Graz University of Technology

Dipl.-Ing (FH) Christoph WOLTSCHE

Numerical study on the joining and testing of self-piercing riveting joints

MASTER THESIS

to achieve the university degree of

Diplom-Ingenieur (Dipl.-Ing.)

Master's degree programme
Advanced Materials Science

submitted to the

Graz University of Technology

Supervisor:
Univ.-Prof. Dipl.-Ing. Dr.techn. Christof Sommitsch

Co-Supervisor:
Ass.Prof. DDDipl.-Ing. Dr.mont. Josef Domitner
Dipl.-Ing. Florian Hönsch, BSc

Institute of Materials Science, Joining and Forming
Research Group Tools & Forming

St. Marein bei Graz, May 2019

EIDESSTATTLICHE ERKLÄRUNG

AFFIDAVIT

Ich erkläre an Eides statt, dass ich die vorliegende Arbeit selbstständig verfasst, andere als die angegebenen Quellen/Hilfsmittel nicht benutzt, und die den benutzten Quellen wörtlich und inhaltlich entnommenen Stellen als solche kenntlich gemacht habe. Das in TUGRAZonline hochgeladene Textdokument ist mit der vorliegenden Masterarbeit identisch.

I declare that I have authored this thesis independently, that I have not used other than the declared sources/resources, and that I have explicitly indicated all material which has been quoted either literally or by content from the sources used. The text document uploaded to TUGRAZonline is identical to the present master‘s thesis.

_____ _____

Datum / Date Unterschrift / Signature

ABSTRACT

In modern vehicles, weight plays a major role. Emissions and fuel consumption of an automotive vehicle are strongly dependent of its weight. To reduce the weight, different materials are employed, such as aluminium (and its alloys) because of its good mechanical properties and low density. The use of multiple materials requires different joining methods such as welding. However, utilising thermal joining process on aluminium and its alloys can be challenging because of the formation of an oxide layer. Therefore, mechanical joining processes like riveting, clinching, or adhesive bonding are used instead.

The aim of this thesis is to develop a numerical three-dimensional (3D) model of the self-piercing rivet process to analyse different situations which can occur during the joining process. This includes the influence of a misalignment of the rivet and tilting of the die. Experimental data is used to validate the numerical simulations.

First, a two-dimensional (2D) model of the setting process was developed, and the simulation result was rotated by 180 degrees about the centre axis. The stress field and the strain field were mapped onto the 3D simulation model. With the numerical 3D model, an axial tension and a shear tension simulation were performed. With the help of those simulations, the mechanical strength of the joints was analysed. To investigate the setting process, a 3D hybrid FEM-SPG model was created, and the different simulations, e.g., rivet offset and die tilting, were performed.

By using a 3D numerical model, the influence of various input parameters on the quality of a self-piercing rivet (SPR) joint can be evaluated. The main advantage of implementing numerical setting models is that different parameters can be investigated and analysed without the need for numerous samples, therefore saving costs and time. The validation of the 3D simulation results only showed slight differences compared to the experiment.

Kurzfassung

In modernen Fahrzeugen spielt das Gewicht eine wichtige Rolle und steht in enger Verbindung mit Emissionen und Kraftstoffverbrauch. Um das Gewicht zu reduzieren, werden verschiedene Materialien wie Aluminium bzw. Aluminiumlegierungen aufgrund ihrer guten mechanischen Eigenschaften und geringen Dichte verwendet. Die Verwendung von unterschiedlichen Materialien im Automobilbau erfordert wiederum unterschiedliche Fügeverfahren. Ein sehr häufig eingesetztes Fügeverfahren im Automobilbau ist das Schweißen. Die Verwendung eines thermischen Fügeverfahrens für Aluminium bzw. Aluminiumlegierungen kann jedoch aufgrund der Bildung einer Oxidschicht eine Herausforderung darstellen. Daher werden stattdessen mechanische Fügeverfahren wie Nieten, Clinchen oder Kleben eingesetzt.

Ziel dieser Masterarbeit ist es, ein numerisches dreidimensionales (3D) Modell des Stanznietprozesses zu entwickeln. Mithilfe dieses Simulationsmodells sollen verschiedene Situationen, die während eines Fügeprozesses auftreten können, analysiert werden, wie z.B. der Einfluss einer Fehlausrichtung des Niets (Versatz) und eines Kippens der Matrize. Für die Validierung der numerischen Simulationen wurden experimentelle Daten verwendet.

Es wurde zunächst ein zweidimensionales (2D) Modell des Setzprozesses entwickelt und validiert. Anschließend wurde dieses Simulationsergebnis für die Erzeugung eines dreidimensionalen Modells dieser Nietverbindung um 180 Grad um die Mittelachse gedreht. Danach erfolgte die Abbildung der Spannungen (von Mises) und der plastischen Dehnungen aus dem 2D-Setzprozess auf dem neu erstellten 3D-Simulationsmodell. Mit dem numerischen 3D-Modell wurden weiterfolgend Simulationen einer Kopfzug- und einer Scherzugprüfung durchgeführt. Mit Hilfe dieser Simulationen konnte die mechanische Festigkeit der Nietverbindung analysiert werden. Um den Setzprozess genauer zu untersuchen, wurde ein 3D-Hybrid-FEM-SPG Modell entwickelt und verschiedene Simulationen, wie z.B. Nietversatz und Kippen der Matrize analysiert.

Durch den Einsatz eines numerischen 3D-Modells konnte der Einfluss der verschiedenen Situationen des Setzprozesses untersucht und der Einfluss auf die Qualität der Nietverbindung bewertet werden. Der Hauptvorteil bei der Verwendung von numerischen Simulationsmodellen besteht darin, dass verschiedene Parameter untersucht und analysiert werden können, ohne dass zahlreiche Proben für Versuche erforderlich sind, wodurch Kosten und Zeit für diese Versuche gespart werden können. Die Validierung der 3D-Simulationsergebnisse ergab nur geringe Unterschiede zu den Versuchen.

Preface

The work presented was written within the framework of the master's program Advanced Materials Science at Graz University of Technology to achieve the university degree of Dipl.-Ing. It was performed in the research group Tools and Forming, which is part of the Institute of Materials Science, Joining and Forming (IMAT).

I would like to thank my supervisors, Univ.-Prof. Dipl.-Ing. Dr. techn. Christof Sommitsch, Ass. Prof. DDDipl.-Ing. Dr. mont. Josef Domitner and Dipl.-Ing. Florian Hönsch, BSc for their advice, help, and guidance during my work on this master's thesis.

I would also like to thank my family and especially my wife, Carmen, who was very helpful and supportive whilst I was writing and working on this paper.

St. Marein bei Graz, May 2019

Christoph Woltsche

Table of Contents

1 INTRODUCTION

1.1 Motivation and technical task

One of the important things for humankind is to be mobile. For that reason, the automotive industry is amongst the biggest industries on earth. Thus, to reduce fuel consumption and vehicle emissions, modern cars must be light. Since cars gain weight because of the vehicle's infotainment system, new power systems (e.g., batteries for electric and hybrid vehicles), comfort systems (e.g. air conditioning), and other electrical devices (e.g., sensors),automotive engineers must lower the weight in other regions, such as the body structure of the vehicle. Events such as the oil crisis of the 1970s and the increase of greenhouse gases in the earth's atmosphere have been catalytic factors in the need for lightweight materials. The body in white (BiW) represents about 30 per cent of the total vehicle weight, and therefore it is an important area in which weight can be reduced, as shown in Figure 1 [1].

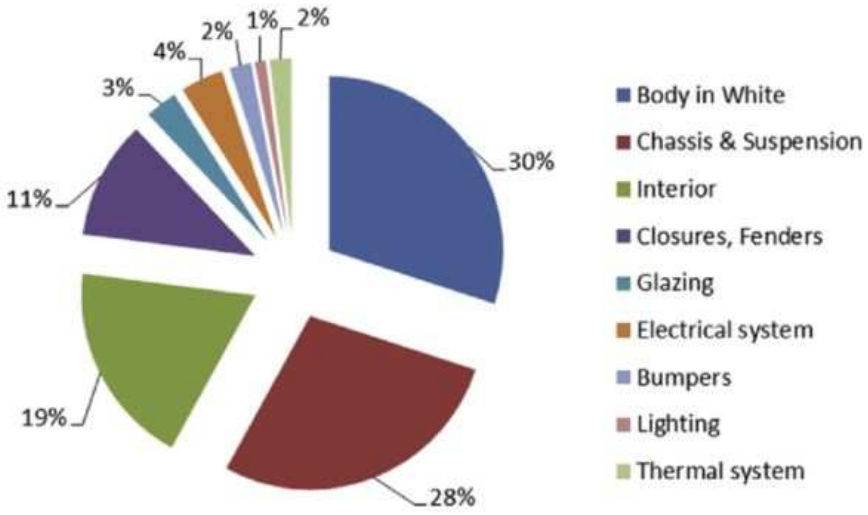

Figure 1 Weight ratio of various vehicle components [4]

The automotive industry uses lightweight materials such as aluminium, magnesium, polymers and composites like carbon-fibre-reinforced plastics (CFRP) in the vehicles. In addition, new steel grades like high-strength steel (HSS) and advanced high-strength steel (AHSS) [1] have been developed and are being used as lightweight materials. In Figure 2, different materials in respect to yield strength and elongation are illustrated.

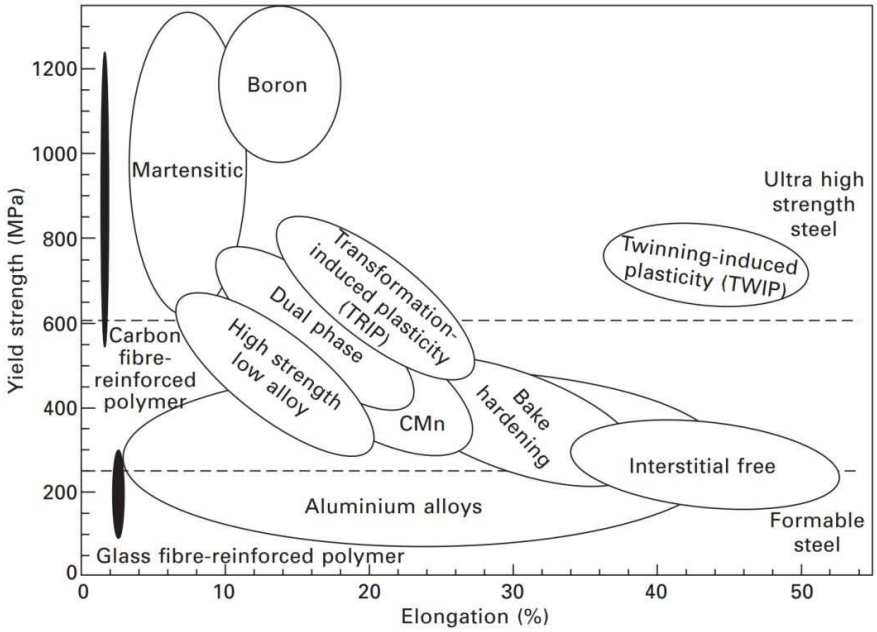

Figure 2 Classification of materials in respect to yield strength and elongation [2]

In modern vehicles, the BiW uses a multi-material, lightweight construction concept whereby different materials are connected using various joining technologies. In Figure 3, the multi-material construction of an Audi A8 is illustrated.

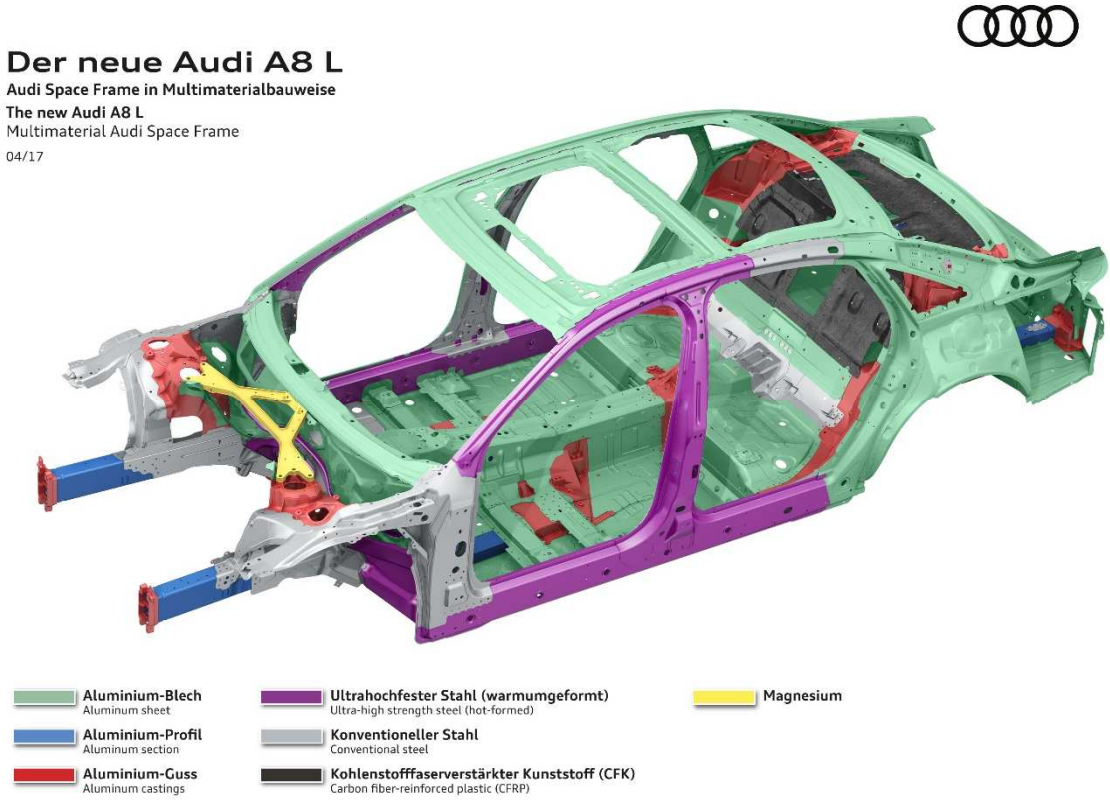

Figure 3 Audi Space Frame in multi-material construction [3]

Because of the different properties of dissimilar joints, traditional joining processes like resistance spot-welding cannot be used for the new structures. Thus, to connect these different materials, new joining methods such as adhesive bonding, mechanical fastening, laser welding, and ultrasonic welding are applied. Some of these are shown in Figure 4.

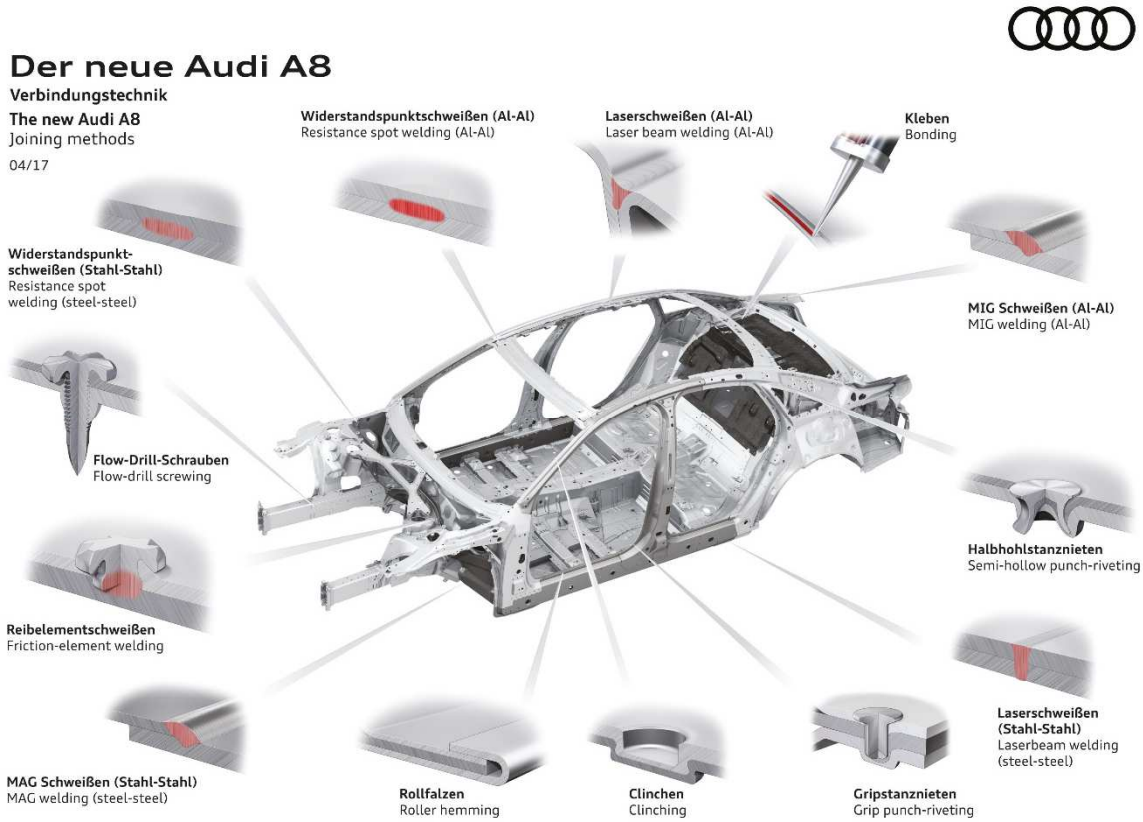

Figure 4 Joining methods, Audi A8 [5]

The automotive industry uses joining methods, which combine adhesive bonding and mechanical fastening (hybrid joining). Self-piercing riveting is one commonly used process for aluminium-aluminium or aluminium-steel connections in vehicles. Structural components are primarily connected using this joining method [6]. The adhesive is the primary joining element, and the rivet fixes the structure in place during curing and additionally acts as a support to prevent catastrophic failure [1].

To determine the mechanical behaviour of the joint, samples are made. Therefore, an SPR is pushed into the two blanks where the force and the displacement are measured. After the processing of the rivet, the produced sample is destroyed with a testing device (tensile and shear testing). The force and the displacement necessary to destroy the connection are measured and

recorded. Furthermore, the area of the failure is investigated. However, it is very time consuming to produce and test the samples.

In the development of modern vehicles, personal computers play a major role. One of the key terms today is computer-aided engineering (CAE). It combines software for engineering and software for calculation like finite element analysis (FEA). With FEA, the mechanical behaviour of joints can be simulated and analysed.

The main focus of this master's thesis is the simulation of an SPR process in 2D and 3D and comparing the numerical results to the experiment. Moreover, a destructive simulation model of an SPR joint was created and analysed. For the analysis, the FEM-solver LsDyna was used.

1.2 Thesis structure

The first part of this thesis describes the technical task and the reason why the self-piercing rivet connection is so important in the automotive industry.

Chapter 2 discusses different joining technologies in terms of their working mechanism and manufacturing process, as well as advantages and disadvantages of the connection. At the beginning, a classification of joining processes is implemented, and the different joining technologies are explained in detail.

Chapter 3 contains geometrical information about the SPR and the equipment for producing an SPR connection. Furthermore, the process monitoring for SPR is described. In addition, the quality criteria of an SPR connection are explained using microsections. The end of this chapter describes the destructive tests of an SPR connection.

Chapter 4 introduces the numerical simulation. For this purpose, the finite element method (FEM) and especially the solver LsDyna are described in detail. Furthermore, the process steps of the FEM are explained, from the meshing of a geometry in a pre-processor to the visualisation of the result in the post-processor program.

In chapter 5, a 2D simulation model of the SPR setting process is developed, and the results are compared to the experiment. After the 2D setting process, a 3D model is created by rotating the result of the 2D simulation about the centre axis. The stress field and strain field of the 2D model are mapped onto the 3D model. An axial tension and shear tension simulation is performed with

the developed FEM models. The destructive simulation results are then compared to the experimental destructive tests.

During joining, misalignments like eccentricity of the rivet and tilting of the die can occur. With the help of the 3D simulation model developed in chapter 6, those problems can be investigated.

Finally, chapter 7 summarises the thesis and provides an outlook of possible modifications for the 3D simulation.

2 JOINING TECHNOLOGIES

This chapter contains an overview of the joining processes important for the BiW as well as a description and classification of the main joining methods.

2.1 Classification of joining processes

Metal joining is defined as the joining of two or more metal parts either temporarily or permanently with or without the application of heat and/or pressure. Figure 5 shows the six main groups of the manufacturing process, including joining in the fourth group. The joining group is divided into nine subgroups. For joining of modern vehicles, the subgroups 4.5) joining by forming, 4.6) welding, 4.7) soldering, and 4.8) adhesive bonding are the most important ones.

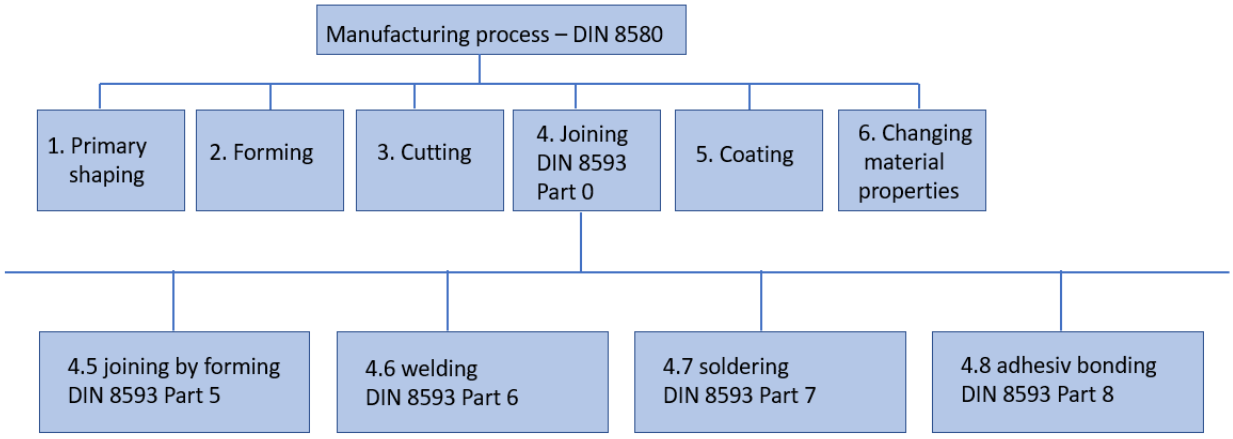

Figure 5 Manufacturing process (overview) [7]

The overview in Figure 6 illustrates the different joining processes as a function of temperature. It starts on the left side with room temperature and the joining methods fastening and adhesive bonding and ends on the right side with welding, which applies higher temperature (melting temperature). In between, there is soldering and brazing, with temperatures around 450°C. In the automotive industry, mainly spot-welding, mechanical fastening, and adhesive bonding are used.

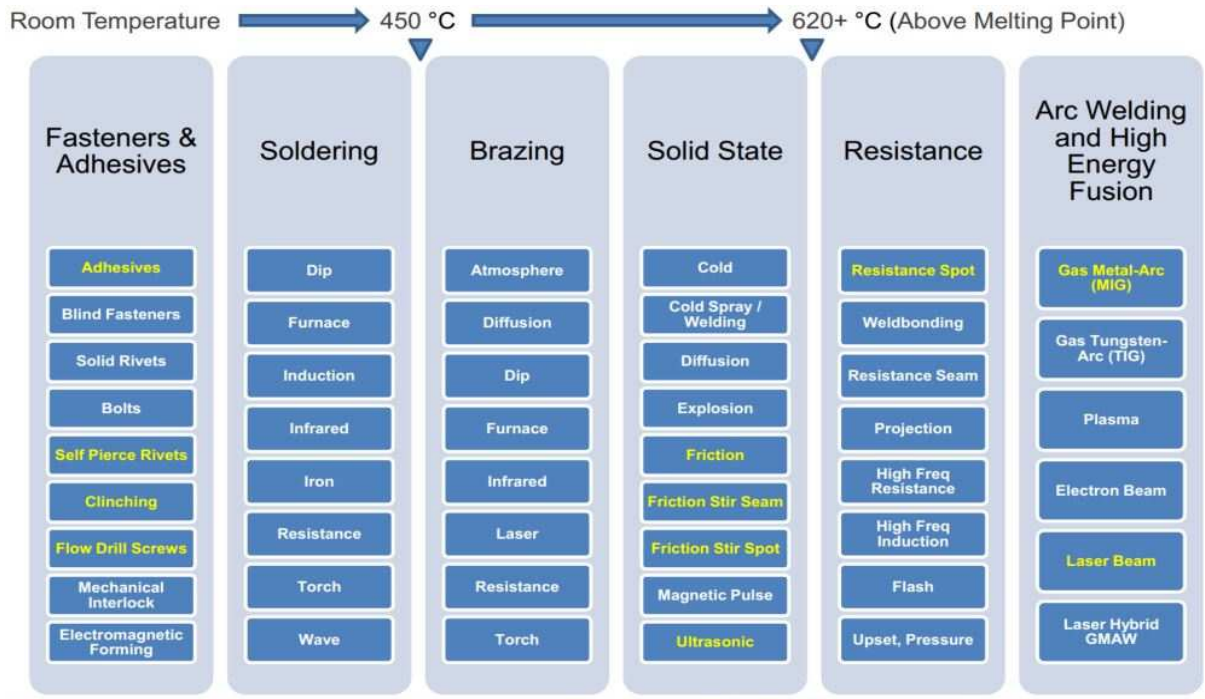

Figure 6 Overview of different joining technologies [32]

2.2 Welding

Welding is one of the key joining technologies used in several fields. Figure 7 shows the market share of different industries using welding technology. The bar chart illustrates that mechanical engineering along with the subgroup automotive industry comprises about 50 per cent market share of welding technology [7].

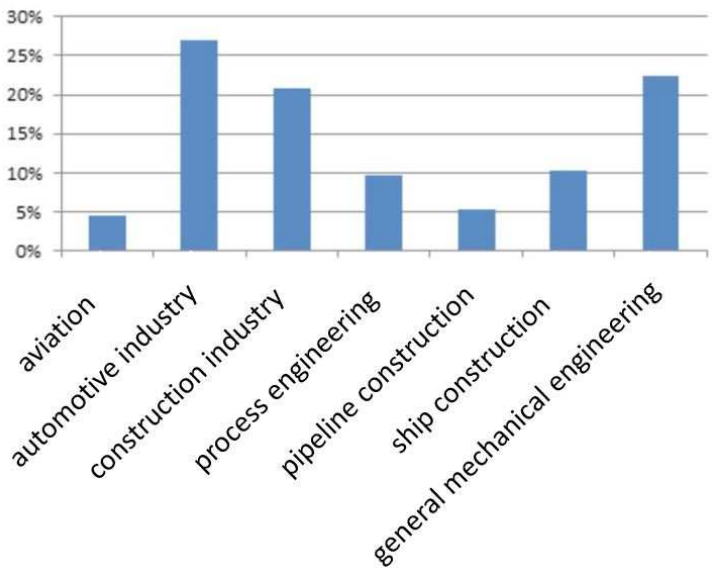

Figure 7 Market share of different industries in welding technology [7]

Definition of welding

A weld is a metallurgically bonded connection between two or more similar or dissimilar materials with usage of heat and/or force with or without filler material. Similar material means nearly the same melting point and chemical composition. The connection is irresolvable and would be destroyed during dismantling [8]. Because of the metallurgical bond, welding constructions are particularly suitable for transferring forces or moment, higher operational temperature, and sealed joining areas.

The advantages of welding compared to mechanical fastening or riveting are no weakening of the base materials (e.g., holes) and less weight because there are no extra parts like screws or rivets. The disadvantages of welding are shrinkage, high inner stress, and the heat-affected zone (HAZ), which can lead to brittle fracture of the weld [10].

Classification of welding methods

The general classification of welding is shown in Figure 8, where welding is separated between fusion and pressure welding [7].

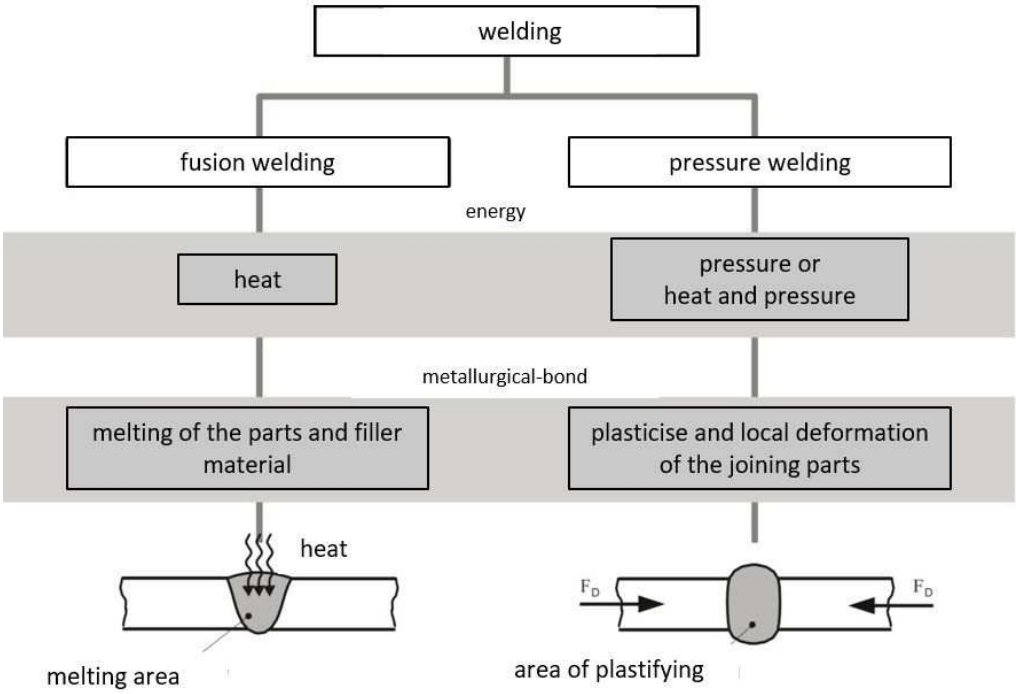

Figure 8 Classification of welding [7]

Fusion welding means local melting of the joining parts without force and with or without filler material. Different fusion welding methods are gas welding, arc welding and laser beam welding [9].

Pressure welding means welding with force (pressure) and with or without filler material. Different pressure welding methods are resistance welding, friction welding, cold pressure welding, and ultrasonic welding [9].

Weldability

The weldability of a construction depends on the material, construction, and production of the weld. The weldability in respect to the material depends on the chemical composition, the metallurgical properties, and the physical properties. For steel, weldability depends mainly on the carbon and the amount of alloying elements. The important aspect for construction or the safety of the construction is that the design with the used material can withstand the mechanical load. The production of the weld is divided into three parts: preparation, which means choosing the welding process or preheating the welding components; performance, e.g., the sequence of the welding seams to reduce distortions; and follow-up treatment, e.g., heat treatment of the weld [10]. The influencing parameters are shown in Figure 9.

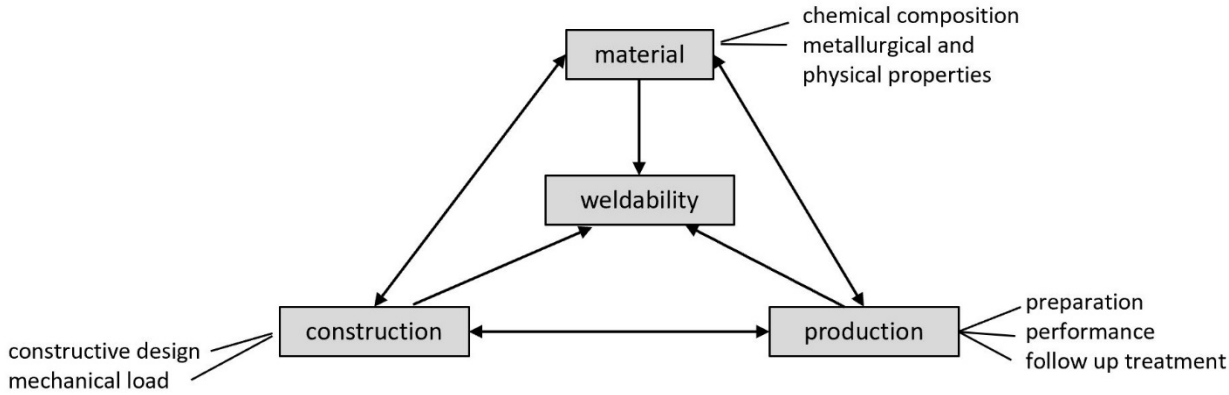

Figure 9 Influencing factors for weldability of a component [10]

Advantages of welding [11]:

- high mechanical strength
- low weight compared with other joining methods
- high temperature stability

Disadvantages of welding [11]:

- thermal distortion near the seam
- change of the microstructure in the welding area (HAZ)
- hard-to-detect defects in the welding seam (only with x-ray or ultrasonic)

2.3 Brazing and soldering

Brazing and soldering are thermal processes for the joining and coating of materials whereby a solder between the components is melted. The temperature of soldering is much lower than that of welding. The connection of the solder and the base material happens by diffusion at the interface (diffusion soldering, as shown in Figure 10). Joining by soldering means a temperature lower than 450°C, and joining by brazing means a temperature higher than 450°C. Soldering is mainly used in electronics to connect wires to an electrical device. Brazing is used to join components which can resist a higher load, e.g., vehicle frame [10].

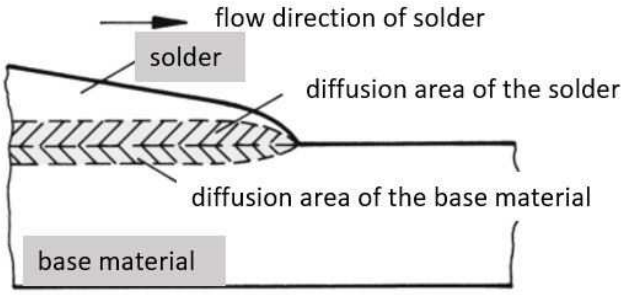

Figure 10 Diffusion of solder and base material [10]

Advantages of soldering and brazing [10]:

- joining of different sorts of metals is possible
- high electrical conductivity at the joining area
- no weakening of the base material due to holes, which are needed for riveting or screwing
- good automation capacity

Disadvantages of soldering and brazing [10]:

- solder consists of expensive elements like silver or tin
- problems with aluminium (electrolytic destruction of the connection)
- soldering flux can lead to corrosion
- low mechanical strength of the connection

2.4 Adhesive bonding

In several years, adhesive bonding has gained importance in the automotive industry. The most relevant reason is the ability to join similar and dissimilar materials. The joining mechanisms of adhesive bonding are described by three theories [12]:

- electrostatic theory (Figure 11 a)
  An electrostatic force occurs between the interfaces of the adherend and the adhesive (e.g., van der Waal force [dipole interactions], hydrogen bond)
- diffusion theory (Figure 11 b)
  Through this mechanism, atoms can be exchanged between the adherend and the adhesive at the interface. This could occur in the solid or liquid form of the adhesive, mostly by similar composition of the adhesive and the adherend.
- mechanical interlocking contribution (Figure 11 c)
  The adhesive must penetrate the surface of the adherent. That means every material has a certain surface roughness (e.g., peaks and valleys) which depends on the production process of the component. There is no chemical bonding between the adherent and adhesive. To get a stronger connection, the surface must be roughened [12].

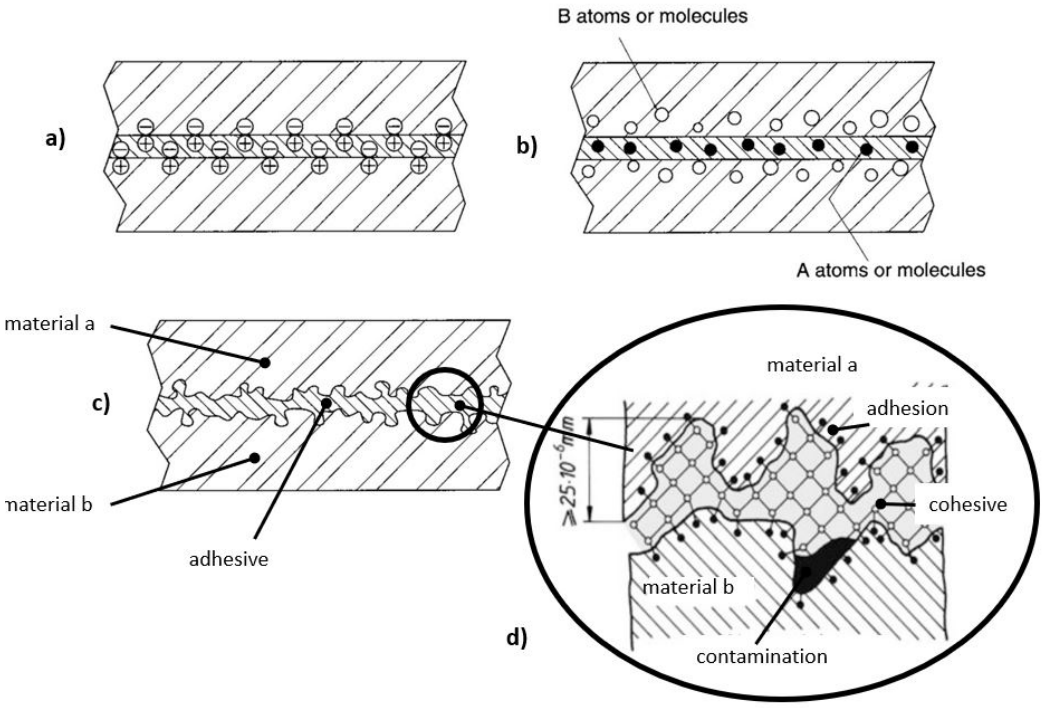

Figure 11 a) electrostatic theory [12], b) diffusion theory [12], c) mechanical theory [12], d) closer look at the connection [10]

Failure of adhesive bonding:

There are two failure mechanisms: adhesive failure and cohesive failure. Adhesive failure is the failure between the adhesive and the adherends. Cohesive failure is the physical failure in the adhesive. The main reason for adhesive failure is often improper preparation of the surface [12].

Additionally, the implementation of adhesive bonding into the construction has a major influence on the connection. The load should be transferred by compression, shear, or tension. Problems can occur if the mechanical load is transferred by peeling and cleavage [12].

Advantages of adhesive bonding [12]:

- does not change the microstructure
- has nearly no effects on the properties of the material
- joining of similar or dissimilar materials
- prevents galvanic corrosion
- connection of any shape is possible
- better stress distribution and reduction of stress concentrations
- easy sealing (liquids, gas)
- damping capacity

Disadvantages of adhesive bonding [12]:

- preparation of the surface is necessary
- long curing times
- no visual examination of the bonding area after joining
- repairing defected bonding areas is impossible
- limited working temperature
- health hazards because of the solvent used for cleaning

2.5 Joining by forming

Joining by forming is based on plastic deformation of the components and results in a form closure between the parts. Hydraulic or mechanical force is used for the plastic deformation of the parts. The classification of this joining technology is shown in Figure 12 [13].

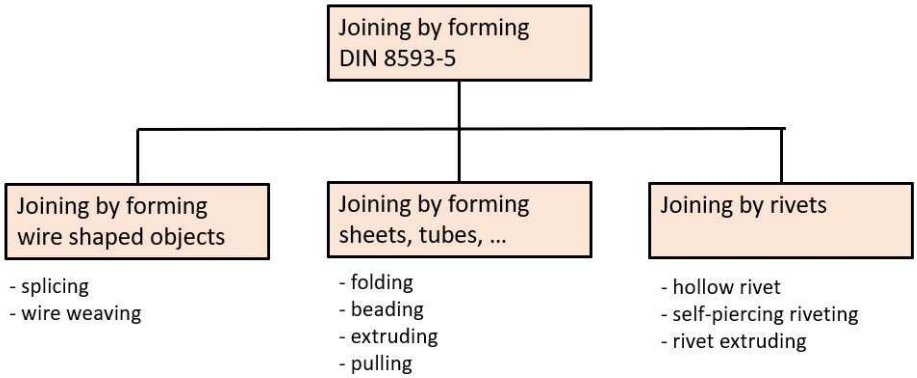

Figure 12 Overview of joining by forming [13]

Advantages of joining by forming [8]:

- similar or dissimilar materials can be joined
- no HAZ
- low process time
- less preparation time

Disadvantages of joining by forming [8]:

- overlapping of joining partners
- causing bumps in the joining area
- low mechanical strength

Mechanical joining

Mechanical joining processes are, for example, riveting, screwing and clinching. The connection is based on a force fit and/or a form fit. In Figure 13, some mechanical joining technologies of an Audi TT are shown.

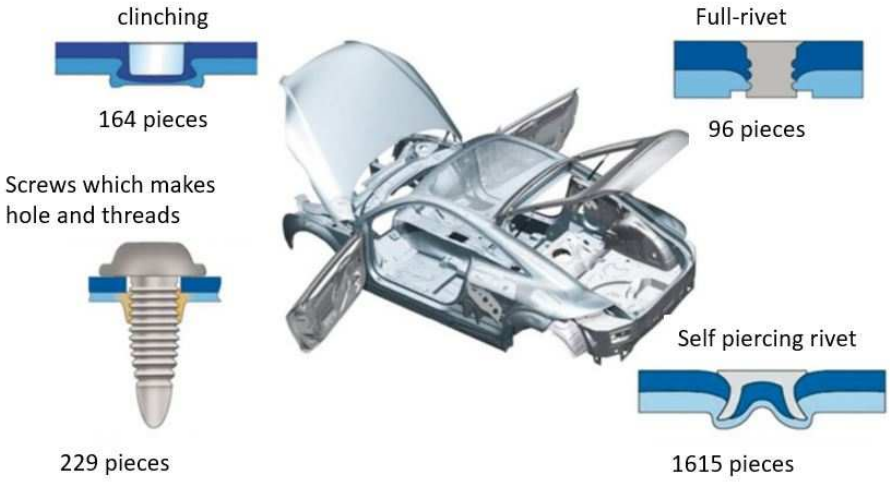

Figure 13 Mechanical joining elements in the Audi TT [7]

Those methods produce spot-like connections, and therefore they have no sealing properties. The joining elements are mostly made of steel. Joining of aluminium parts can lead to corrosion; thus, some measures must be accounted for like coating of the rivet [14].

2.5.1 Clinching

Clinching is a mechanical joining method where at least two sheets are combined only by cold forming (locally severe plastic deformation). A punch is used to form an undercut between the sheets without using any additional joining elements. The cross section of such a connection is shown in Figure 14a [13].

The joint quality of a clinch depends on the neck thickness (tn), undercut (ts), and the joint's bottom thickness (X). Those parameters are responsible for the mechanical strength of the connection [17]. This is also illustrated in Figure 14b on the right side.

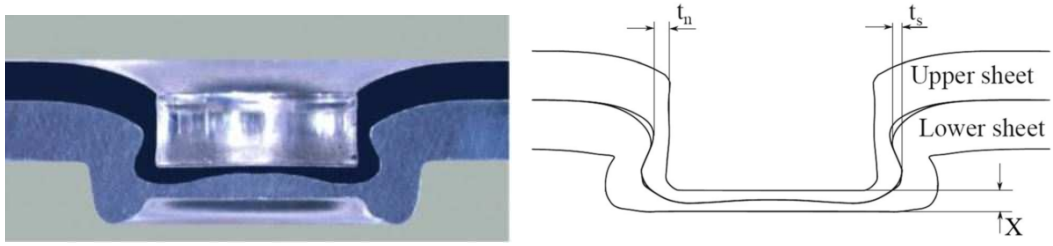

(a) (b)

Figure 14 (a) Cross section of a clinching point [13], (b) interlocking condition [17]

In the automotive industry, there are numerous clinching process like

- clinching with or without cut section
- single-stage or multistage process

2.5.1.1 Clinching (standard)

The production steps of a single-stage clinching process without cut section are plotted in Figure 15. In the first step, the blanks are fixed with the help of the blank holder. In the second step, the punch starts to move down and deforms the metal sheets. In the third step, the punch pushes further down, and the lower sheet starts to yield into the small hollow cavities in the lower area of the die. Between the upper and lower blanks, an undercut is formed. The size of the undercut and the wall thickness are important for the strength of the connection. In the last step, the tool opens, and the connected sheets can be extracted [13].

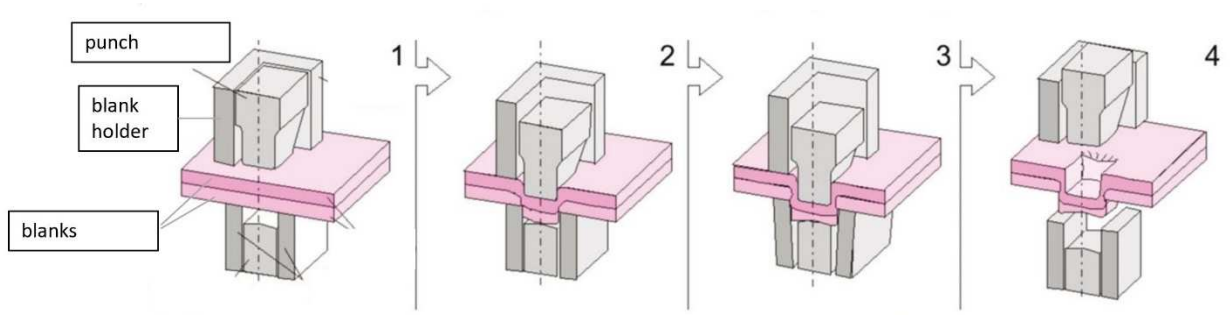

Figure 15 Clinching process without cut section [7]

2.5.1.2 Shear clinching

The single-stage clinching process with section cut is plotted in Figure 16. The main difference is the geometrical form of the connection. In Figure 16c, the rectangular shape of the clinching point, which has a partial cutting area, is shown [13]. Figure 16c also shows the sheets which are joined by interlock between the upper and lower sheets with upper sheet separation in the short sides of a rectangle, whereas fractures are prevented in the long sides of a rectangle [17].

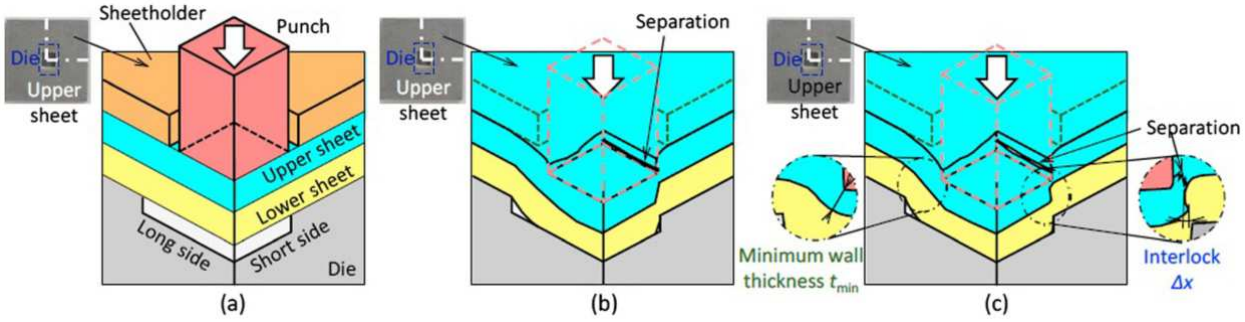

Figure 16 Clinching process with cut section (shear clinching) [17]

2.5.1.3 Hole-clinching process

To join high-strength steel, clinching as a joining approach is problematic. Therefore, the hole-clinching process was developed. For this joining method, a predrilled sheet is used. The predrilled lower sheet is the one with the higher strength. The upper sheet is then punched down and starts to yield in the lower cavity. The lower cavity helps to generate the interlock. This method is used to join aluminium to high-strength steels and carbon-fibre-reinforced plastic (CFRP) [17].

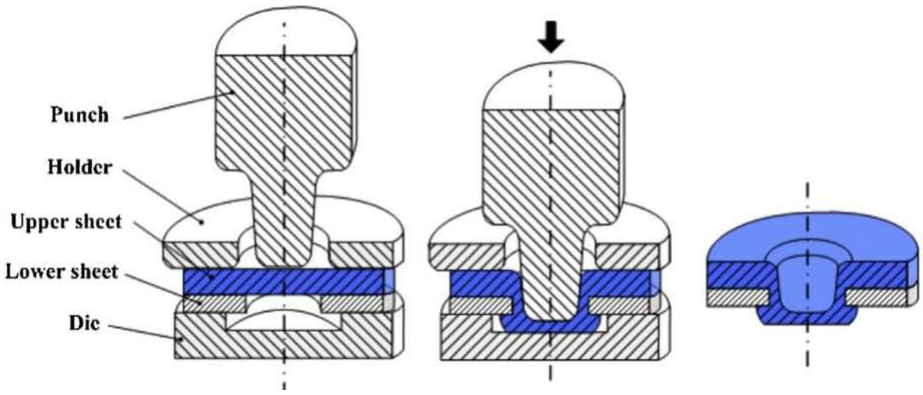

Figure 17 Hole-clinching process [17]

2.5.1.4 Die-less clinching

In this variant, the two sheets are lying on a flat die. The clamp and the punch are moved down to the sheets. The clamp comes in contact with the upper sheet, and low pressure is applied. The punch starts to push down with a higher force, and the sheets under the punch begin to deform. Because of this deformation, the sheets are moved in the upper direction and push the clamp upwards. The material under the punch flows in radial direction, and the interlock is formed [17]. This process is illustrated in Figure 18.

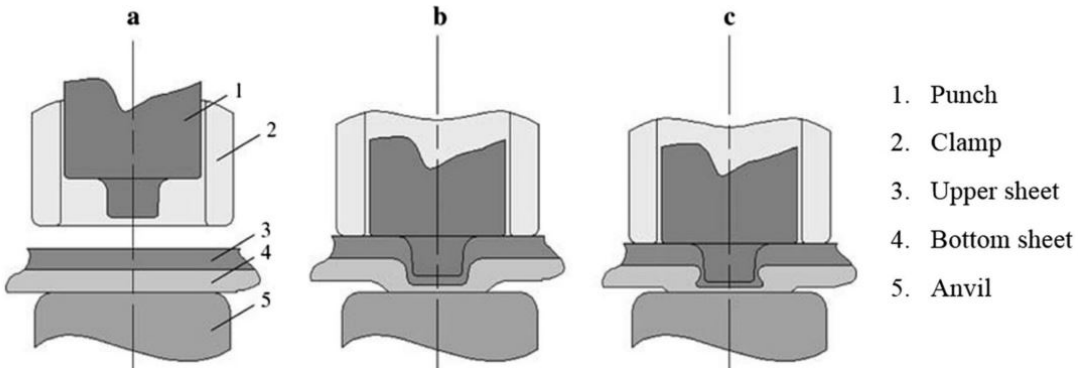

Figure 18 Die-less clinching [17]

Failure in clinching [16]

- failure due to the lack of interlock between the two sheets
- fracture of the upper sheet in the necking area (ductile problems)
- too high tensile stress in bottom of the joint

2.5.2 Riveting

Rivets are widely used in mechanical engineering. In the next few sections, different kinds of rivets, such as solid rivet and SPR, are explained.

2.5.2.1 Solid rivet

In Figure 19, the riveting process is shown. For preparation, a hole must be drilled into the sheets where the rivet is inserted. The counter holder encloses the rivet head on one side, and on the other side, the upper die presses against the closing head. As a result, plastic deformation of the rivet occurs, which leads to a force, and forms closure. This process takes place at room temperature, although for bigger rivets, the temperature could be higher [7].

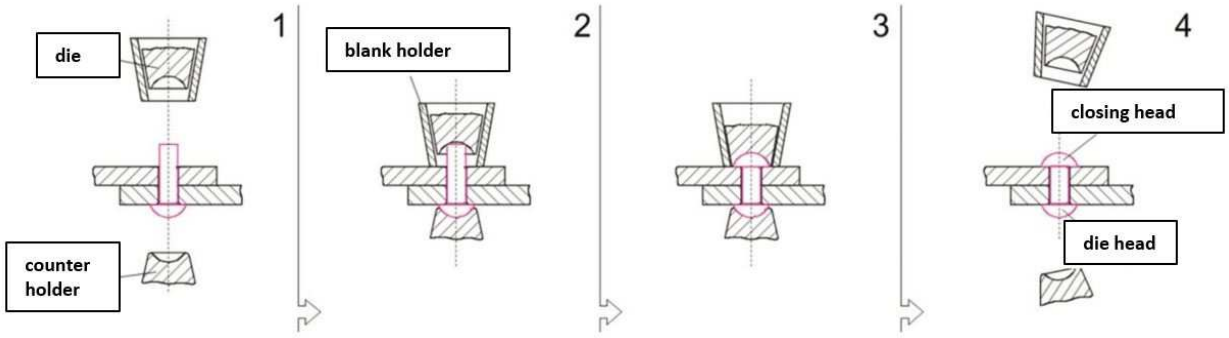

Figure 19 Solid rivet process [7]

2.5.2.2 Self-piercing riveting

Self-piercing riveting is another joining method which creates a form fit by cold deformation of the sheets and rivet. The difference with clinching is that an extra element, the rivet, is used. For this joining method, a preparation of the joining components (e.g., predrilled hole) is not needed. The rivet pierces through the sheet and creates a horizontal interlock [17].

Process steps of self-piercing riveting

The joining process of an SPR can be described in four steps, as shown in Figure 20. In the first step, the blank holder comes in contact with the metal sheets and applies a force between 5 and 10kN (clamping step). In the second step, the rivet is pushed down by a punch and pierces the upper metal sheet (piercing step). In the third step, the horizontal interlock is formed by spreading the rivet shank and by the flowing of the lower sheet material into the cavity of the die (spreading step). After reaching the predefined force or stroke, the punch stops and goes back to its initial point [17].

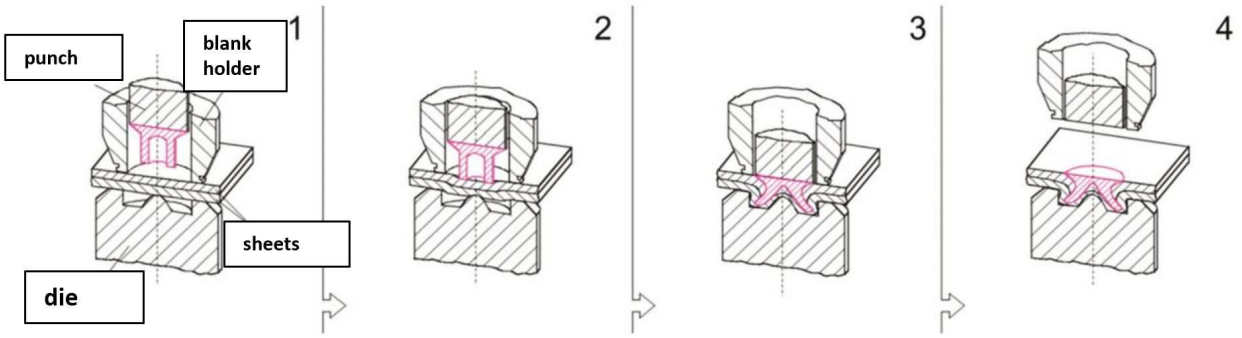

Figure 20 SPR process [7]

Quality criteria of an SPR

The final position of the rivet head is one quality criterion of the connection. It should be in plane with the upper metal sheet or a little bit lower. Another criterion is the residual wall thickness which is the minimal thickness of the lower metal sheet. It depends on the material of the sheet, the pressure during the processing, and the form of the rivet. The most important factor is the horizontal interlock which defines the mechanical strength of the connection. This interlock is the horizontal length between the outermost point of the rivet and the innermost point of the lower metal sheet [6]. Figure 21 shows a section cut of the rivet

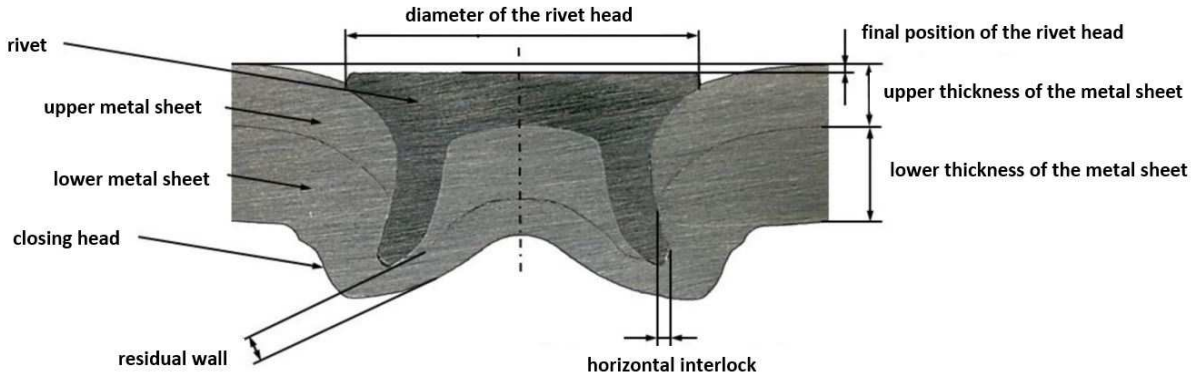

Figure 21 Cross section of an SPR with terms of the relevant areas [6]

Advantages of SPR [19]:

- similar and dissimilar materials can be joined (see Figure 22)
- no predrilled hole (less preparation) necessary
- can be easily automated
- connection has a high mechanical strength and good fatigue properties
- no waste materials
- localised plastic deformation

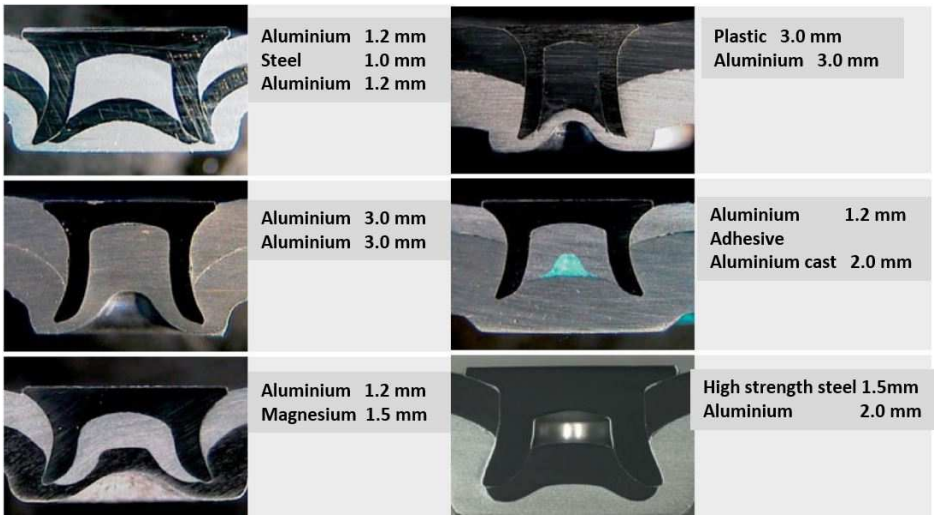

Figure 22 Different materials connected with spr [20]

Disadvantage of SPR [19]:

- the process needs access from both sides
- high process force
- bulges on one side of the connection
- problem with brittle materials

Solid punch rivet

Solid punch riveting is a method which has a high connection strength, and the joining has a two-sided conciseness. Two or more metal sheets with the same or different thickness or strength can be connected. Another advantage is that there is no need for preparation of the connection area like drilling a hole [15].

In Figure 23, the joining process of a solid punch rivet is illustrated. The process is divided into four steps. In the first step, the blank holder goes down, pushes the blanks against the die with a defined force, and holds the metal blanks in place. In the second step, the punch pushes through the metal sheets. The pieces which were punched out are disposed. In the third step, the punch pushes the rivet or the head of the rivet into the upper sheet. The rivet itself has a special kind of groove in which the material of the lower blank is forced to yield, which is shown in the cross section of Figure 24. Because of this plastic deformation, a form-fit joint is realised. The rivet itself is rigid and has no plastic deformation. In the fourth step, the punch and the blank holder move upward [16].

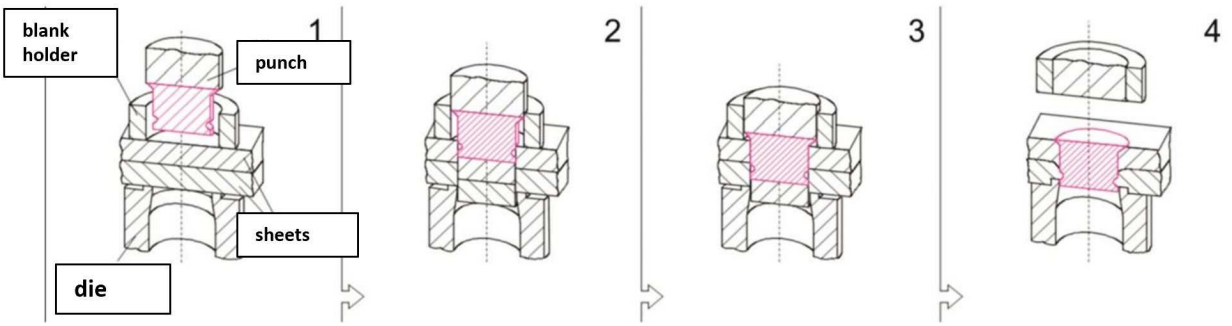

Figure 23 Solid punch rivet process [7]

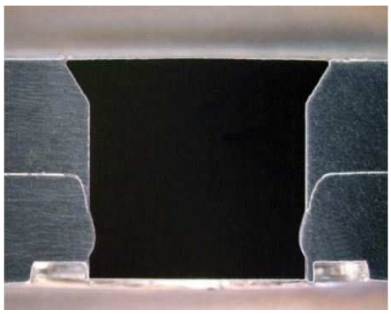

Figure 24 Cross section solid punch rivet [13]

Influence on the joining quality [16]:

- blank holder force
- punching force
- geometry of the die and the rivet

The main scope of application is in the automotive and railway industry. Sheets up to a thickness of 5mm and also materials with a high tensile strength (Rm>1000MPa) can be joined.

Hydro self-pierce riveting

Another form of rivet joining is hydro self-pierce riveting. Instead of a die, a fluid is used as a counterpart. A clamping force for the two sheet metals is produced between the blank holder and the fluid. The SPR is pushed down by a punch. The upper sheet is pierced, and the rivet starts to deform in the lower sheet and creates the interlock. During the whole process, the fluid presses with a pressure between 600 and 2000 bar against the lower metal sheet. The pressure depends on the material and the thickness of the material to which it should be connected [21].

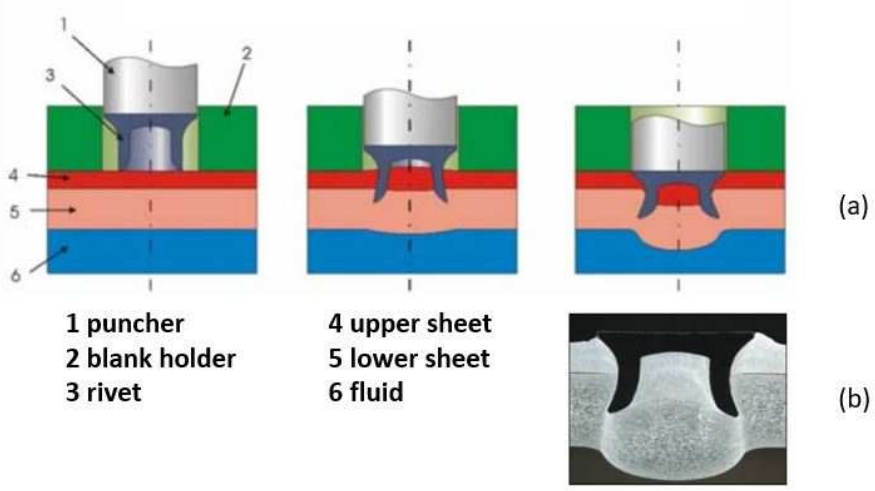

Figure 25 (a) Process and (b) cross section of hydro SPR [21]

2.6 Combined joining technologies

Nowadays, the automotive industry uses combinations of different joining techniques. Thus, the joining methods clinch riveting, resistance spot clinching, and adhesive bonding with SPR are described.

2.6.1 Clinch riveting

Clinch riveting is a combination of riveting and clinching. That means a solid rivet is pressed against two or more sheets. The solid rivet is much smaller than the recess in the die. The rivet deforms the sheets into the cavity of the die, where the sheets deform in radial direction which forms the horizontal interlock between the upper and lower sheets. The strength of this joint is much higher compared with a standard clinching joint because of the presence of the solid rivet [17].

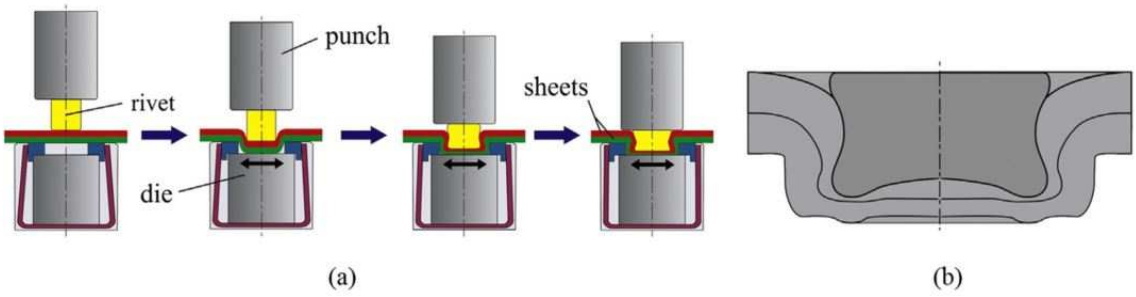

Figure 26 (a) Process of clinch riveting, (b) cross section of the joint [17]

Disadvantages of clinch riveting [17]:

- extra weight because of the rivet
- increasing of process force

Advantages of Clinch Riveting [17]:

- no heat
- no damage to surface coating
- no need for predrilled holes
- higher strength of the connection compared to clinching
- higher destructive energy
- higher stiffness of the joint

2.6.2 Resistance spot clinching

One hybrid joining method is resistance spot clinching. It is like conventional clinching but includes a current phase. The process consists of four steps. In the first step, a processing table is inserted between the sheet and the upper and lower moulds. The upper mold moves down, and a clamping force is applied. In the second step, a low-level current is applied, and the punch pushes the sheets into the cavity of the die. In the third step, a high-level current is applied in the deformed area; the material starts to melt, and the joint is formed. In the last step, the punch moves up to its initial position. The advantage of this joint is increased tensile strength; it is also an energy-efficient joining process (low amount of energy used) compared to spot-weld joining [17].

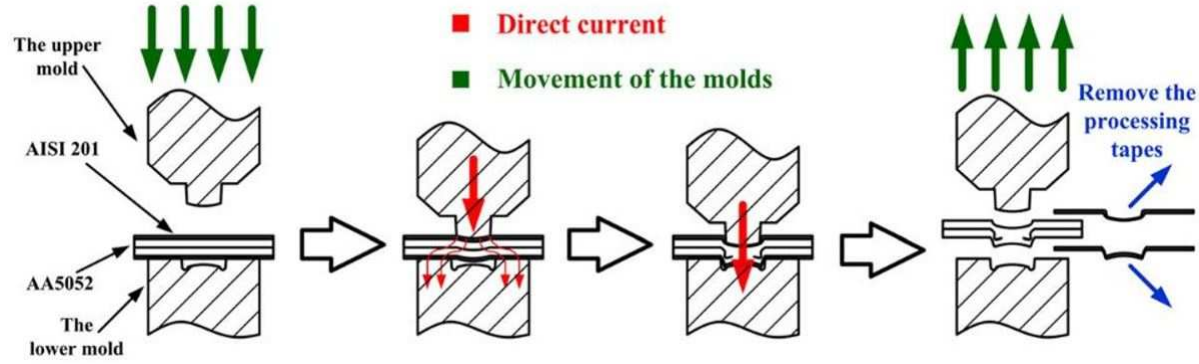

Figure 27 Process steps of resistance spot clinching [18]

2.6.3 Hybrid joining

Another hybrid joining method is adhesive bonding combined with self-piercing riveting. In the first step, the adhesive is applied between the metal sheets. The second step is the riveting process, which means the blank holder comes in contact with the sheets, and a certain pressure is applied. Next, the punch pushes the rivet through the upper sheet into the lower sheet, where the rivet starts to spread and form the horizontal interlock. Because of the rivet, a constant pressure is applied to the sheets and the joint is left to harden. The process is illustrated in Figure 28.

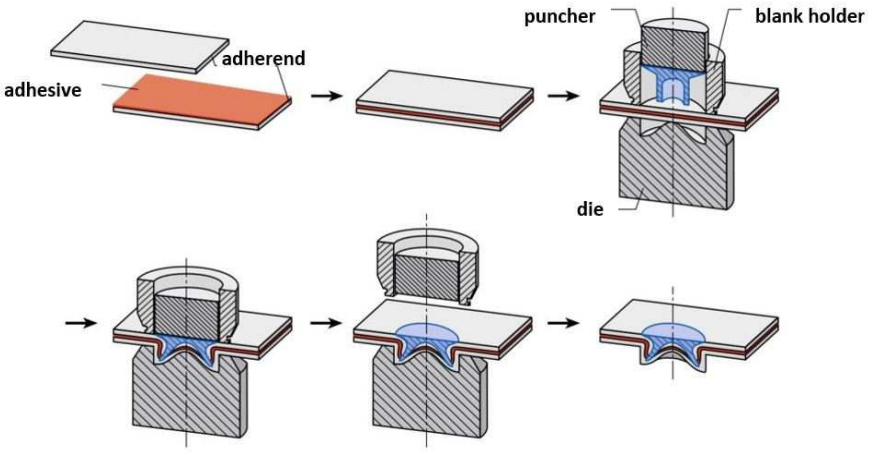

Figure 28 Hybrid connection of SPR and adhesive [22]

Figure 29 shows force-displacement curves from shear tension tests of a standard SPR and hybrid joint. In this diagram, the strength of the joint is illustrated where the hybrid connection has much higher strength because of the adhesive bonding.

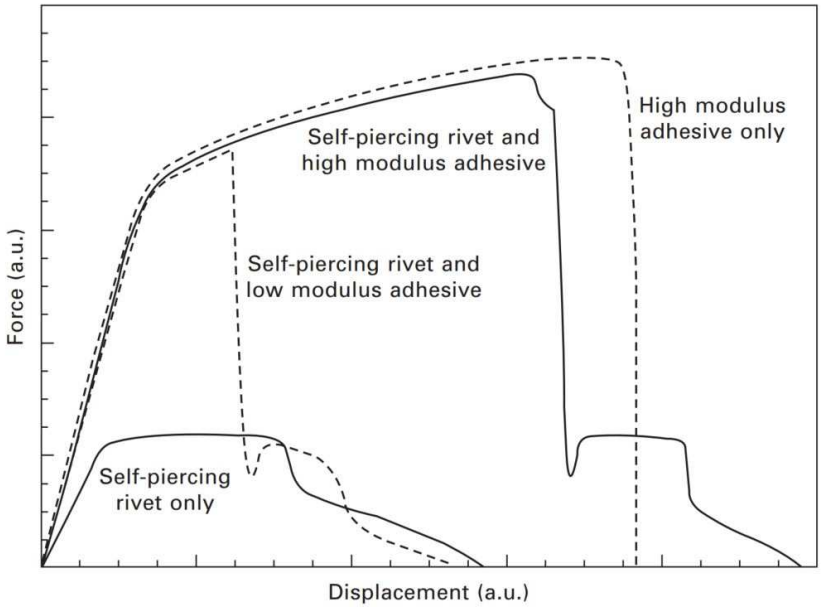

Figure 29 Comparison of SPR and hybrid SPR with adhesive [2]

The failure of hybrid joints does not happen abruptly in all bonded areas. In the area of the SPR, the adhesive failure is delayed, and therefore the connection will not be disrupted instantly, which is a kind of safety feature.

3 SELF-PIERCING RIVETING

This chapter describes the equipment necessary to create an SPR joint as well as the self-riveting process and the mechanical tests.

3.1 Equipment for self-piercing riveting

A self-piercing riveting system consists of different components which depend on the application itself and the level of automation. One main part of the system is the C-frame with the integrated SPR device, including the power unit and rivet magazine.

The rivet can be fed manually by hand. This is used especially for joining of prototypes or automatically via table or magazine. The tape-feed can store up to 11,000 rivets (depending on the size) and can be supplied in spools or cassettes. Magazines store fewer rivets, but they would be faster to refill. For the drive system, an electric or hydraulic unit is used to push the rivet into the metal sheet. A C-frame is used to reach the connection point from both sides. The C-frame must be very stiff, otherwise, the frame could be deformed (bending) during the process, which creates an inaccuracy [1]. The system to create a SPR joint is illustrated in Figure 30.

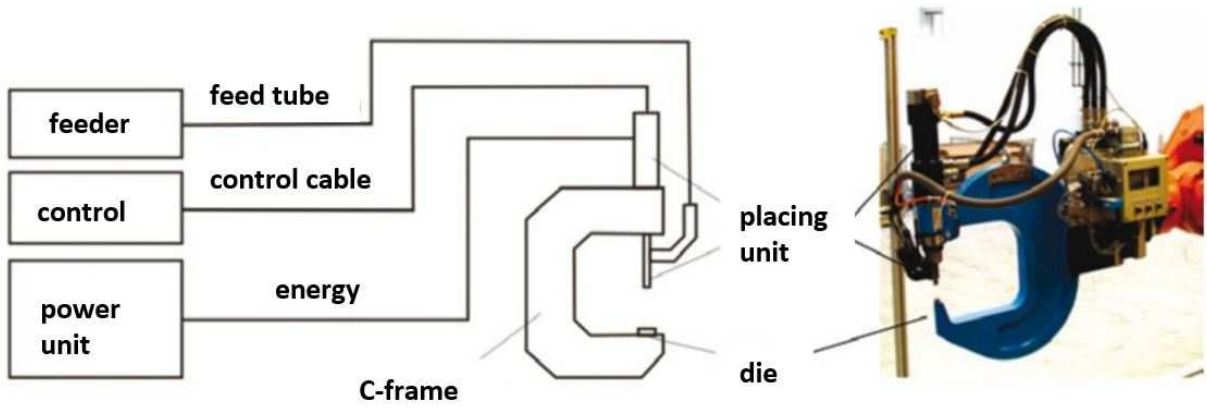

Figure 30 Equipment of an SPR system [7]

The process can be controlled by:

- velocity
- force
- displacement

3.2 SPR process

For novel joints in self-piercing riveting (section 2.5.2.2.), the standard approach is to optimise the rivet-die combination and, after that, to choose the gun. Every process has a window, like a

process tolerance, in which the quality of the joint is sufficient. This is necessary because there is some variation in material thickness (tolerance), composition of the material (strength), surface coating, and so on [1].

Problems which can occur during processing [1]:

- gap between rivet head and upper metal sheet
  (sign of incorrect position of the rivet)
- gap between rivet shaft and sheets
  (reducing fatigue strength; corrosion problems)
- cracks in the material
  (reducing fatigue strength; also leads to corrosion problems)
- symmetry problems of the joint (eccentricity)
  (lower mechanical strength because of the incorrect position of the rivet)
- piercing of the lower sheet
  (leads to corrosion problems)

When some of these problems occur, there is usually an equipment issue, or some parameters are wrong. Normally, it is easy to change the parameters or switch the equipment. If the process is adjusted well, the reproducibility is very high.

3.2.1 Monitoring of the process

Sensors record different process parameters like punch velocity, displacement, force, and also the equipments condition. The displacement and the force of the system are two useful parameters to create a force-displacement curve which is characteristic for the connection. The shape of the force-displacement curve is like a fingerprint of the connection with the same process conditions. A reference curve from a perfect connection can be compared to the curve of the ongoing process, and therefore a quality check can be done [19]. One example of a force-displacement curve with the different process phases is illustrated in Figure 31. In this figure, the cutting phase with a lower amount of force is shown. After piercing through the upper sheet, more material of the lower sheet flows into the die. The rivet starts to deform (spreading). During the first step of the process, the lower sheet also deforms and comes in contact with the die. The force level starts to increase because of the spreading of the rivet. In the last phase, the rivet compresses, and the final horizontal interlock forms.

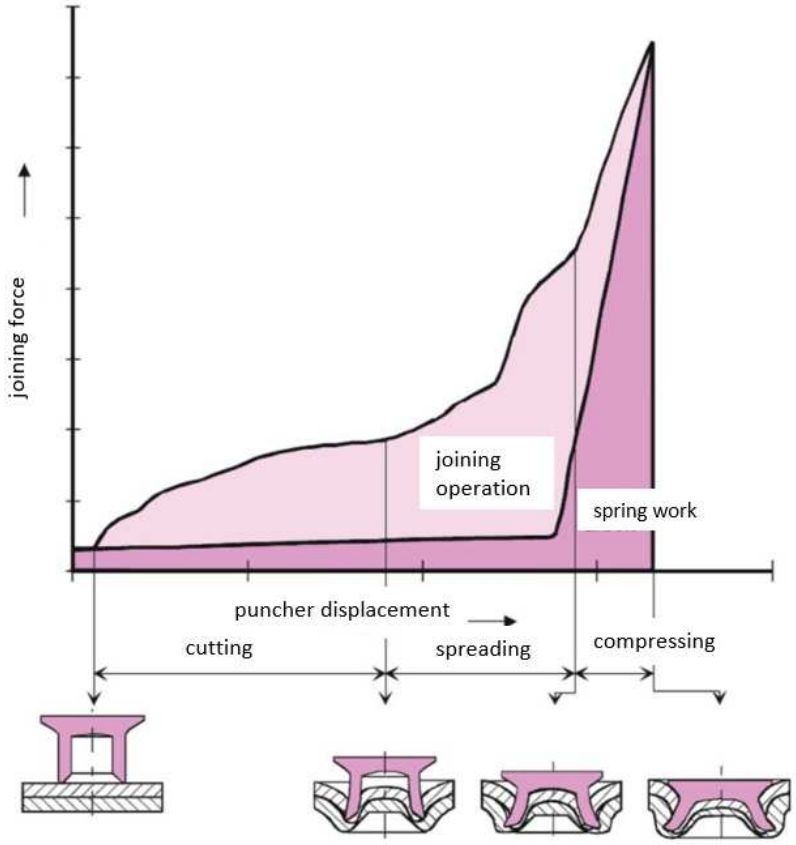

Figure 31 Force-displacement curve of processing a rivet connection [13]

The shape of the force-displacement curve can be affected by [28]

- rivet geometry
- die geometry
- material type
- sheet thickness

3.2.2 Microsection of an SPR

The eccentricity of the rivet plays a major role in the mechanical strength of the SPR connection. It is the difference between the central axis of the rivet and the closing head. During the process, the working force is very high, and because of the elasticity of the system, some deviations (regarding the central axis) can occur which have a strong influence on the riveting process. The effect of the eccentricity is shown in Figure 32 to 34, where the pressure applied is 230 bar [6].

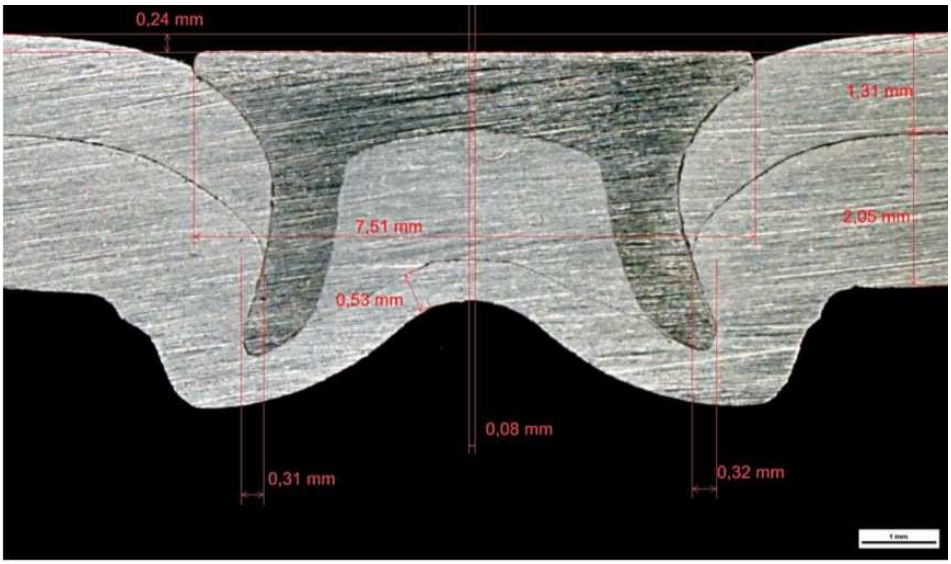

Figure 32 Microsection of a symmetric SPR [6]

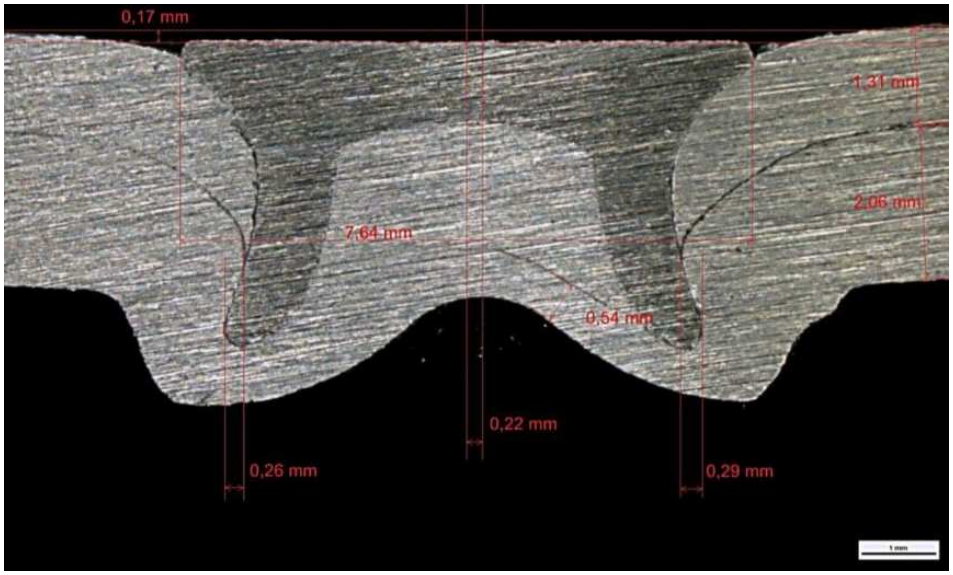

Figure 33 Microsection of SPR with an eccentricity of 0.2mm [6]

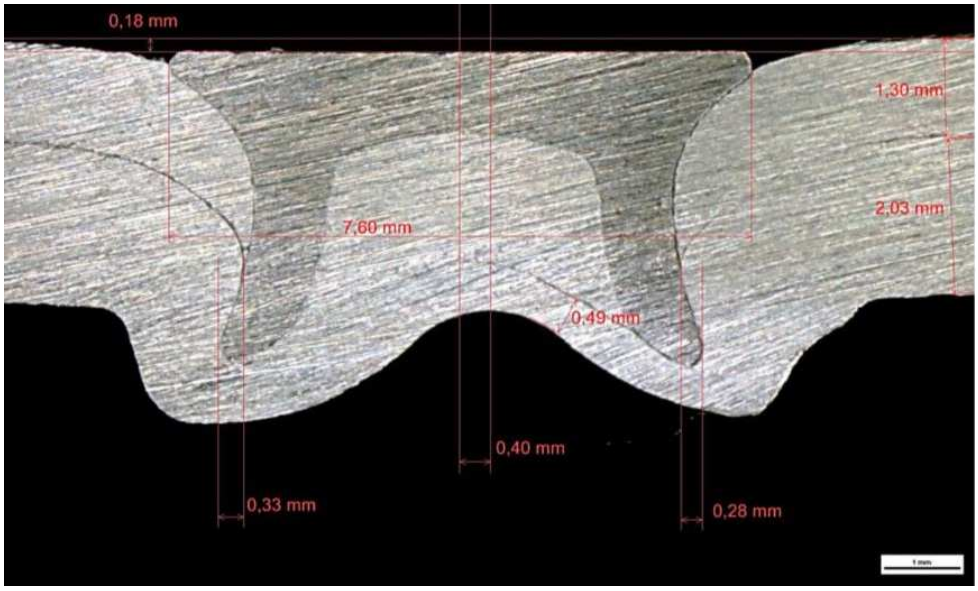

Figure 34 Microsection of SPR with an eccentricity of 0.4mm [6]

In the microsections, different eccentricity values are shown. As the pictures illustrates, the eccentricity of the SPR changes the horizontal interlock and also reduces the residual wall thickness. [6]

3.3 Destructive testing

A destructive test is necessary to check the strength of the joint. Two or more metal sheets are joined and for example an axial tension or shear tension test is performed. In the next sections, the sample and the two tests are described.

3.3.1 KS2 sample

A sample called the KS2 sample is used for the destructive test. There are two different test settings: the shear tension test and the axial-tension test. The sample is made up of an upper and a lower U-shaped aluminium sheet (6000 series aluminium alloy). In the present case, the upper sheet has a thickness of 1.3mm, and the lower sheet has a thickness of 2.0mm. These two aluminium sheets are connected using SPR. Each sheet also has two drilled holes where it is connected to the testing machine [6]. The KS2 sample is illustrated in Figure 35.

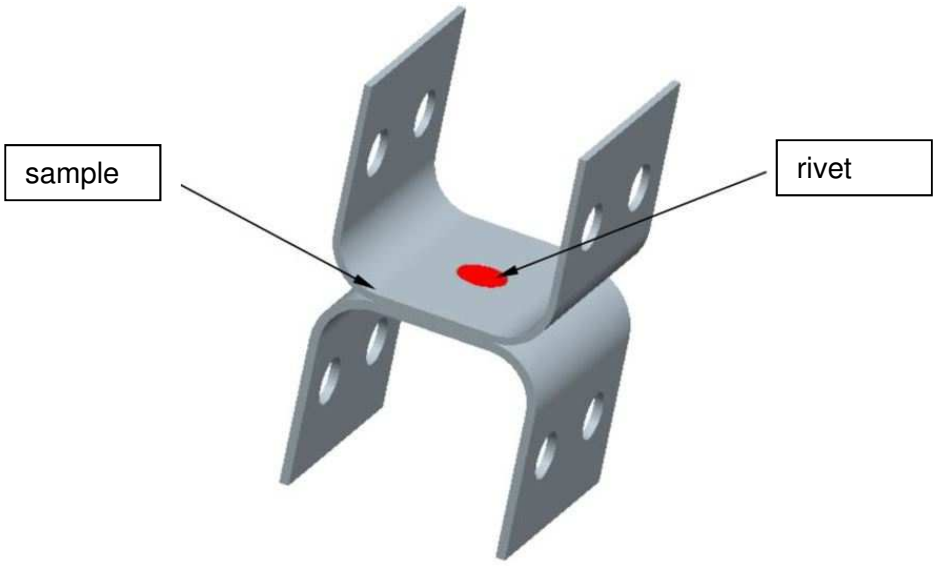

Figure 35 KS2 sample for destructive test [6]

3.3.2 Axial-tension test

The axial-tension test, illustrated in Figure 36 (a), is a quasi-static tension test with a test velocity of 10mm/min. The legs of the U-shaped sheets are pulled apart in the direction of the rivet axis. During the test, the force and also the displacement of the sample are measured. With these two parameters, the force-displacement diagram of such a connection is created, which is shown in Figure 36 (b). The diagram shows the maximum tension strength which this connection can withstand in axial direction, and the energy absorption capacity can also be derived from this graph. The integration of the force curve over the displacement leads to the energy-absorbing capacity of the connection, which can imply the mode of failure during an abrupt load. A low energy-absorbing capacity means that the connection has a tendency towards an abrupt failure by overload. If the absorbing energy is high, the components will plastically deform (absorbing energy), and the possibility of abrupt failure is low [6].

Test data for the axial-tension test includes [6]:

- Diameter of rivet ~ 5.30mm
- Length of rivet ~ 4.50mm

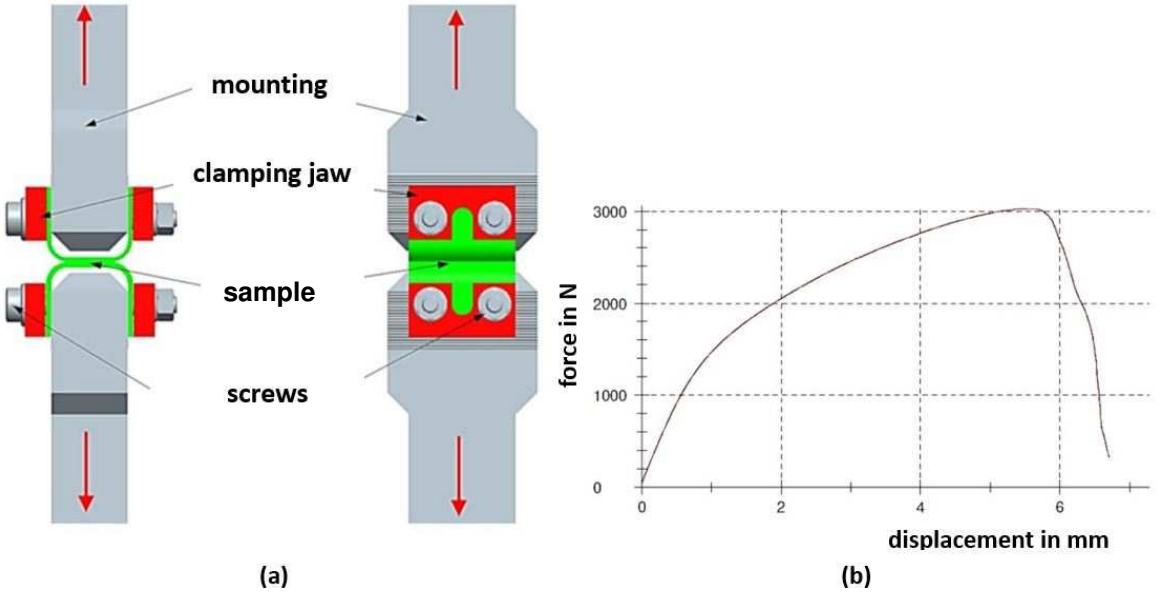

Figure 36 (a) Test setup for axial-tension test, (b) result of the test [6]

For the parameter set used, this connection has a maximum tension strength of about 3kN, and the displacement at failure is 5.5mm. With adhesive between the aluminium sheets, the energy-absorbing capacity would be much higher, which is shown in Figure 29.

3.3.3 Shear tension test

The shear tension test, illustrated in Figure 37 (a), is also a quasi-static tension test. The load is applied perpendicular to the center axis of the rivet, which causes a shear load to the rivet [6].

In this test case, the force and displacement are measured. As a result, the force-displacement diagram of such a connection is created, which is shown in Figure 37 (b). The diagram shows the maximum shear strength which this joint can withstand in a perpendicular direction. Again, the energy absorption capacity can be derived from the graph below [6].

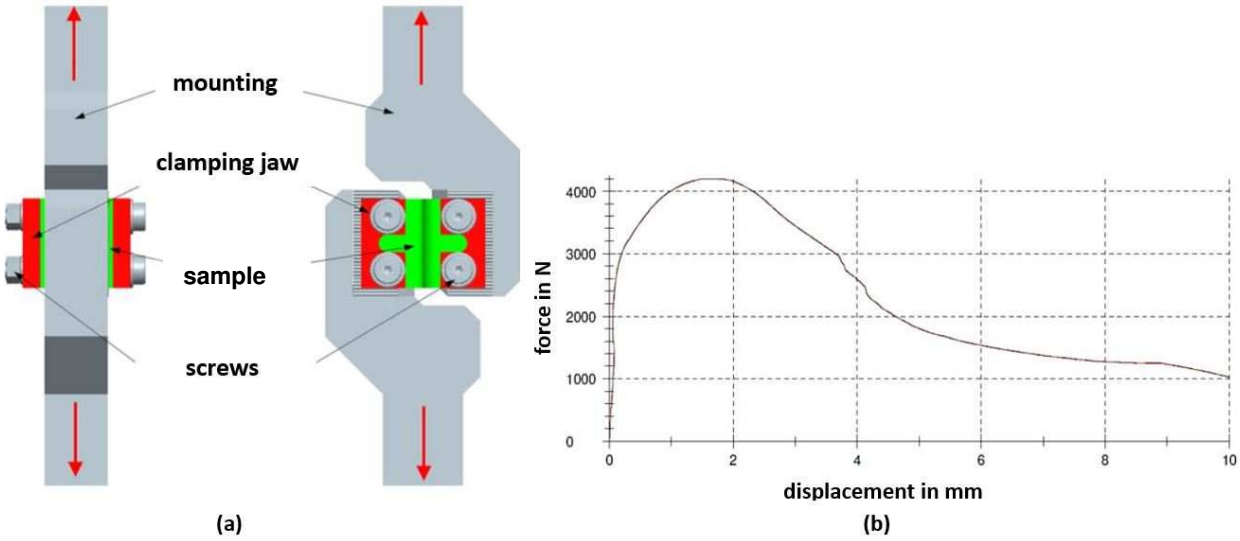

Figure 37 (a) Test setup for shear tension test, (b) result of the test [6]

The graph on the right shows a peak with a maximum of ~4.1kN at a displacement of ~1.8mm. After that, the force drops to a lower level. The force will not reach 0kN because, after the failure of the connection, the rivet gets jammed between the two sheets. Thus, the test itself ends after reaching the maximum force peak, and therefore the values for the energy-absorbing capacity should be used in that range [6].

4 FINITE ELEMENT METHOD

This chapter describes the importance of the numerical simulation for the development of new components. Furthermore, one main purpose of this chapter is to explain the steps performed to set up a numerical simulation. For this thesis, the solver LsDyna is used, and some of its functions are discussed.

4.1 Introduction

The numerical simulation has a huge impact on the development of new products, especially in the fields of aerospace, automotive, biomedical, consumer goods, energy, electronics, heavy industry, and marine. Today, the keyword is computer-aided engineering (CAE), which combines mechanical design with computer-aided design (CAD) and the simulation area like finite element analyses (FEA) or computational fluid dynamics (CFD). With the help of such computer-supported programs, new products can be developed in a short time, costs can be reduced, and companies can stay competitive more easily. Numerical simulation helps to develop better products with higher quality. It also reduces the number of prototypes and conserves resources such as materials.

In terms of mechanical strength, stiffness, and durability, the components can be investigated in the early stage of development. Although the performance of the simulation is very high, experiments must be done to validate the numerical results. Incorrect boundary condition or wrong material condition, for example, are mistakes which can happen in the pre-processing stage, where the simulation model is developed.

Numerical simulation is used for:

- structural investigation (stiffness, stress, instabilities)
- crash simulation (front crash, side crash, dummy simulation, etc.)
- fluid simulation (flow around the vehicle or in the vehicle, etc.)
- noise, vibration, harshness (NVH) simulation
- process simulation (joining, drilling, deep drawing, etc.)

In Figure 38, different forms of simulation are visualised. In (a), a deformed vehicle front from a front crash simulation is illustrated; in (b), a fluid simulation around a car is depicted; and in (c), a simulation result of a side panel of an automotive vehicle is shown.

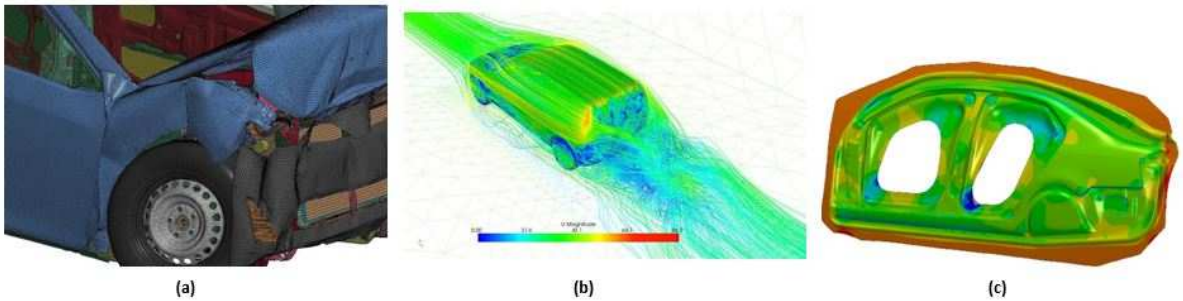

Figure 38 (a) Crash simulation [27], (b) fluid simulation [27], (c) process simulation [26]

4.2 FEM setup

The following sections describe elements of the FEM mesh and the differential equations to solve a numerical simulation.

4.2.1 Elements and mesh

For the setup of a FEM model, CAD data are used. The FEM model is generated by creating a mesh from the CAD geometry, which happens in the pre-processing phase. In the first step, the mesh is created by discretisation of the component, which means that the geometry is divided into finite elements. The FEM mesh consists of nodes and elements. In Figure 39, the available elements are illustrated. With those elements, the mesh is generated from the CAD geometry.

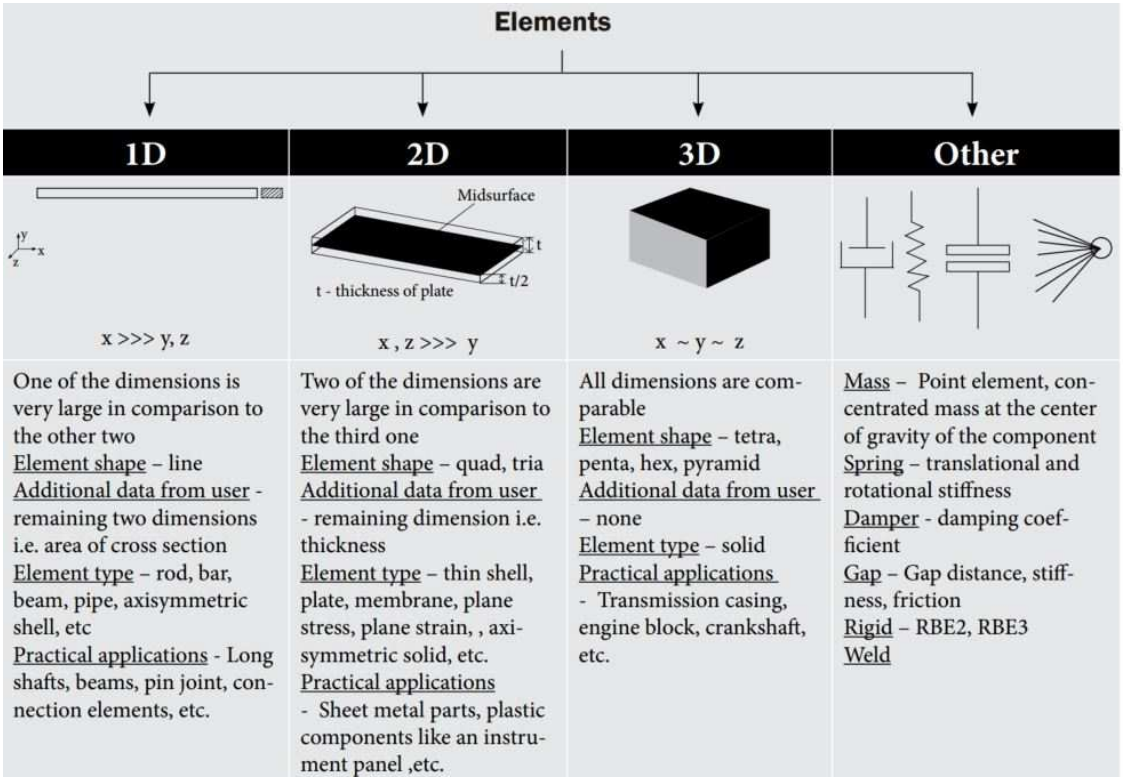

Figure 39 Types of finite elements [23]

One-dimensional (1D) elements e.g. beams which have two nodes, and those nodes are connected with a line (beam). In 2D elements, two dimensions are very large compared with the third one; they have three or four nodes, and the elements which connect the nodes are called tria or quad elements. As an additional input, the thickness of 2D elements must be provided by the user. 3D elements are used if the dimension of the solid element is approximately constant in all dimensions [23]. The different elements for discretisation are illustrated in Figure 41. An example of a meshed part is shown in Figure 41, where various elements are used.

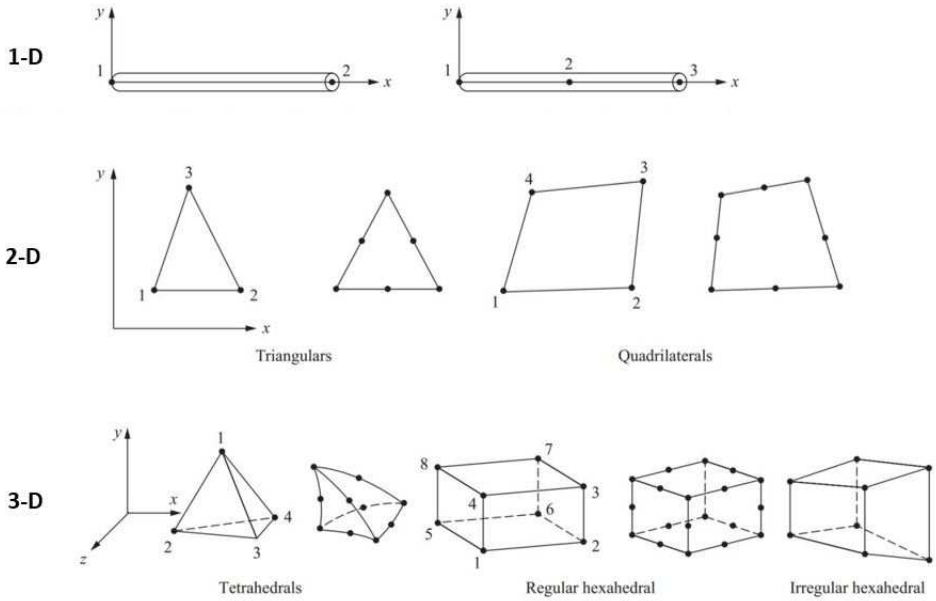

Figure 40 Finite elements for discretisation [24]

It is also possible to use elements of higher order. Therefore, an extra node in between the two boundary nodes is implemented. With elements of higher order, the numerical solution is more precise, but the calculation time will increase.

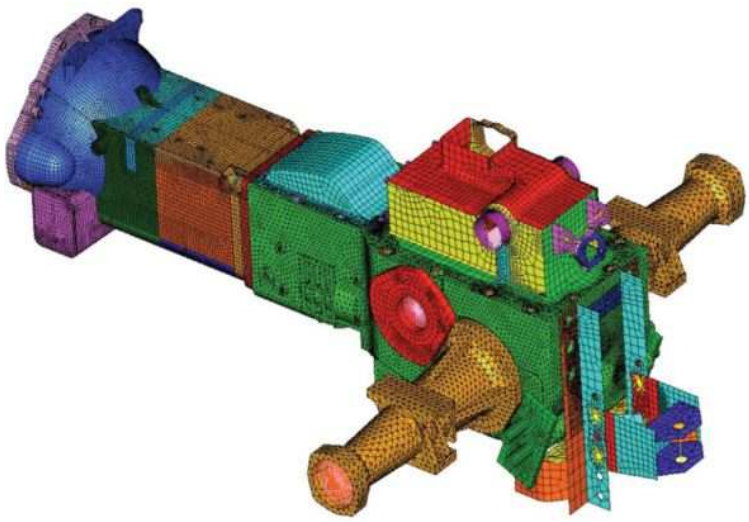

Figure 41 Mesh example of a drive train [23]

Based on the type of analysis different elements are used, for example [23, page 112]:

- *Structural and fatigue analysis – Quad or hex elements are preferred over trias, tetras and pentas.*
- *Crash and nonlinear analysis – Priority to mesh flow lines and brick elements over tetrahedron.*
- *Mould flow analysis – Triangular element are preferred over quadrilateral.*
- *Dynamic analysis – When the geometry is borderline between the classification of 2D and 3D geometry, 2D shell elements are preferred over 3D. This is because shell elements being less stiff, capture the mode shapes accurately and with a fewer number of nodes and elements.*

The mesh size has a big influence on the quality and calculation time of the simulation. A finer mesh causes a higher calculation time, and a rough mesh reduces the calculation time. For areas with higher importance, a finer mesh should be used; otherwise, the mesh could be rough to reduce the elements and nodes (reduce simulation time).

The following steps must be fulfilled to get a numerical solution:

- create a mesh (nodes, elements)
- implement material data (elastic material: elastic modulus, density, Poisson's ratio at least)
- load (force, moment)
- boundary conditions (locking of degrees of freedom)
- contact conditions (with more parts present)

4.2.2 Equation

The elements are directly connected to other elements by shared nodes. With knowing the stress/strain properties of the material, the behaviour of the node can be determined. Each node can be described by an equation (eq. 4.1, [23, page 438]), and the set of equations of all nodes can be expressed in matrix notation.

$$M \cdot \ddot{u} + D \cdot \dot{u} + S \cdot u = f \tag{4.1}$$

M mass matrix

D damping matrix

S stiffness matrix

$\ddot{u}$ acceleration vector

$\dot{u}$ velocity vector

u displacement vector

f external forces

To solve the equation of motion, a time integration method is needed. At the initial time t_0, all parameters are known, and the parameters at a later point in time must be found ($t_0 + \Delta t$). The time integration methods can be divided into explicit and implicit.

Implicit integration method [25, page 7]

The main advantage of the quasi-static implicit finite element formulations is that equilibrium conditions are checked at each increment of time in order to minimize the residual force vector to within a specified tolerance. The main drawbacks in the quasi-static implicit finite element formulations are summarized as follows:

- *Solution of linear systems of equations is required during each iteration;*
- *High computation times and high memory requirements;*
- *Computation time depends quadratically on the number of degrees of freedom*

Explicit integration method [25]

The explicit method does not check the equilibrium demands at the end of each step size of time. This method is conditionally stable whenever the step size of time Δt fulfils the following equation (eq. 4.4):

$$\Delta t \cdot c = l \tag{4.2}$$

$$c = \sqrt{\frac{E}{\rho}} \tag{4.3}$$

$$\Delta t = l \cdot \sqrt{\frac{\rho}{E}} \tag{4.4}$$

where l is the length of the smallest finite element, E is the elastic modulus, ρ the density of the material, and c the velocity of propagation of a longitudinal wave in the material. The step size is normally very small to fulfil equation 4.4. This means that the simulation time would be very long and not efficient. Mass scaling can be performed to speed up the calculation time and increase Δt. This means by increase the density the speed of the longitudinal wave in the material decreases and the time step increases.

The problem with mass scaling is that the mass of the component also increases, and if a dynamic simulation is performed, the energy is incorrect. For example, by performing a crash simulation

with a vehicle into a rigid wall, the mass of the vehicle increases dramatically, and the deformation in the simulation would be higher than in real time due to the kinetic energy.

With the help of a post-processing program like Hyperview or LsPrePost, the numerical solutions can be displayed on the screen. Stress, deformation, and acceleration/velocity of parts or nodes can be visualised.

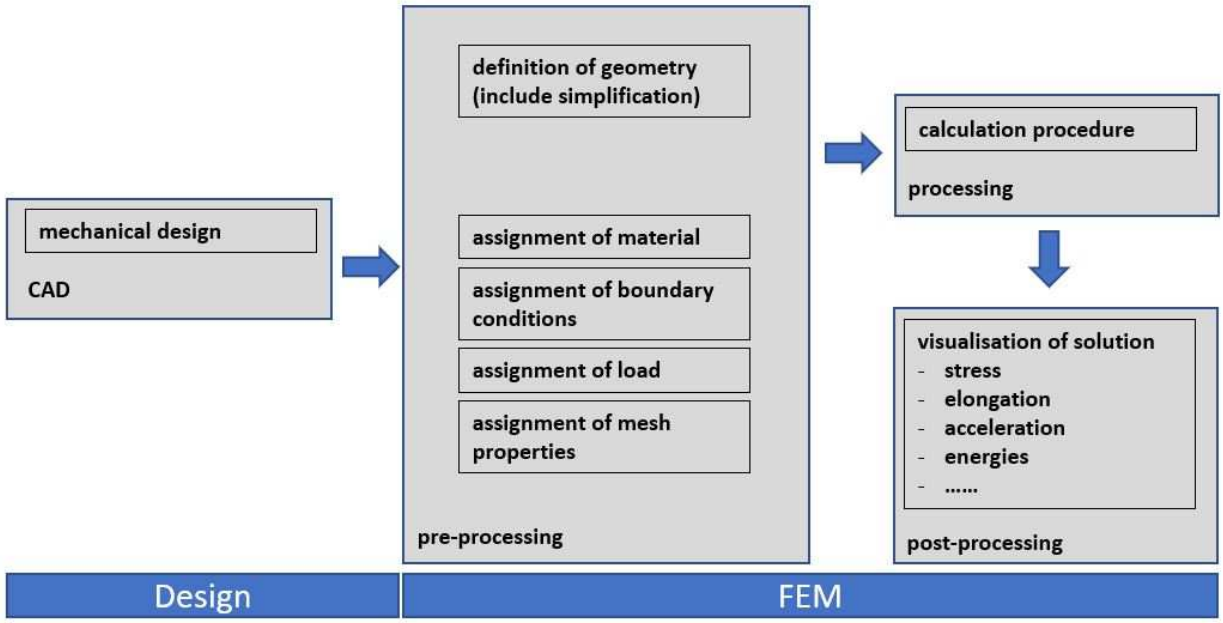

Figure 42 Structure of a FEM

4.3 FEM software LsDyna

In this thesis, the software LsDyna was used for the investigation. LsDyna is a finite element program for simulating complex problems and is used in the automobile, aerospace, construction, military, manufacturing, and bioengineering industries. It was developed by the Livermore Software Technology Corporation (LSTC). The code was developed for dynamic finite element analyses which use explicit time integration [35].

4.3.1 Contacts in LsDyna

A contact in LsDyna is defined via parts, part sets, segments, or node sets. In every time step, the contact algorithm in LsDyna checks for possible penetration from slave nodes due to a master segment (the contacts of different parts are defined as master-slave contact). This means that slave nodes cannot penetrate the master surface. If a penetration is detected, a force proportional to the depth of the penetration is applied and eliminates the penetration. That is how the penalty-

based contact in LsDyna works, and most of the contacts are penalty based. Otherwise, constraint-base contacts without penetration are used. A method to define contacts in LsDyna is, for example, a single contact, which handles every possible contact situation in the simulation. Implementation of some redundant contacts, such as different kinds of contacts with the same contact partner, can lead to numerical instabilities. LsDyna has numerous contact models for different situations, and defining the correct contact is crucial for the accuracy of the simulation [33].

Penalty-based method

As described, this method uses contact stiffness and creates a force when penetration occurs. It can be imagined that this method works like springs, as illustrated in Figure 43 [34]. The contact force is calculated with the following equation (eq. 4.5):

$$F = k \cdot g \tag{4.5}$$

k…contact stiffness

g…penetration depth

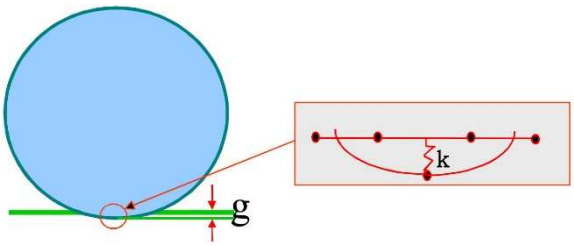

Figure 43 Penalty-based contact [34]

The contact stiffness must be defined. This can be done by a flag in the contact card. LsDyna has different input variants, such as standard penalty formulation, soft constraint, and segment-based. If the stiffness is too high, it could lead to numerical instabilities because of high contact vibrations in explicit calculations. On the other hand, if the stiffness is too low, the penetration is too high.

Contact friction

In LsDyna, one possible model to calculate the contact friction is shown via equation 4.6 [31]. The coulomb friction model used is a function of pressure and velocity of the interface.

$$\mu = FD + (FS - FD) \cdot e^{-DC \cdot |v_{rel}|} \tag{4.6}$$

$FS\ldots$ static coefficient of friction

$FD\ldots$ dynamic coefficient of friction

$DC\ldots$ exponential decay coefficient

$v_{rel}\ldots$ relative velocity of the surfaces

The relationship between the sliding velocity and the friction coefficient is described mathematically in the upper equation, using the parameters FD, FS, and DC.

In the next section, some important contact definitions which were used in this thesis are described.

- **Single surface**

There is no master surface defined, only slave surface, typically as a list of parts. The contact is defined amongst all the parts in the slave list, and self-contact is also included. These types of contact are very stable and accurate and are widely used in LsDyna [33].

The most popular ones are:

*CONTACT_AUTOMATIC_SINGLE_SURFACE

(the automatic options can detect penetration coming from either side of an element)

*CONTACT_AIRBAG_SINGLE_SURFACE

(for folded airbags which are deploying; time-consuming)

- **One-way treatment of contact**

In the definition of one-way contact, only the slave nodes are checked for penetration against the master surface. If the master surface is a rigid body, such a contact definition is used, e.g., for a punch in a setting process of SPR. This definition can also be used for deformable parts with fine mesh on the slave side and coarse mesh on the master side. Other applications are shell to edge or beam edge to surface [33]. The most common are:

*CONTACT_NODES_TO_SURFACE

*CONTACT_ONE_WAY_SURFACE_TO_SURFACE

*CONTACT_FORMING_NODES_TO_SURFACE

- **Two-way treatment of contact**

This contact definition works the same way as the one-way contact, but the difference is a symmetric treatment of the master and slave surface, meaning that the master nodes are checked for penetration against the slave surface and vice versa. Those contacts are about twice as slow as the one-way definition, and therefore the simulation time increases. [33]. The most popular are:

*CONTACT_AUTOMATIC_SURFACE_TO_SURFACE
*CONTACT_SURFACE_TO_SURFACE

- **Tied contact**

In this contact definition, the slave nodes are constrained (fixed) to the master surface, which means that they move with it. At the beginning of the simulation, the slave nodes look for the master surface and then move to it. As a result, the initial geometry can change a little. With the implementation of the 'offset' option, the slave nodes do not move to the master surface, and therefore there is no modification of the initial geometry [33]. Examples for this definition are:

*CONTACT_TIED_NODES_TO_SURFACE
*CONTACT_TIED_NODES_TO_SURFACE

*CONTACT_TIED_NODES_TO_SURFACE_OFFSET
*CONTACT_TIED_SURFACE_TO_SURFACE_OFFSET

4.3.2 Materials in LsDyna

Approximately three hundred different material models are integrated in LsDyna. Some material models can only be used for beam (1D), shells (2D), or solids (3D). There are also some special material models for foam, steel, composites, plastic, and so on. The following section describes the important ones for this thesis.

- ***MAT_PIECEWISE_LINEAR_PLASTICITY**

This is LsDyna material type 24. It is an elastic-plastic material model whereby an arbitrary stress-strain curve can be defined. In this material, a strain rate dependency can also be implemented. The material definition can handle failure by implementing the failure strain. That means by reaching this value, the element will be deleted [36].

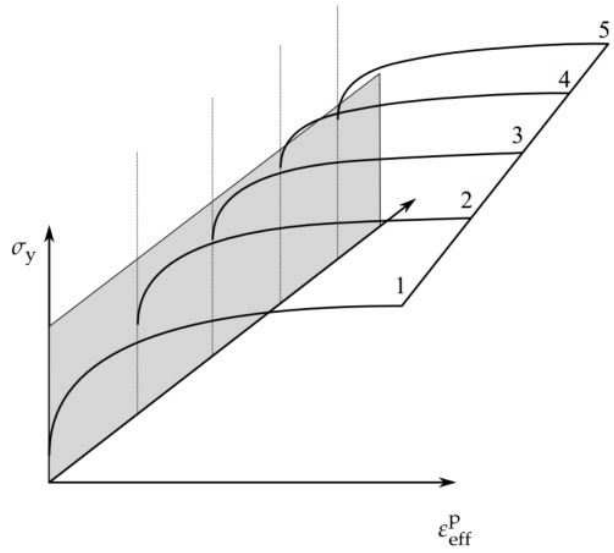

Figure 44 Material 24 stress-strain behaviour [36]

- ***MAT_PLASTICITY_WITH_DAMAGE**

This is LsDyna material type 81. It is an elastoviscous-plastic material model wherein a stress-strain curve was implemented, and this model is also strain-rate dependent. The failure mode in this material model is more focussed on the effects of the damage than the rupture. It includes a parameter where failure begins, without a rupture of the material; this point is called the softening point. A second value for the effective strain is implemented where the deleting of the element (rupture) occurs [36].

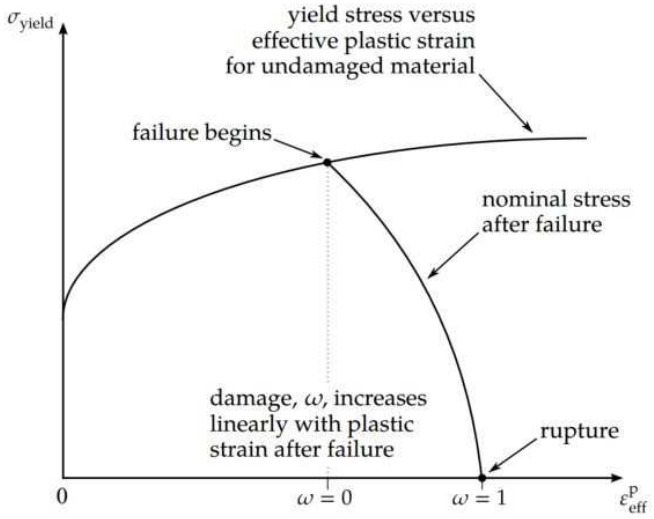

Figure 45 Material 81 stress-strain behaviour [36]

- ***MAT_RIGID**

This is LsDyna material type 20. Parts which are described with this material model are rigid. That means these parts cannot be deformed. For the material definition, only the density, elastic

modulus, and Poisson's ration must be defined. The E-modulus and Poisson's ratio are needed for the contact definition. This material model can be used for beams, shells, and solid elements. There are often parts in a FEM simulation which are defined as rigid to save, for example, calculation time. In metal sheet forming, the tools or dies can be modelled as rigid parts because they should not deform during the simulation. Those parts are crucial for the simulation, and therefore they must be integrated in the model. The moment of inertia of such parts is calculated from the geometry, or the user can implement these parameters. In the material input, constraints can also be defined, e.g., the part is moving in the z-direction, and the other directions (for example, x-, y-, x_{rot}, y_{rot}, and z_{rot}) are locked [36].

4.3.3 Material data for simulation

The aluminium alloy used for this thesis was investigated at Graz University of Technology during the doctoral thesis of Florian Hönsch. To define the elastic plastic properties of the used material, some uniaxial tensile tests were performed. From the true stress-strain curve, the flow curves were derived. The curve is marked in orange in the left picture of Figure 46. For the plastic-strain behaviour beyond 0.2, the Hockett-Sherby [39] material model is used. The Hockett-Sherby model was adapted with a linear term to correctly consider the strain hardening in the area over 0.5 of plastic strain (Figure 39 below, left picture, blue line). In grey, the classic Hockett-Sherby model is illustrated, where the hardening effect is not really present. Also, the material properties of the rivet are investigated in the doctoral thesis. The picture below (right side) illustrates the flow curve of the steel rivet. This curve is implemented in the numerical simulation model [38]. In Table 1, the parameters for calculating the flow curves are illustrated.

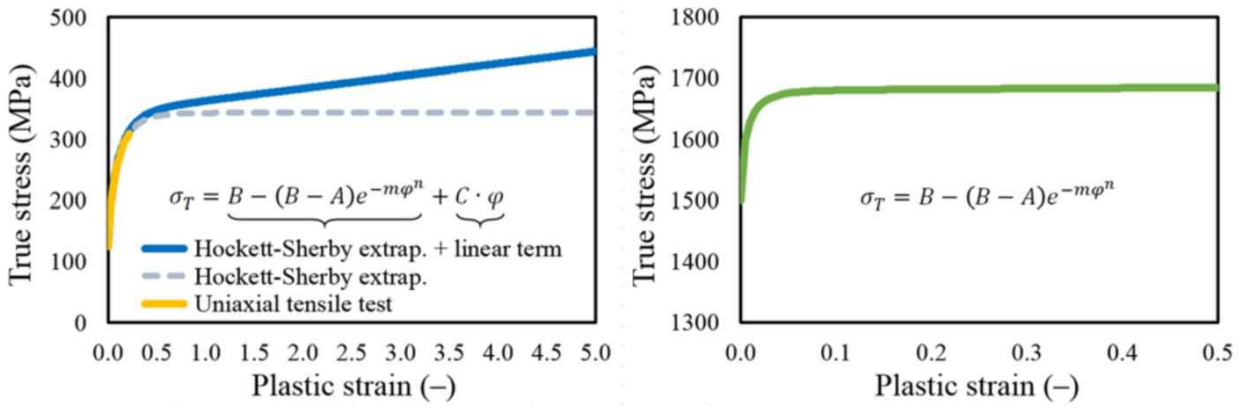

Figure 46 Adapted flow curves of aluminium blank (left) and steel rivet (right) [38, page 3]

Table 1 Parameter for flow curves [38, page 3]

	A	***B***	***C***	***m***	***n***
metal sheet	*125*	*340*	*20*	*6.5*	*0.82*
steel rivet	*1500*	*1680*	*-*	*25*	*0.65*

Summary of the chapter

This chapter included the main points for a numerical FEM simulation. Furthermore, the operation of contacts between components have been described. Moreover, the material data used for the FEM simulations in this paper were discussed.

5 TWO-DIMENSIONAL SPR PROCESS

This chapter describes the different steps to create a 2D axisymmetric model of the SPR process. The 2D simulation results are used as an input for a 3D model, which was created by rotating the 2D model. Also, the stress and strain patterns of the 2D model were mapped onto the 3D model with the help of HyperWorks [29], a powerful pre- and postprocessor (HyperMesh, HyperView, HyperGraph).

5.1 Geometry and mesh

Geometry

The geometry of the rivet is based on the measurement of multiple cross-sections of SPRs. In another project, the experiments for the validation of the simulation results were conducted. The dimensions of the rivet and die are illustrated in Figure 47 and Figure 48. The rivet itself has a height of 4.5mm, the diameter of its legs is about Ø 5.49mm, and the rivet head has a diameter of Ø 7.8mm.

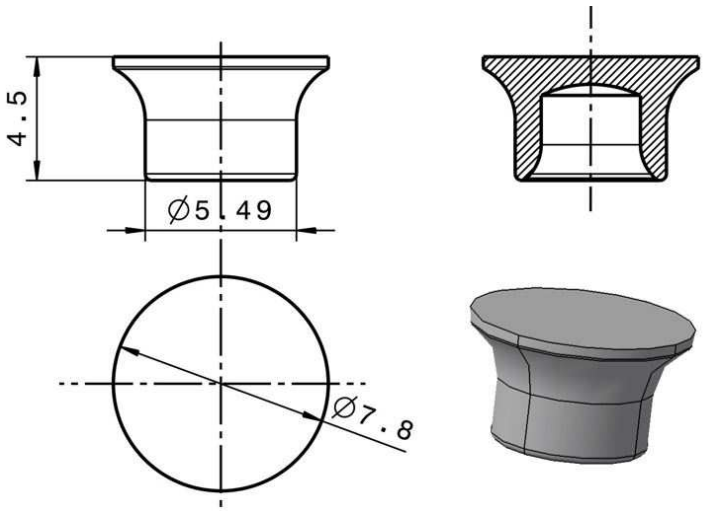

Figure 47 Different views of the rivet [30]

The die itself has a height of 10mm and an outer diameter of Ø15mm. The cavity of the die has a special form to ensure that the rivet is spreading enough. The two aluminium sheets, which are joined, have a thickness of 2mm (lower sheet) and 1.3mm (upper sheet).

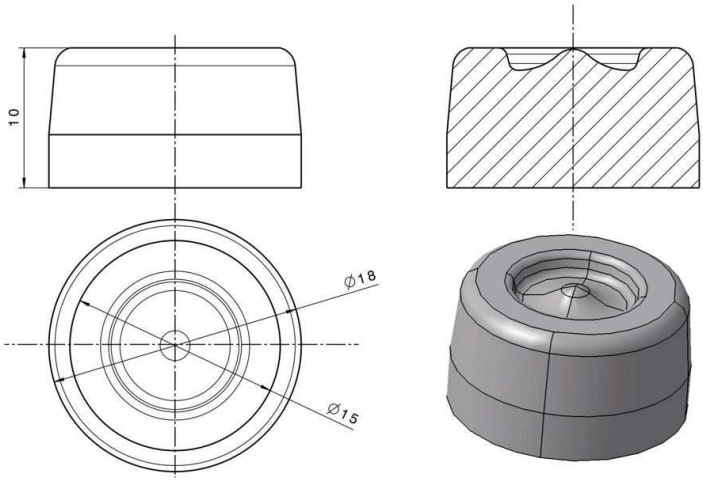

Figure 48 Different views of the die [30]

Mesh

A mesh is generated from the geometry, as described in section 0. The size of the elements was determined by trying different mesh sizes. Small elements mean a more accurate simulation but lead to an increase in calculation time. For the 2D setting process of the SPR, a mesh size of 0.1mm was used for the deformable parts. A coarser mesh was used for the punch, the die and the blank holder.

The 2D model consists of the following components:

- punch: defined as rigid because it is much stiffer than the rivet or the aluminium sheets, and therefore, in the experiment, there is no deformation of this part
- SPR: the rivet is defined as a deformable part
- upper and lower aluminium sheets: also defined as deformable parts
- die: modelled as a rigid part (in experiment, no deformation)
- blank holder: also modelled as a rigid part (in experiment, no deformation)

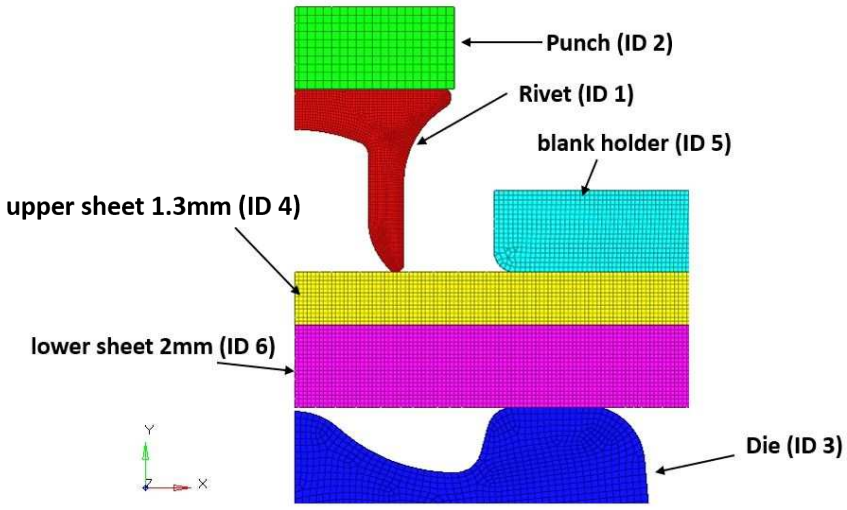

Figure 49 2D axisymmetric model

Due to axial symmetry, only a half model was created, and therefore the calculation time was decreased.

Elements for the mesh

For the simulation, four-node, 2D, fully integrated axisymmetric elements were used (LsDyna element formulation *elform 15* [31]). The element itself is defined as a quad element with four nodes.

Axisymmetric means that the:

- model was created in the x-y plane
- z-coordinates of the nodes are 0
- global y-axis is the symmetry plane

remeshing of the 2D mesh

During the setting process of the SPR, the upper and lower aluminium sheets are exposed to large deformations, which can lead to element distortions. This may reduce the accuracy of the simulation, or the simulation could be aborted. To avoid these problems, an adaptive remeshing method was used. LsDyna uses two different kinds of remeshing: h- and r-adaptive remeshing. For the element formulation used, only the r-adaptive remeshing can be applied.

r-adaptive remeshing:

A completely new mesh is generated which is initialised from the old mesh using a least-squares approximation [31, p. 12–15 (Control)]. In the input data, a characteristic element size is defined, which is used by the algorithm. In the simulation, a periodic remeshing is used to produce a new mesh after a defined time. For the simulation, different remeshing times were investigated, and the time selected was 4ms. Reducing the remeshing time increases the simulation time. To the new generated mesh, the stress and strain from the previous step were mapped. In Figure 50, the remeshing process during the setting simulation at different times is visualised.

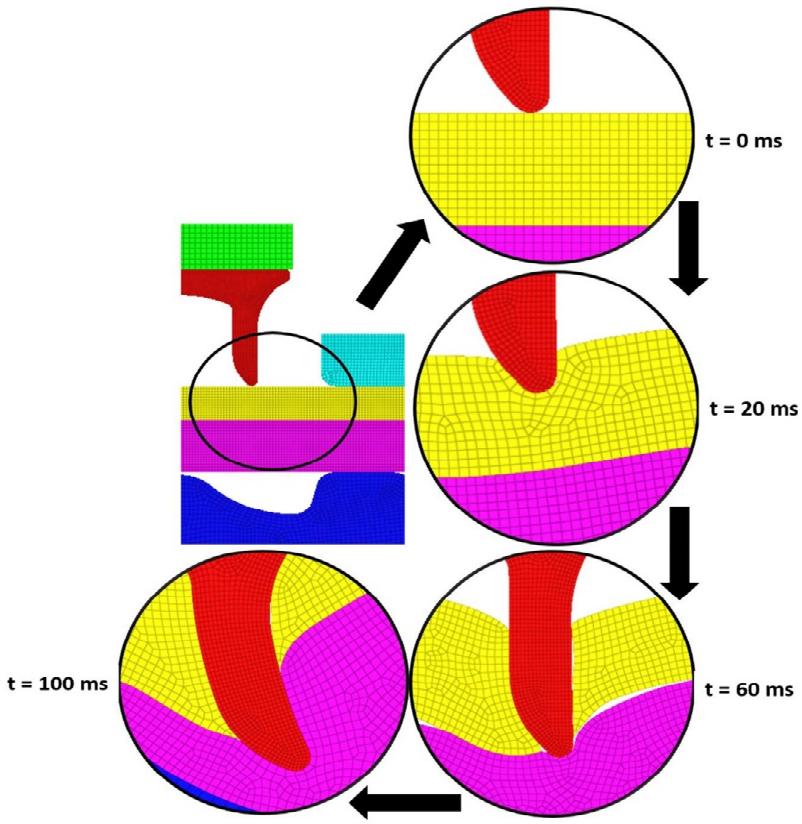

Figure 50 r-adaptive remeshing during setting process

5.2 Contact definition

For all contacts within the simulation, the **CONTACT_2D_AUTOMATIC_SINGLE_SURFACE* – contact was used. This is a special contact for 2D solid and shell elements which uses the axisymmetric formulation. Parts which are in contact are implemented in a part set (slave side). Static and dynamic friction was implemented in the contact card. In Table 2, all contact definitions of the model are summarised. The table consists of the contact ID, the parts which are in contact, and the friction parameters.

Table 2 2D contact definition

ID	Parts in Contact	Static Friction (FS)	Dynamic Friction (FD)
10 000 000	Rivet (ID 1) <--> Upper Sheet (ID 4)	0.12	0.12
20 000 000	Rivet (ID 1) <--> Lower Sheet (ID 6)	0.12	0.12
30 000 000	Blank Holder (ID 5) <--> Upper Sheet (ID 4)	0.2	0.2
40 000 000	Die (ID 3) <--> Lower Sheet (ID 6)	0.2	0.2
50 000 000	Upper Sheet (ID 4) <--> Lower Sheet (ID 6)	0.12	0.12
60 000 000	Plunger (ID 2) <--> Rivet (ID 1)	0.2	0.2

5.3 Material data

For the deformable parts (steel rivet, upper/lower sheet), the material model **MAT_PIECEWISE_LINEAR_PLASTICITY* was used. The material for the aluminium sheets and steel rivet are described in section 4.3.2. For the tools (blank holder, punch, die), the material model **MAT_RIGID* was applied.

In the self-piercing riveting process, the upper sheet was pierced, and therefore a geometric failure criterion was implemented, which means that the element was eroded when the element size was too small. The keyword for that option is **PART_ADAPTIVE_FAILURE*. This option allows for the separation of one part into two parts, and the remeshing can still go on (Figure 51). As an input, the residual thickness of the element was implemented. Different values for the residual thickness were investigated, and the final value was set to 0.1mm, which ensures that the splitting of the part was at the right place. If the value is lower than 0.1mm, then the splitting appeared in other areas, and the overall simulation result was incorrect.

In the material cards, an additional strain failure was implemented because, after the splitting process, element distortion occurred. After reaching the threshold value (3.6), the elements were deleted to avoid numerical instabilities. The defined materials for the different parts are illustrated in Table 3.

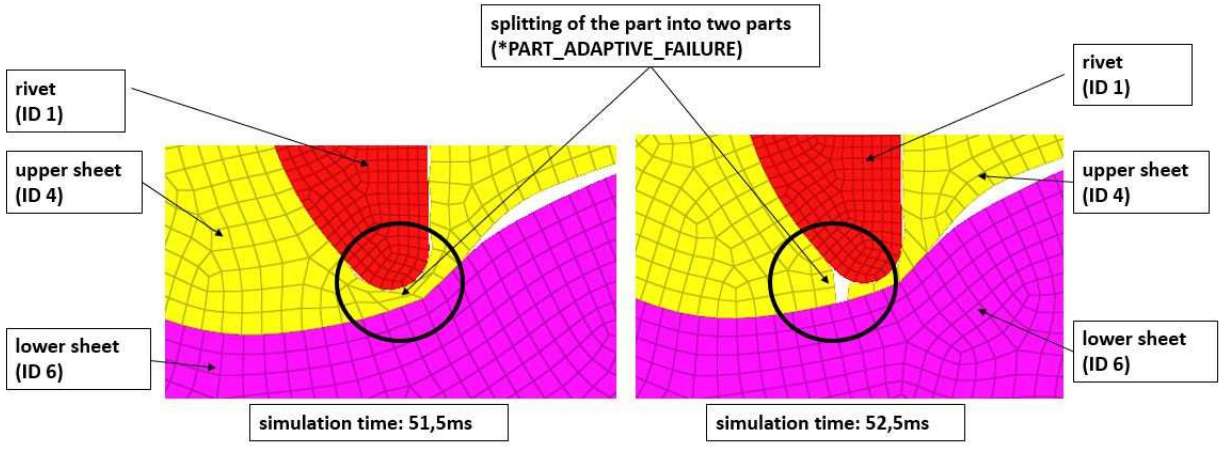

Figure 51 2D part splitting

Table 3 2D material data

Part-Name (ID)	Material ID	Material	Material model	Mass density [kg/mm^3]	Youngs modulus [GPa]	Poisson's ratio	Yield stress [GPa]	Strain failure	Material curve ID
rivet (ID 1)	3	Steel	Mat_24 elastic-plastic	7.80E-06	210	0.30	1.580	-	1000000
punch (ID 2)	1	Steel (rigid)	Mat_20 rigid	7.80E-06	210	0.30	-	-	-
die (ID 3)	1	Steel (rigid)	Mat_20 rigid	7.80E-06	210	0.30	-	-	-
upper sheet (ID 4)	4	Aluminium	Mat_24 elastic-plastic	2.80E-06	70	0.35	0.126	3.6	2000211
blank holder (ID 5)	1	Steel (rigid)	Mat_20 rigid	7.80E-06	210	0.30	-	-	-
lower sheet (ID 6)	4	Aluminium	Mat_24 elastic-plastic	2.80E-06	70	0.35	0.126	3.6	2000211

5.4 Boundary condition and load

There are different boundary conditions and loads integrated in the simulation model. First, the die must be held in place during the setting process. Therefore, all degrees of freedom are locked. This was implemented in the *MAT_RIGID card as described in section 4.3.2. There is also a boundary condition for the punch which pushes the rivet through the aluminium sheet. For that case, the **BOUNDARY_PRESCRIBED_MOTION_RIGID* keyword is used. Another boundary condition is introduced for the blank holder which presses with 10kN against the aluminium sheets and clamps both sheets between itself and the die. The keyword for that is **LOAD_RIGID_BODY*. In the simulation, gravity was accounted for with the keyword **LOAD_BODY_Y*.

- ***BOUNDARY_PRESCRIBED_MOTION_RIGID**

This keyword is used to move the punch down. The punch itself is a rigid body that comes in contact with the deformable rivet. By moving the punch downwards, the rivet is placed properly. Here, the displacement, the velocity, or the acceleration of the punch can be adjusted. The part ID, direction, property (displacement, velocity, acceleration), and value of the property must be implemented. The input information is shown in Table 4. The punch is moving downwards with a constant velocity of about 50mm/s.

- ***LOAD_RIGID_BODY**

The purpose of this card is to apply a concentrated force to the centre of mass of a rigid body. With this option, a constant force is applied to the blank holder. The input is also shown in Table 4.

- ***LOAD_BODY_Y**

The purpose of this card is to add acceleration to all parts in the model. With this acceleration, gravity is simulated, and the field is applied in the y-direction because the model is designed in the y-x plane. The input is also shown in Table 4.

Table 4 2D input for punch movement

Part ID	Degree of freedom	Property	Value
2	y-direction	displacement	-4.575 mm
5	y-direction	force	10 kN
ALL	y-direction	acceleration	9.81 m/s^2

5.5 Result of 2D setting simulation

The next several sections describe the simulation of the 2D setting process. First, the stress and strain field is reviewed, followed by the force-displacement curve and, finally, the comparison between the reality (microsection) and the simulation is shown.

5.5.1 Numerical result of stress and strain field

Figure 52 illustrates the effective plastic strain during the SPR setting process, which is divided into the three process steps (initial, piercing of upper sheet, and final joint). The figure shows that the highest strain value is in front of the tip of the SPR or, more specifically, during the piercing of the upper aluminium sheet. At this point in the simulation, a high plastic strain in the area of 2.6 occurs. After the final step of the processing, the punch moves upwards, and an elastic spring back occurs. The highest plastic strain in the final connection occurs in the area where the upper sheet is in touch with the rivet and the lower sheet. After the upper sheet is pierced, it moves with the rivet into the final position. Also, in the area where the lower sheet touches the die (bulge of the die), a higher plastic strain exists because of the deformation due to the rivet spreading.

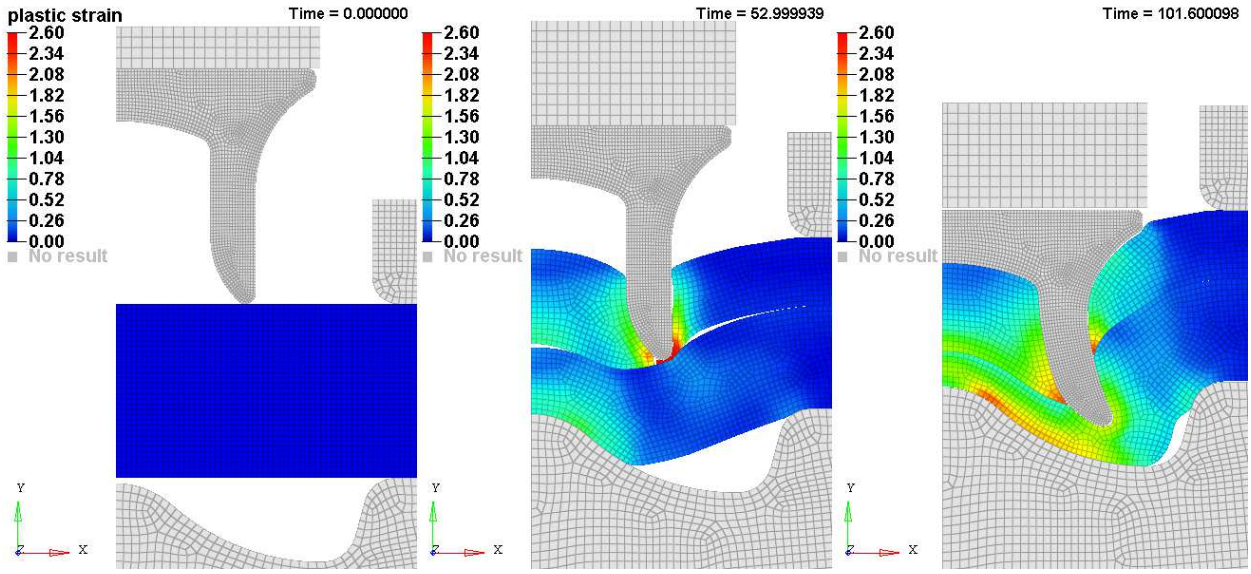

(a) (b) (c)

Figure 52 Effective plastic strain during the three process steps: (a) initial step, (b) upper sheet pierced, (c) final joint [37]

Figure 53 shows the von Mises stress during the self-piercing riveting process, wherein the highest stress in the blanks is in the field of roughly 400MPa. In the final position of the rivet the biggest stress is in the upper sheet on the inner side of the rivet. In this region, a compression of the upper sheet occurs. Another area with higher stress is near the bulge of the die. In that position, the lower sheet is clamped or compressed between the upper sheet and the die, and as a result, higher stress occurs.

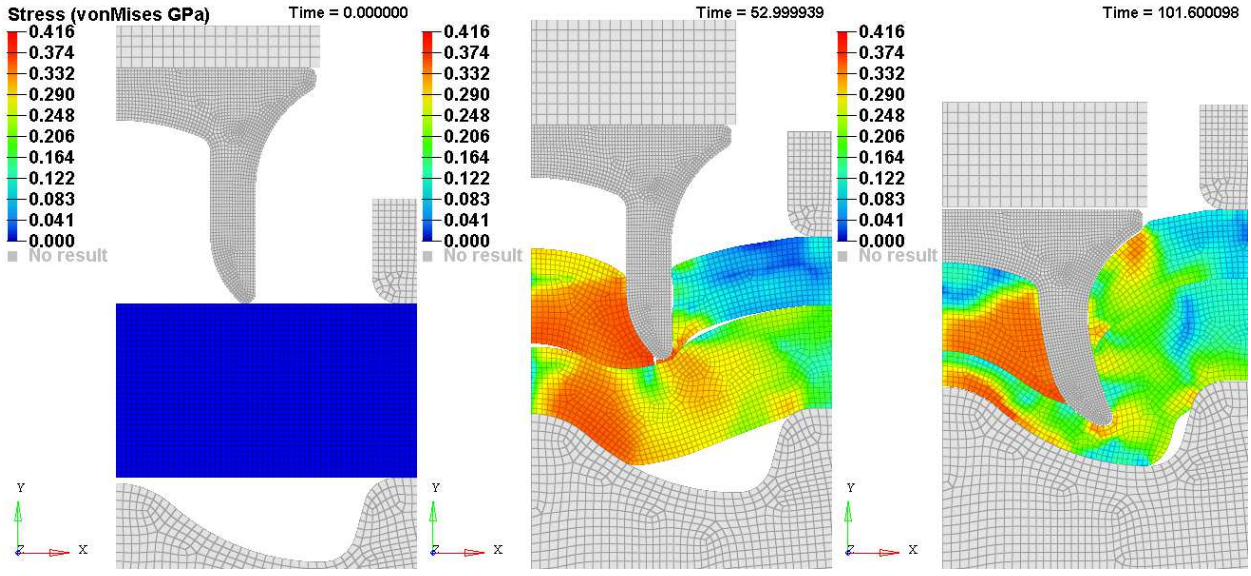

(a) (b) (c)

Figure 53 von Mises stress during the three process steps: (a) initial step, (b) upper sheet pierced, (c) final joint

5.5.2 Force-displacement curve of the 2D process

In Figure 54, the force-displacement curve (described in section 3.2.1) of the punch and blank holder is illustrated. The Figure 54 shows three curves: the one from the FE simulation, a corrected curve from the FE simulation, and the curve from the experiment. The difference between the FE and the corrected curve is the consideration of the stiffness of the tool. In the simulation, the tools are rigid, and therefore no elastic deformation can occur. In the experiment, elastic deformation of the C-frame occurs, and this affects the force-displacement curve, which is visualised in the figure below. For the rivet tool, a stiffness of 25kN/mm was determined [37]. Using this parameter, the original FE curve was corrected.

The cutting and spreading step can be distinguished in the force-displacement curve. The displacement is measured by the movement of the punch. In the first 4mm of the curve, the cutting of the upper aluminium takes place. After that, the spreading of the rivet occurs. The highest force of the setting process for this setup (upper sheet thickness of 1.3mm, lower sheet 2.0mm) is 54kN. The maximum force reached in the experiment is around 51kN.

The corrected curve compared with the real experiment shows a high correlation.

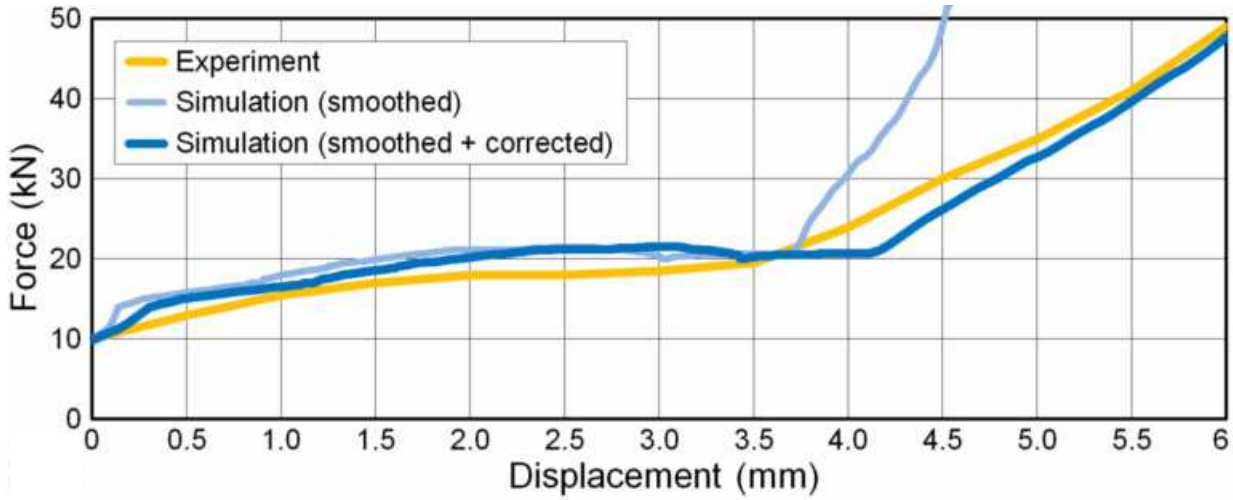

Figure 54 Force-displacement curve of simulation (original and corrected) and experiment [37]

5.5.3 Comparison simulation versus experiment

Figure 55 illustrates the comparison of the experimental deformation and the deformation calculated from simulation. In Figure 55 (a), the microsection of the SPR with the main geometrical features and in (b), the result of the simulation is visualised. The main features are the horizontal interlock, the rivet head overlap, and the residual thickness of the lower sheet. The horizontal interlock in the simulation is 0.35mm versus 0.31mm in the experiment, which is a good correlation. The residual thickness in the simulation is about 0.65mm, which is higher than in the

experiment, with 0.56mm, but this can be influenced by the position of the rivet head. In the simulation, the overlap is 0.0mm versus 0.24mm in the experiment. By adapting the height of the head, the lower sheets residual thickness would be smaller, but the horizontal interlock would be higher. The important comparison value for this simulation is the interlock because the mechanical strength of the joint is strongly dependent on this parameter.

The simulation result has a good agreement with the experiment, as shown in the red encircled area.

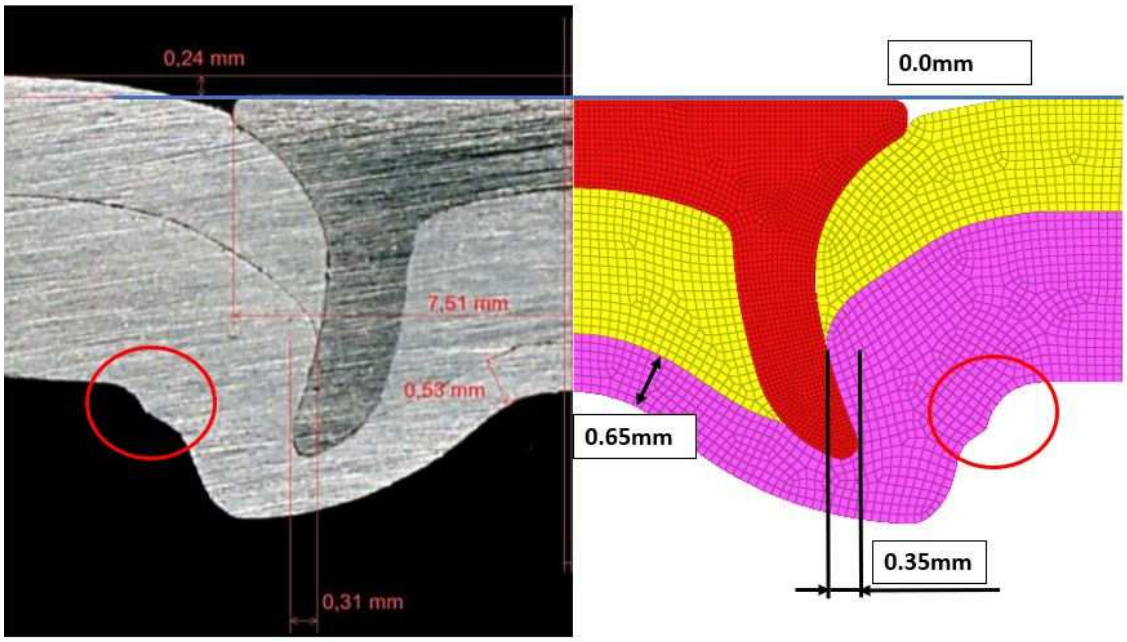

(a) *(b)*

Figure 55 Comparison of experiment (a) and simulation (b)

Based on the presented results, the 2D process simulation is an accurate and fast simulation method for self-piercing riveting. The difference of simulation and experiment occurs because of the friction model and the influence of the material behaviour, e.g., strain rate dependency, simplifications, temperature, etc.

There are also some drawbacks with the 2D simulation, for example, the eccentricity of the rivet or the tilt of the die cannot be investigated. To consider this misalignments, a 3D simulation model was developed (see chapter 6).

5.6 Simulation of the destructive tests

This section analyses the simulation of the destructive tests (described in section 3.3). It is common to perform a 2D setting process simulation and take the simulation result as an input for a 3D destructive simulation. Thus, the results of the 2D simulation, e.g., the effective strain and stress, were mapped onto the 3D model.

5.6.1 Axial tension simulation

Axial tension model

For the destructive axial tension simulation, a 3D model was needed, and the following steps were performed:

- creation of a 3D model from the 2D simulation results
- integration of the 3D model (KS2 sample)
- mapping of the effective strain and stress to the model as initial values

Mapping 2D onto 3D model

After the 2D setting process simulation, the elements and nodes of the 2D results were exported using HyperView and imported to HyperMesh (both products of Altair). In HyperMesh, a 3D geometrical model was created and meshed with hexahedral elements (Figure 56 b, c). Furthermore, the KS2 sample was meshed using CAD data, and the rotated SPR joint was implemented. The different steps are shown in Figure 56. In the simulation model, a symmetry plane was integrated to reduce the simulation time. The symmetry plane (x-y) was generated in the centre of the model, and thus only half a model had to be created. The keyword used was **BOUNDARY_SPC_SYMMETRY_PLANE_SET.*

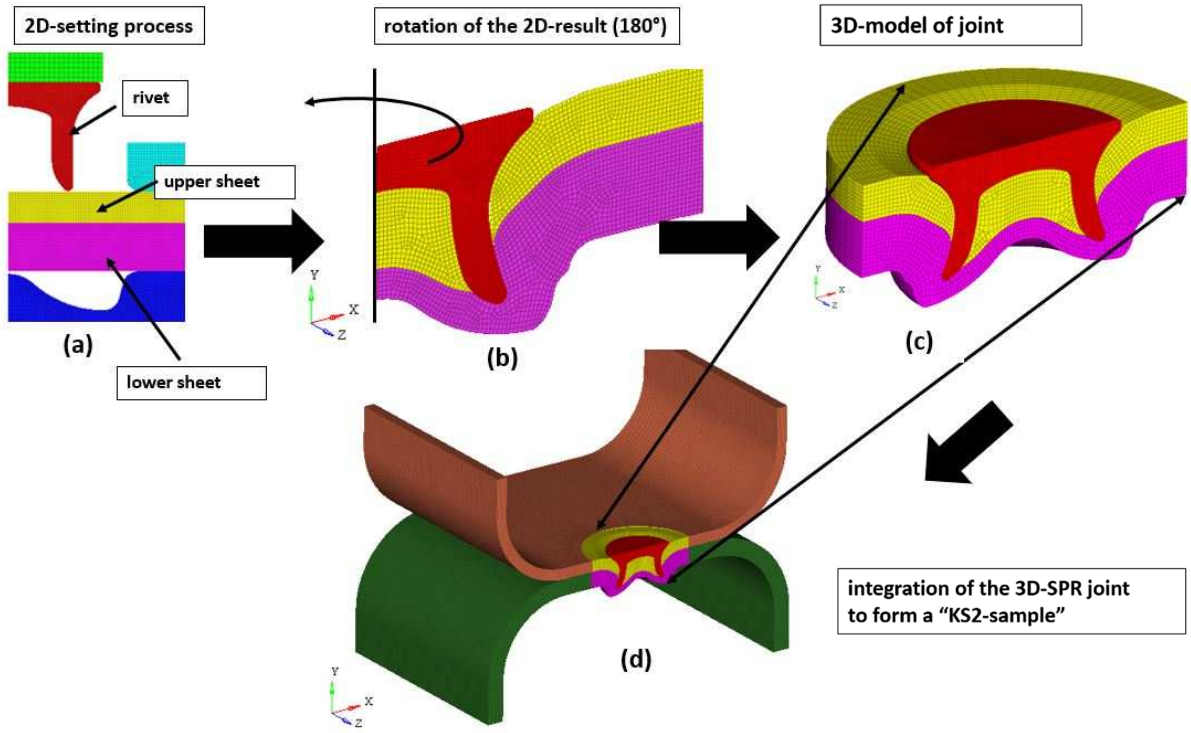

Figure 56 2D to 3D extrapolation to create an axial tensile simulation

After the meshing step, the material and part properties were assigned to the different components. Therefore, the section was changed from a 2D element (shell) configuration to a 3D (solid) formulation. The solid element formulation used was *ELFORM 1,* which is the default type for solid elements.

Boundary conditions for the axial tension test

In the experiment, the sample halves were pulled apart in the direction of the rivet axis as described in section 3.3.2. To get the same movement in the simulation, a **BOUNDARY_PRESCRIBED_MOTION_SET* option was utilised. One was used for the upper sheet and one for the lower sheet. A constant velocity (20mm/s) to both node sets was applied to introduce the load to the SPR joint. The velocity was used to reduce the computing time. The movement of the nodes was defined in y-direction, and the other degrees of freedom were constrained to prevent the displacement of those nodes. The simulation time was 200ms, and therefore the uppermost and lowermost points were moving 4mm in opposite directions. That means the displacement at the end of the upper and lower points was 8mm.

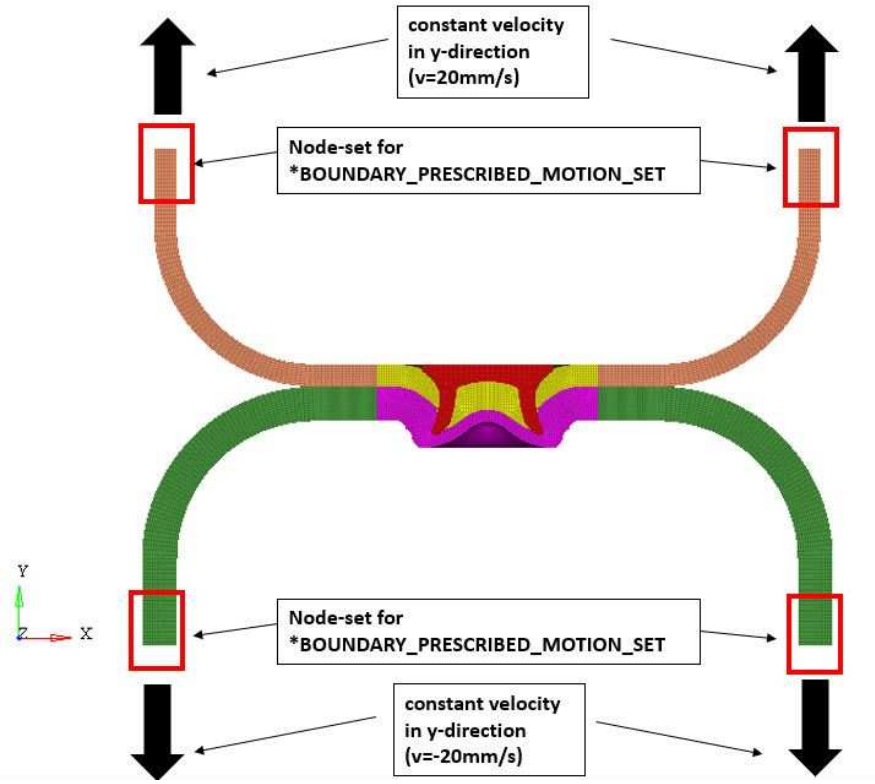

Figure 57 Applied velocity for the axial tension test

Mapping of the initial stress and effective strain field

The option **INITIAL_LAG_MAPPING* was used to implement the effective strain and the stress as initial values from the 2D setting process. With this option, a mapping file was read which was created during the 2D simulation.

Result of the axial tension simulation

Comparison of the deformation

In Figure 58, the destroyed sample from the experiment is compared with the numerical simulation. Figure 58 (a) represents the experiment where the failure of the connection is illustrated. In principle, the rivet can be pulled out of the lower aluminium sheet, or it can be drawn through the upper sheet. In (a), the picture shows the second failure mode (drawn through the upper sheet). In (b), the result of the simulation is illustrated. To create that picture, the result of the half model was reflected around the x-y plane. In (c), the result of the axial tension simulation is visualised. Here, the rivet was also drawn through the upper aluminium sheet. Overall, the comparison of the destructive tension simulation has a high accordance regarding the deformation within the experiment.

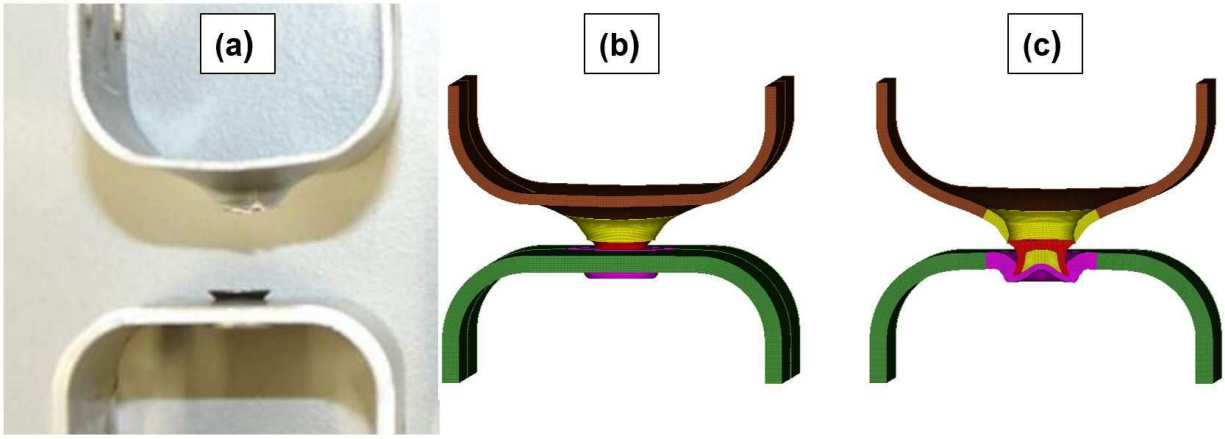

Figure 58 Comparison of the deformation (a) real part [6], (b) simulation, (c) section cut of simulation

Analysis of effective plastic strain and stress (von Mises)

The figures below show the effective plastic strain and stress field. In Figure 59, the effective strain is illustrated in three different time steps: figures (a) to (c) from an overall perspective and figures (d) to (f) from a closer perspective. In figures (a) and (d), the initial conditions are shown. Especially in (d), the mapped effective strain from the 2D setting process is visible. The destructive simulation time starts at 100.6ms because the first 100ms are used for the setting process simulation.

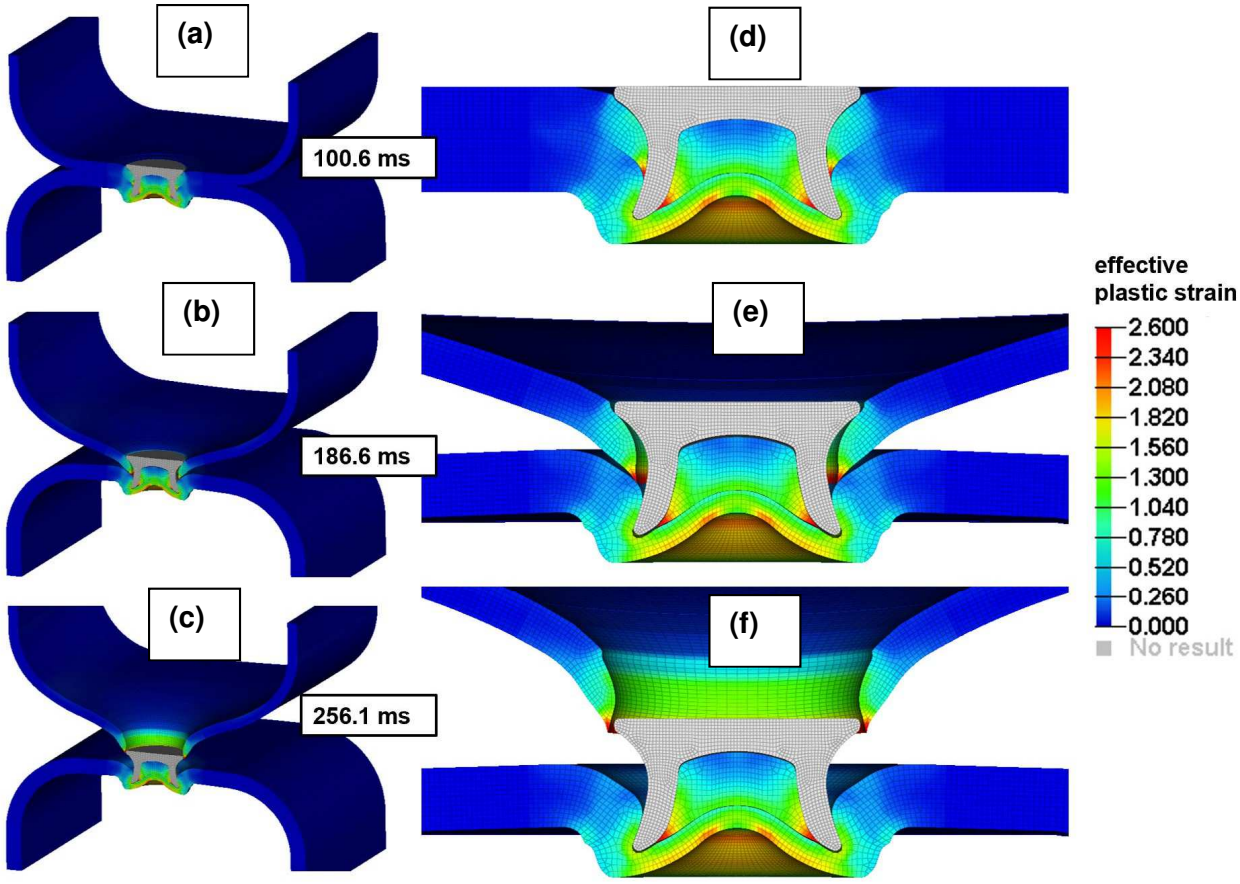

Figure 59 Plastic strain field of the 3D axial tension simulation

In Figure 60, the stress field of the destructive axial tension simulation is illustrated. It starts again with 100.6ms. Also, in this picture, the left column shows the overall perspective: (a), (b), and (c). The right column gives a closer look of the front view: (d), (e), (f). The simulation ends after 256.1ms. At the beginning, the 2D stress was mapped onto the 3D elements (a) and (d). The highest stress occurs at around 186.6ms in the lower aluminium sheet near the tip of the rivet. This is obviously because of the horizontal interlock. In this area, the pulling force is distributed over the upper sheet into the rivet and through the contact area into the lower sheet. The rivet is drawn through the upper sheet, and the lower sheet holds the rivet back. At the end (around 256ms), the stress decreases because of the failure of the joint and the elastic relaxation, which is visible in (f).

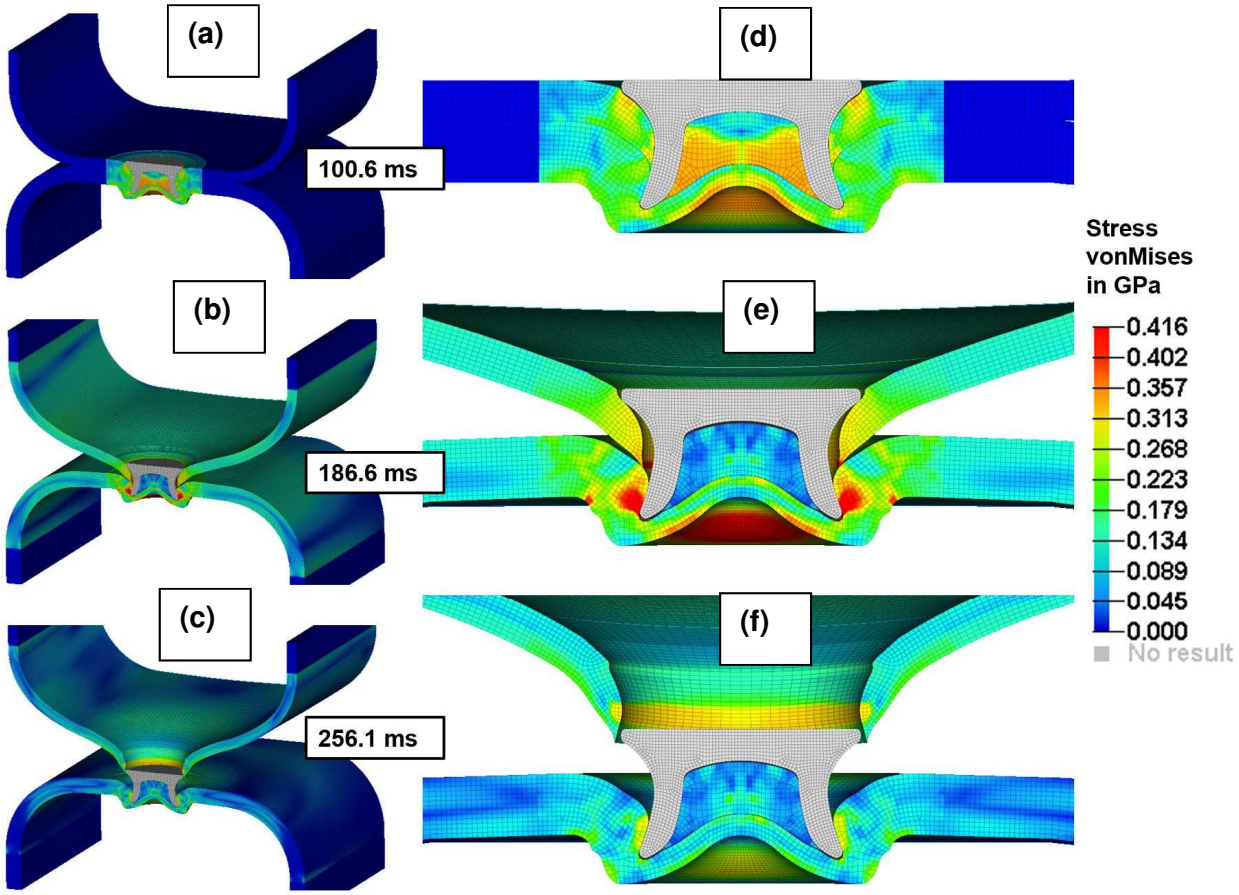

Figure 60 Stress field of the 3D axial tension simulation

Analysis of the force-displacement curve

The force-displacement curve, which is shown in Figure 61, illustrates a slight deviation between the experiment (data from [6]) and the numerical simulation. The force in the experiment (red curve) is, on average, 200N higher than in the simulation (green curve). The shape of the curve is fine, but there is a difference in the maximum peak of around 250N. In general, the accordance of the Force-displacement curve is quite good.

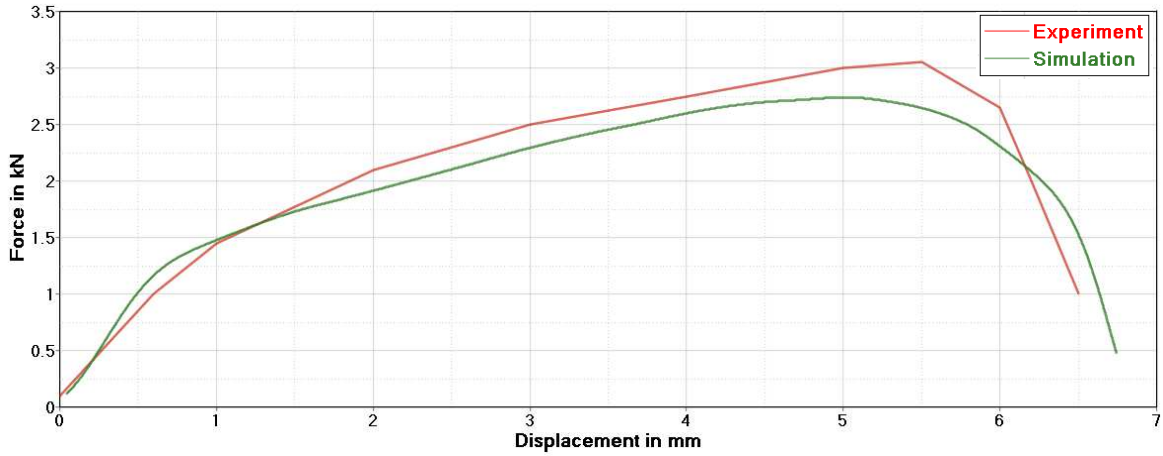

Figure 61 Force-displacement curve for axial tension simulation

5.6.2 Shear tension simulation

Shear tension model

For the shear tension test, a 3D model was needed as well, and the steps for this were similar to those for the axial tension test. The difference of modelling the KS2 sample and the axial tension test is the symmetry plane of the model. In the shear tension test, the x-z plane is used as a symmetry plane.

The steps for the 3D shear tension test are:

- creation of a 3D model from a 2D simulation result
- integration of the 3D model (KS2 sample)
- mapping of the effective strain and stress to the model as initial values

Figure 62 illustrates the numerical model for the shear tension test.

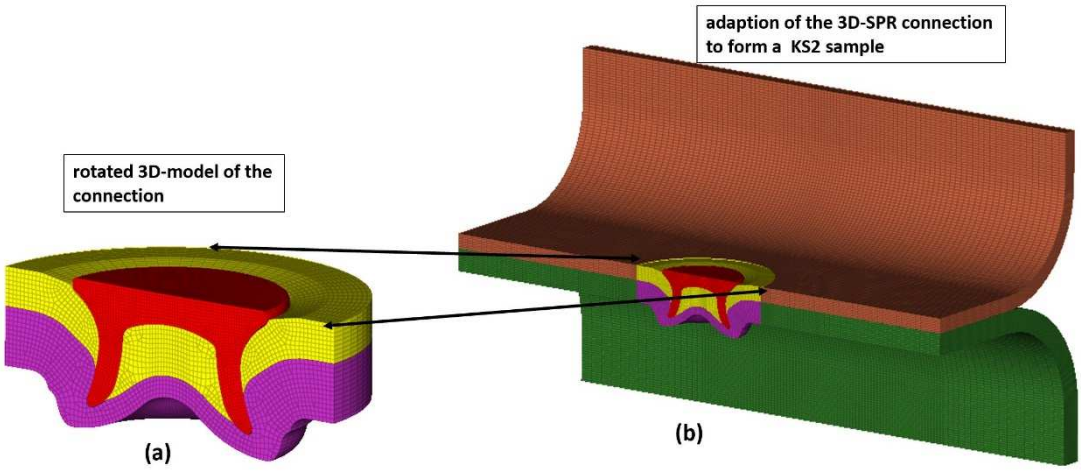

Figure 62 Model of 3D shear tension test overview

Boundary conditions for the shear tension test

Figure 63 illustrates the boundary conditions for the simulation. For the shear movement of the KS2 sample, the **BOUNDARY_PRESCRIBED_MOTION_SET* was used. As shown in Figure 63, the keyword is applied to the nodes in the red encircled area only. The upper nodes were moving in negative y-direction, and the lower nodes were moving in positive y-direction. A relative movement of 50mm/s was created. The load to the SPR joint was introduced over the legs of the KS2 sample. The relative movement of the upper and lower parts of the KS2 sample was about 10mm.

The symmetry plane (z-y) was defined in the centre of the model, and so only half a model had to be created. The keyword used was **BOUNDARY_SPC_SYMMETRY_PLANE_SET.*

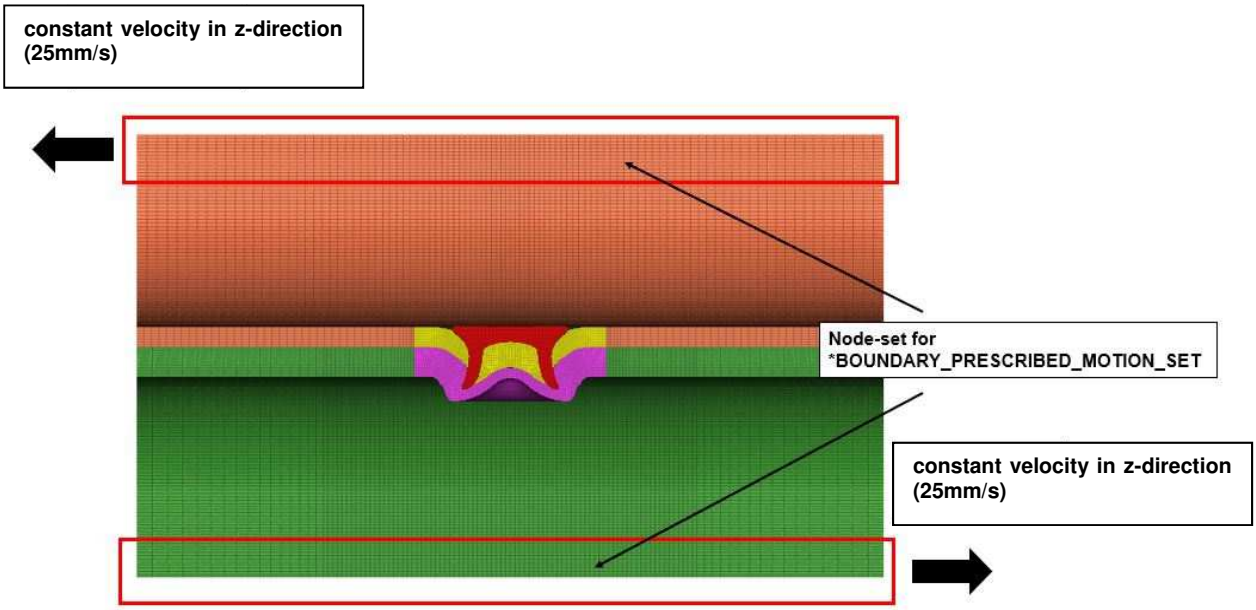

Figure 63 Boundary conditions for shear tension test

Mapping of the initial stress and effective strain field

Again, the stress and effective strain field from the 2D result was mapped onto the rotated 3D model and used as an initial value, illustrated in Figure 65.

Result of the shear tension simulation

Comparison of the deformation

In Figure 64, the deformation of the shear tension simulation is shown and compared to the experiment. In (a), the deformation of the destroyed sample is illustrated. Here, the upper and the disconnected lower parts of the KS2 sample are shown. The failure of the shear tension test is completely different to that of the axial tension test. The rivet was levered out by the induced force

and was pulled completely out of the top and lower sheet. During the test, the rivet head can also cause some additional damage to the lower aluminium sheet, which is marked in the picture (red encircled area) [6]. This additional damage is also slightly visible in the numerical simulation. The damage of the upper sheet is very similar to the simulation, which is marked in the green and yellow encircled area of the picture.

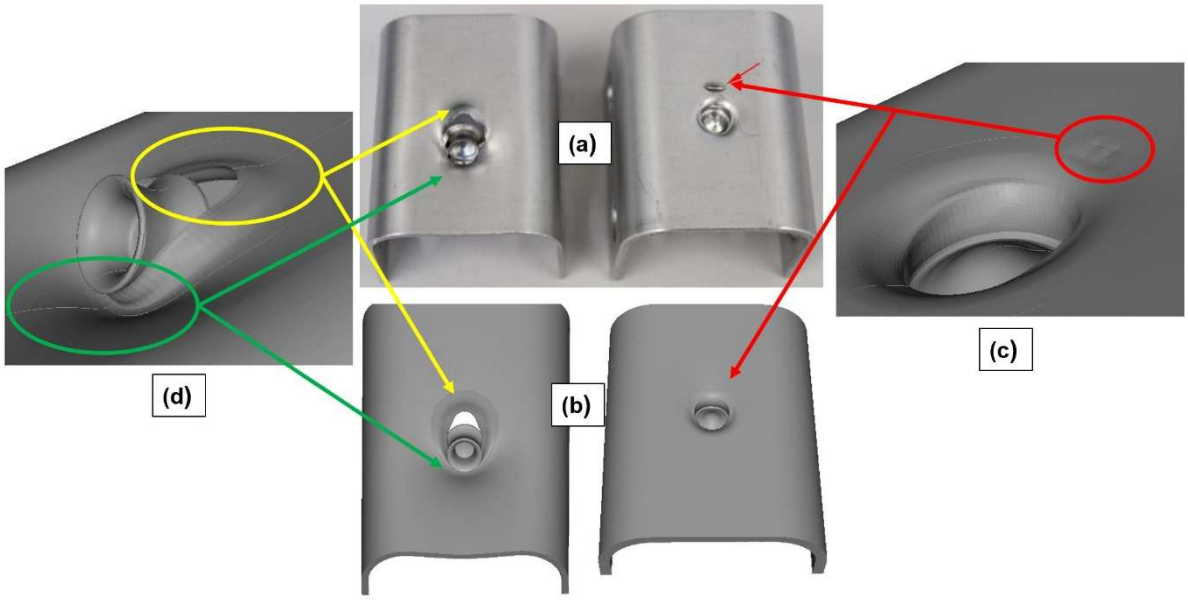

Figure 64 Comparison of the deformation in (a) experiment [6], (b) simulation, (c) detail lower sheet, (d) detail upper sheet

Analysis of effective plastic strain and stress (von Mises)

Figure 65 shows the effective plastic strain of the shear tension simulation. At 100.6ms, the initial status of the strain is visible. The left side of the picture shows an overview and on the right side, a closer look at the joint is illustrated. The initial status is defined by the input data from the 2D setting process. At 186.6ms, the levering out of the rivet is visualised. Here, the upper sheet is pushing against the rivet, which rotates. The right leg of the rivet is pulled out of the lower aluminium sheet. The upper sheet shows high deformation near the rivet head (left side). The rivet head comes in contact with the lower sheet, and causes additional damage. The average strain is about 1.8, and the maximum is 2.6. At the simulation time of 256.1ms, the rivet is pulled completely out of the lower sheet.

Figure 66 shows the stress (von Mises) of the parts during the simulation. Representatively, the times of 100.6ms, 186.6ms, and 256.1ms are analysed. At the beginning of the simulation, the stress field mapped from the result of the 2D setting simulation is shown. In general, the stress is in the area of 416MPa at the bulge of the lower aluminium sheet. A small area in the upper sheet also has such high stress, which could lead to failure or cracking. The rest of the parts show stresses between 200MPa and 300MPa.

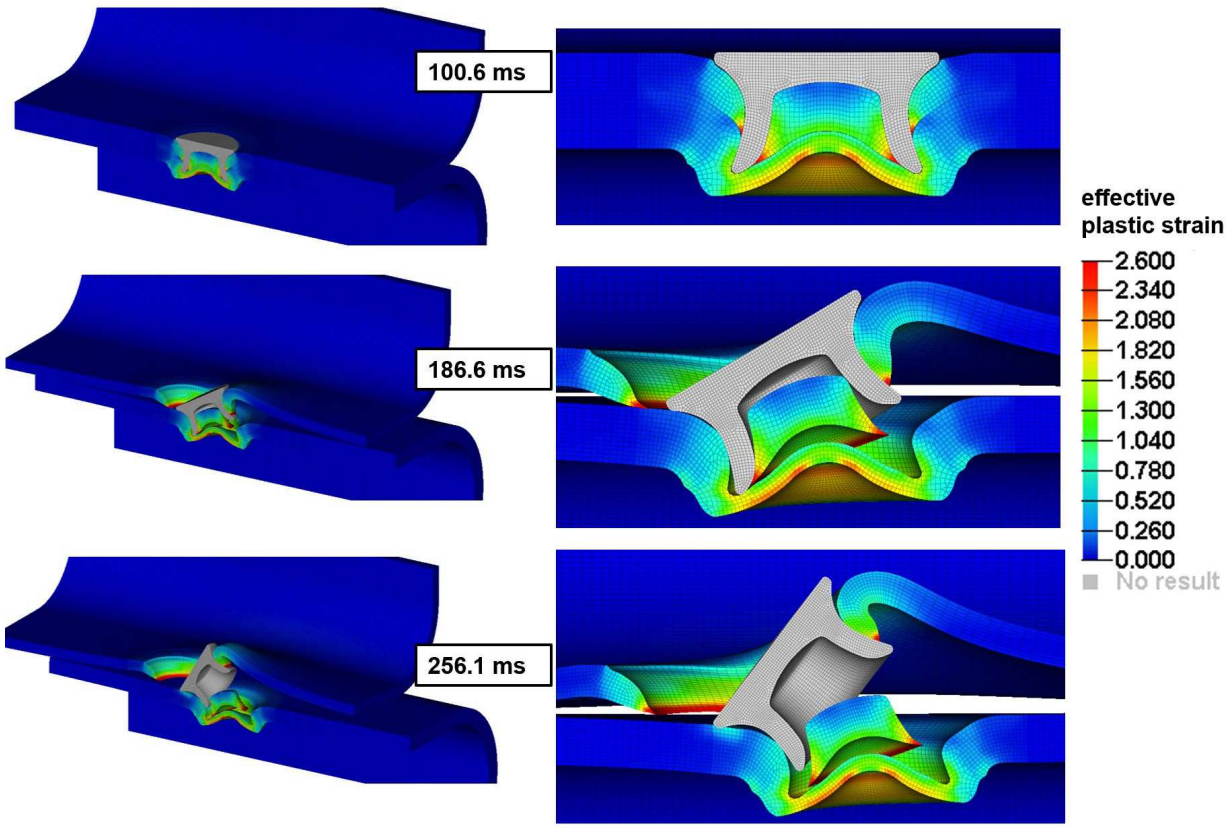

Figure 65 Effective plastic strain field of the shear tension simulation

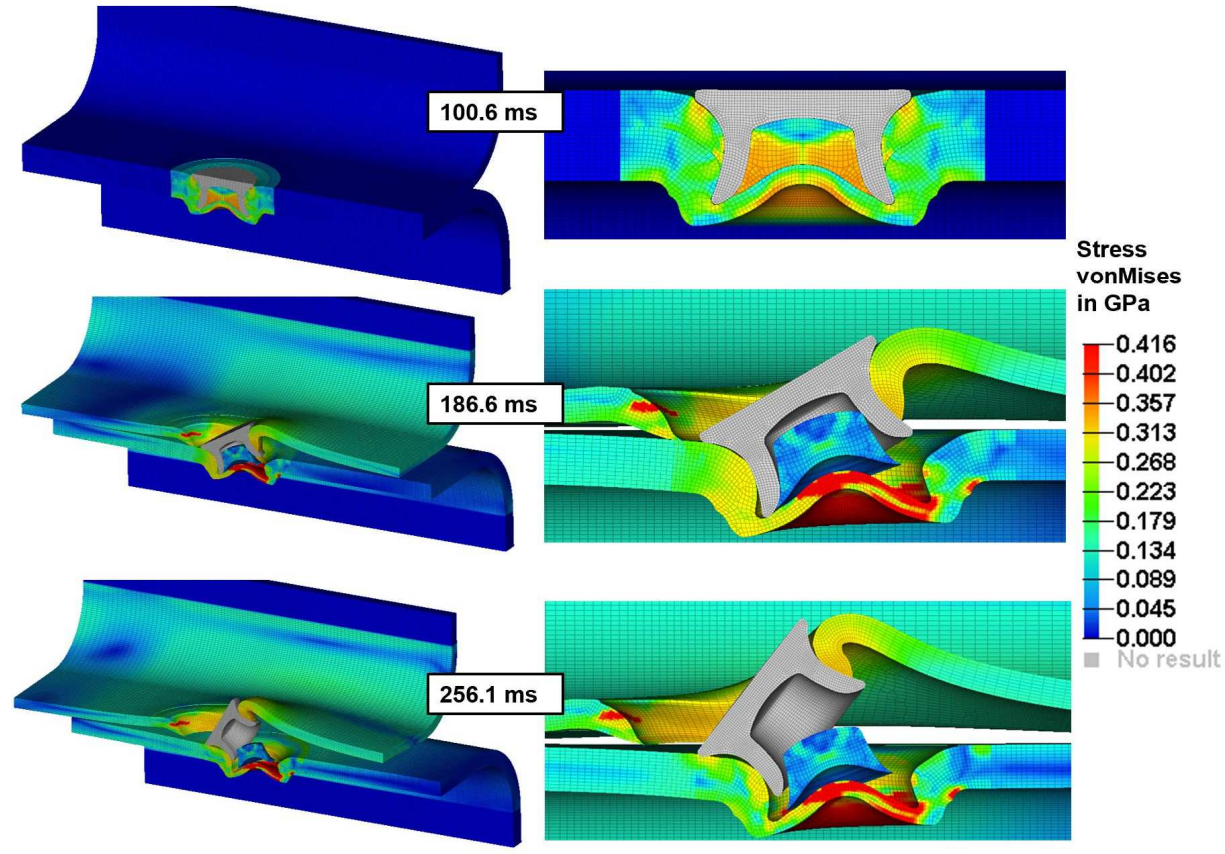

Figure 66 Stress field of the shear tension simulation

Analysis of the force-displacement curve

The next figure shows the comparison of the force-displacement curve from the simulation (green curve) with the experiment (data from [6], red curve). The shape of the curves is similar regarding the maximum force occurring in the first section; after that, the curves decrease to a lower value. The maximum force reached in the experiment occures at approximately 1.6mm with a value of 4.2kN. This is about 0.4kN higher than in the simulation (3.8kN), where the maximum force occurs at 2.4mm. Between 3mm and the end, the curves are quite different to each other with an average force variance of about 0.8kN.

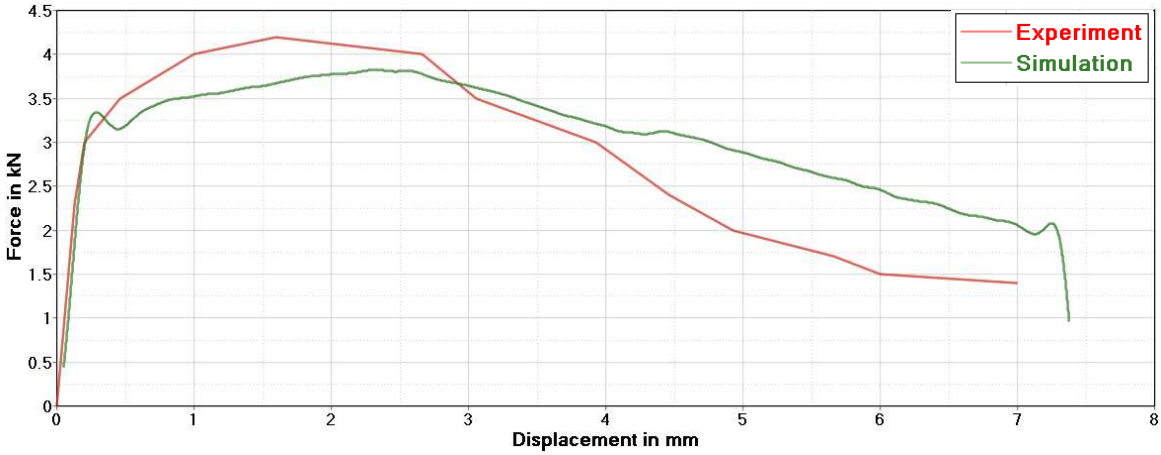

Figure 67 Force-displacement curve for the shear tension simulation

Conclusion of the destructive simulation

Using the presented approach (2D setting process, rotating 3D model), it is possible to get a good agreement of the experiment and the simulation. The main disadvantage of such an approach is that misalignments which can occur during the setting process cannot be captured. To deal with this, a 3D numerical model is needed, which is described in the next chapter.

6 THREE-DIMENSIONAL SELF-PIERCING RIVETING PROCESS

In this chapter, the 3D numerical self-piercing riveting process is investigated. The reason for performing time-consuming 3D simulation are misalignments which can occur during the setting process.

These misalignments are:

- misalignment between the rivet axis and the tool axis
  The main reasons for this are the tolerances of the components of the assembly and changes during the production, for example, temperature fluctuations, abrasion of the parts, etc.

- tilting of the die during setting process
  The main part of the system is the C-frame with the rivet gun. Because of the process forces, up to 50kN, the frame deforms elastically, and therefore a tilting of the die is possible. This tilting affects the correct position of the rivet and the mechanical strength of the rivet joint.

Those problems which can occur during production cannot be investigated with a 2D numerical simulation model. For that reason, in this thesis, a 3D model was developed and validated.

6.1 3D EFG model

The first approach to create a 3D numerical model was applying the element-free Galerkin *(EFG)* meshless method. The EFG method can handle large deformations better than conventional FEM. Therefore, the numerical accuracy and stability are much better at high deformations. The EFG method is very often used in forming simulations. However, it has the same problems as the conventional FEM with respect to extremely high deformations and also material failure. The EFG method cannot handle failure during the simulation, but the simulation can be stopped during the setting process, and the elements can be deleted manually. After the deleting process, the numerical simulation can continue. The EFG meshfree method can manage adaptivity (remeshing), which is useful for forming simulations.

Advantages of the meshfree EFG method [40]:

- large deformations are possible
- adaptivity can be used

Disadvantages of the meshfree EFG method [40]:

- high CPU cost
- complicated in parallel (mpp, to split the simulation on various PCs in a network [43])

6.1.1 Mesh of the EFG-model

The 3D model consists of the following components, which are illustrated in Figure 68:

- punch (rigid)
- SPR (deformable)
- upper and lower aluminium sheets (deformable)
- die (rigid)
- blank holder (rigid)

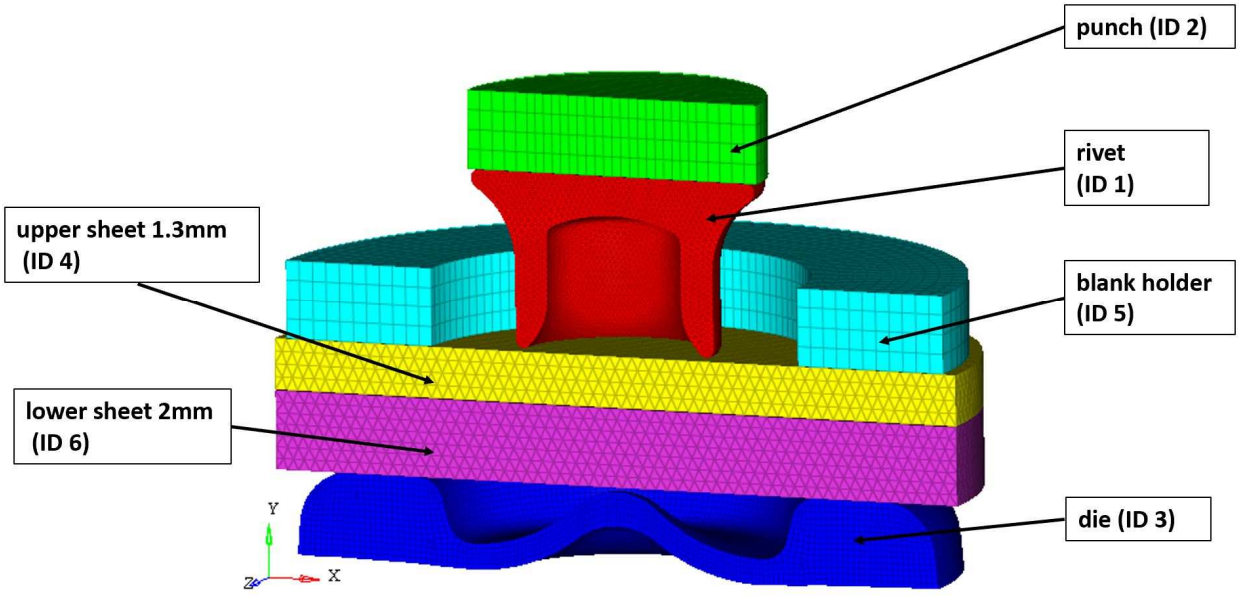

Figure 68 3D EFG model of the setting process

The numerical 3D model is only half a model with symmetrical boundary conditions to reduce the simulation time. The option **BOUNDARY_SPC_SYMMETRY_PLANE* was implemented into the model. The symmetrical model enables the investigation of the misalignment of the rivet and tilting of the die.

3D elements

In the 3D numerical model, tetrahedron and hexahedral elements were used. The rigid parts like die, punch, and blank holder consisted of hexahedral elements, and the deformable parts were meshed with tetrahedrons.

Aluminium alloy sheets

The upper aluminium sheet has a thickness of about 1.3mm and the lower aluminium sheet of 2.0mm. The size of the elements for the 3D sheets is 0.2mm. The simulation adaptivity steps (remeshing steps) for the mesh were integrated with the option **CONTROL_ADAPTIVE*. With this, the element size in the area of the large deformation changed to 0.1mm. This adaption is shown in Figure 69.

Adaption of the mesh

Because of the large deformations occurring during the setting process, which can lead to a high element distortion and termination of the simulation, an r-adaptive remeshing was integrated whereby a completely new mesh is generated. For 3D models, tetrahedral elements were created, and therefore the sheets were, by default, modelled with tetrahedral elements.

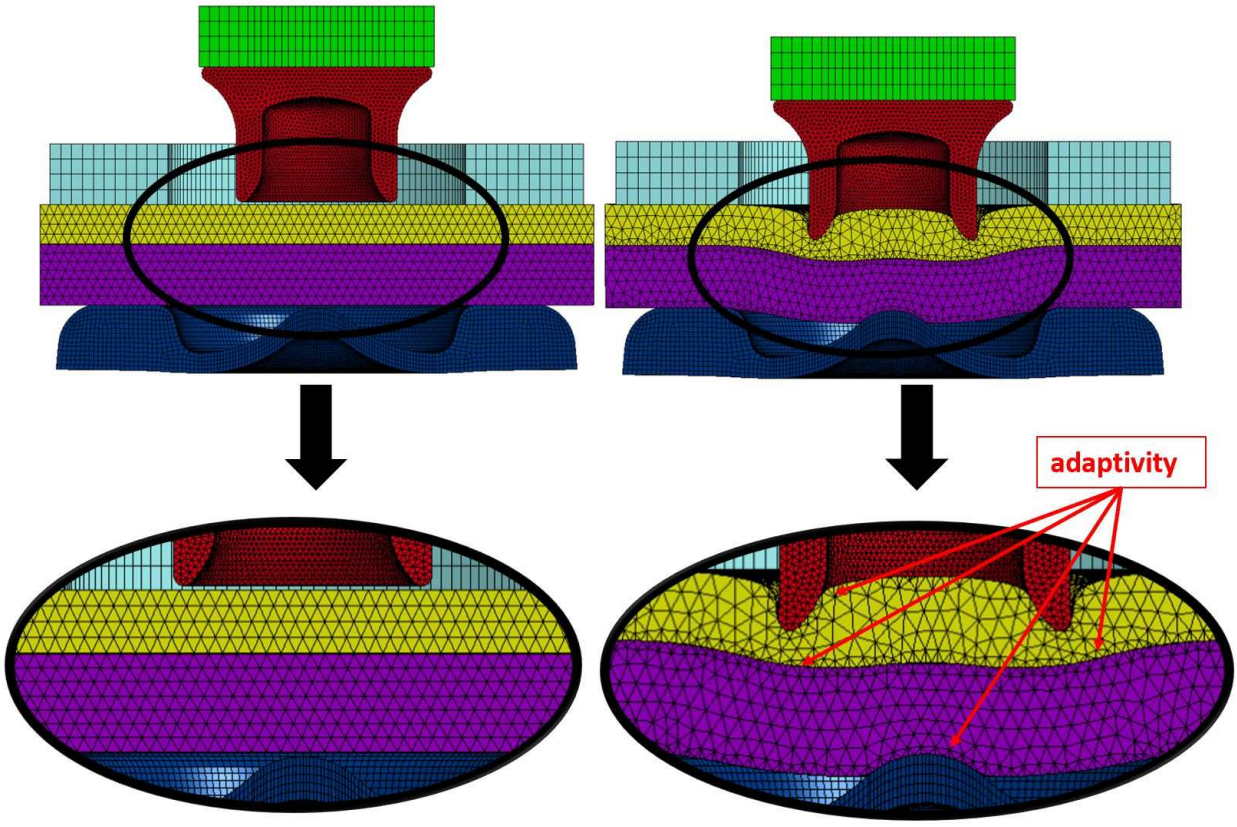

Figure 69 Adaptivity of 3D EFG-model: initial status (left) and during processing (right)

Rivet

The complex geometry of the rivet can be meshed very easily with tetrahedrons. The element size used is 0.1mm. The rivet could also be meshed with hexahedral elements, but some problems appeared during rotation of the element near the rotation axis. The elements near the

axis are very small, which influences the simulation in a negative way. Therefore, tetrahedral elements are used. The meshed rivet is illustrated in Figure 70.

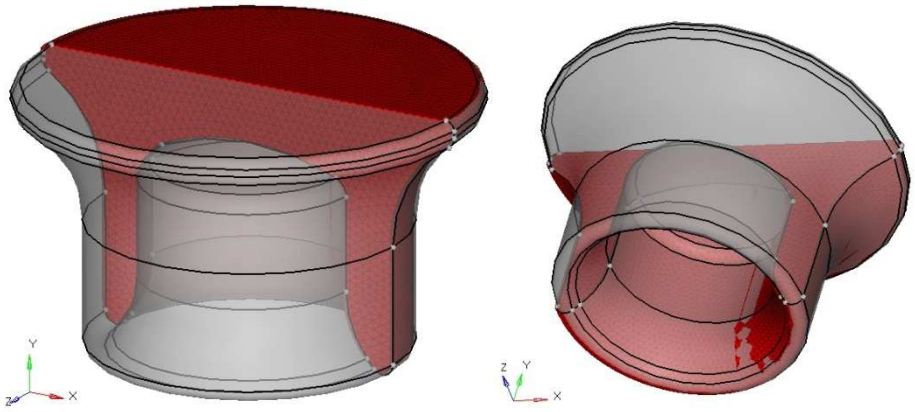

Figure 70 3D mesh of SPR

Rigid parts

The rigid parts like the die, punch, and blank holder were meshed with hexahedral elements. In Figure 71, the meshed parts and the element sizes are shown. The size of the element is slightly larger than the parts which can deform.

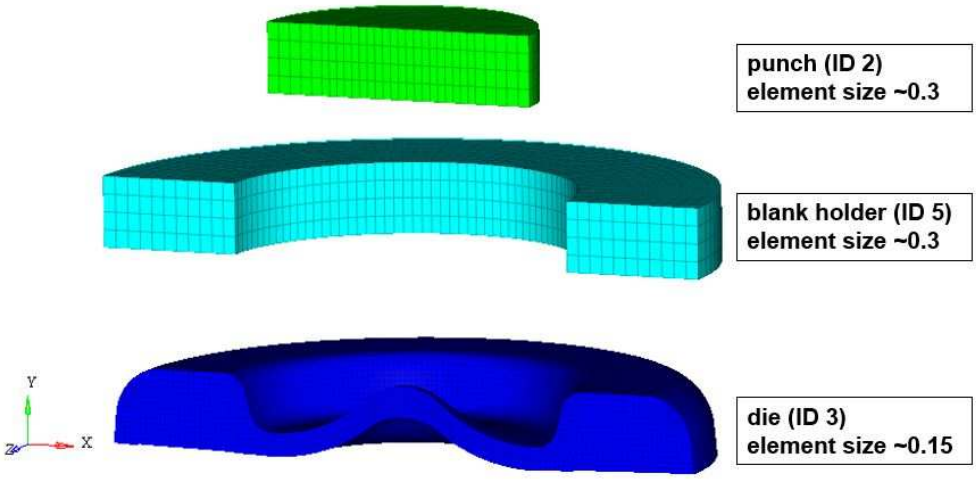

Figure 71 3D mesh rigid parts (EFG method)

A short summary of the elements used in the 3D EFG simulation is illustrated in Table 5.

Table 5 3D EFG element formulation summary

ID	Part	Element-formulation	Element-size	Adaptivity
1	*rivet*	*tetrahedral*	*~0.1*	*No*
2	*punch*	*hexahedral*	*~0.3*	*No*
3	*die*	*hexahedral*	*~0.15*	*No*
4	*upper sheet*	*tetrahedral*	*~0.2*	*yes (~0.1)*
5	*blank holder*	*hexahedral*	*~0.3*	*No*
6	*lower sheet*	*tetrahedral*	*~0.2*	*yes (~0.1)*

6.1.2 Contact definition

For the EFG-simulation, a **CONTACT_AUTOMATIC_SURFACE_TO_SURFACE* definition was used. This contact type is a two-way treatment of the contact pairs, as described in section 4.3.1. Static and dynamic friction was implemented in the contact card. In Table 6, the contact definition of the model is summarised.

Table 6 Contact between parts for 3D EFG-model

ID	Parts in Contact	Static Friction (FS)	Dynamic Friction (FD)
1	***Rivet (ID 1) <--> Upper Sheet (ID 4)***	***0.12***	***0.12***
2	***Rivet (ID 1) <--> Lower Sheet (ID 6)***	***0.12***	***0.12***
3	***Blank Holder (ID 5) <--> Upper Sheet (ID 4)***	***0.2***	***0.2***
4	***Plunger (ID 2) <--> Rivet (ID 1)***	***0.2***	***0.2***
5	***Upper Sheet (ID 4) <--> Lower Sheet (ID 6)***	***0.12***	***0.12***
6	***Die (ID 3) <--> Lower Sheet (ID 6)***	***0.2***	***0.2***

6.1.3 Material data

For the deformable parts (steel rivet, upper/lower aluminium alloy sheets), the material model **MAT_PIECEWISE_LINEAR_PLASTICITY* was used. The material used for the aluminium sheets and steel rivet are described in section 4.3.2 . For the tools (blank holder, punch, die), the material model **MAT_RIGID* was applied. The defined materials for the different parts are summarised in Table 3, section 5.3.

The material data was implemented in the parts definition. In that card, the element formulation and section formulation were also integrated. Figure 72 illustrates a part card and section card of the 3D EFG model. Representatively, the part card of the lower aluminium sheet is described. In it, the option for r-adaptive can be activated by writing the number '2' into the column of '*adpopt*'. In the section card DX, DY, and DZ stand for the influence area of the particle or interaction area of the particles.

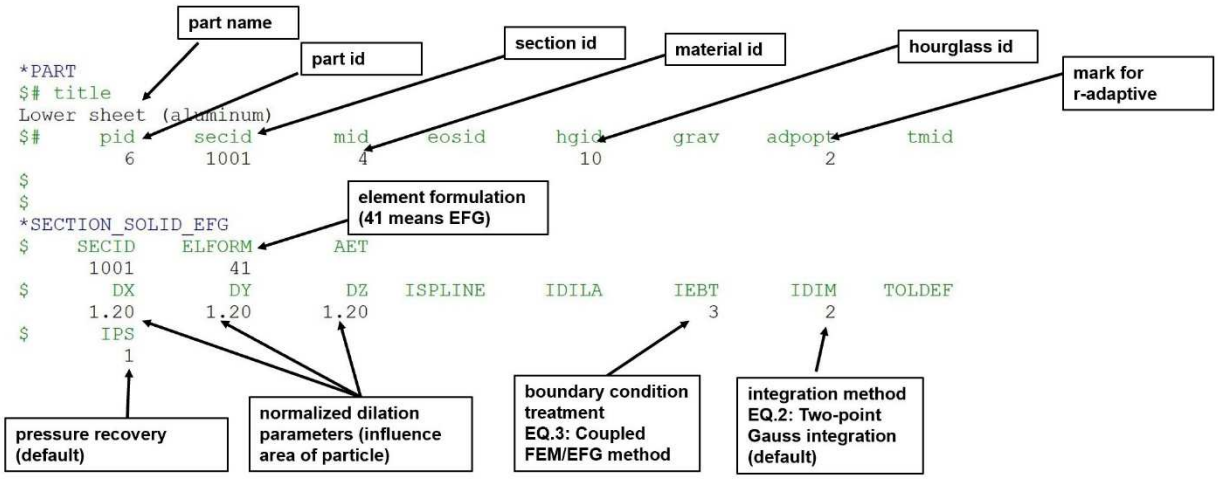

Figure 72 Part and section card for 3D EFG simulation

6.1.4 Boundary conditions and load

The boundary conditions used for the 3D simulation are the same as for the 2D model. For the movement of the punch, the **BOUNDARY_PRESCRIBED_MOTION_RIGID* keyword is used, and for the blank holder force (10kN), the **LOAD_RIGID_BODY* option was implemented. To hold the die in place, the degrees of freedom in all directions are locked in the **MAT_RIGID* card. The *LOAD_BODY_Y* was used for gravity. The characteristics of the different boundary conditions and load options are described in section 5.4.

Stopping the simulation during processing

The EFG method cannot handle failure during the simulation. It is possible to bypass this problem by stopping the simulation during the setting process and deleting some elements. This happens close to the cutting of the upper sheet when the thickness of the part has a size of about 0.1mm (manual failure of the elements). After deleting the elements, the remesh takes place, and the numerical simulation can continue. Deleting the elements was done using Altair HyperMesh. The upper sheet before and after the deleting process is visualised in Figure 73. For the second part of the simulation, the r-adaptivity was deactivated.

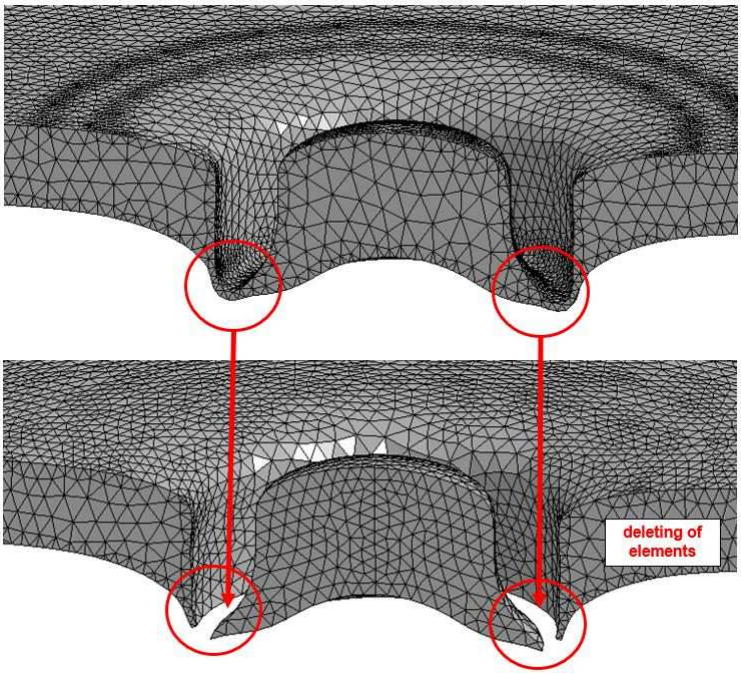

Figure 73 EFG model: deleting of elements during the simulation

6.1.5 Results of the 3D EFG-model

Force-displacement curve

In the 3D EFG simulation, the stiffness of the C-frame (SPR tool) was neglected, and an ideal model was used (rigid die). Figure 74 illustrates the force-displacement curve of the 3D EFG model (green curve) compared to the curve from the 2D setting process (red curve), which has a good correlation with the experiment, as described in section 5.5.2. In the Figure 74, the 3D curve shows high vibration. The reason for that is the r-adaptivity which takes place every 0.05ms and creates a new mesh. In the first part of the curve (until 2.5mm), a moderate deviation is occurring compared to the 2D result. At the cutting point of the upper sheet, the force is much higher than at the 2D result (5kN), and also the shape of the curve is like a constant slope, which is not exactly the same as in the 2D result.

At 2.5mm displacement of the rivet, the simulation stops, and the manual deleting process takes place as described before. This is also illustrated in Figure 74. After restarting the simulation, the curve drops down to 17.5kN. Because of deleting and remeshing, there is a distorted shape of the curve until 2.75mm. From 2.75mm to the end of the simulation, the shape of the curve is quite similar to the 2D result and, at 4.5mm, reaches a maximum of 53kN compared to 55kN for the 2D simulation.

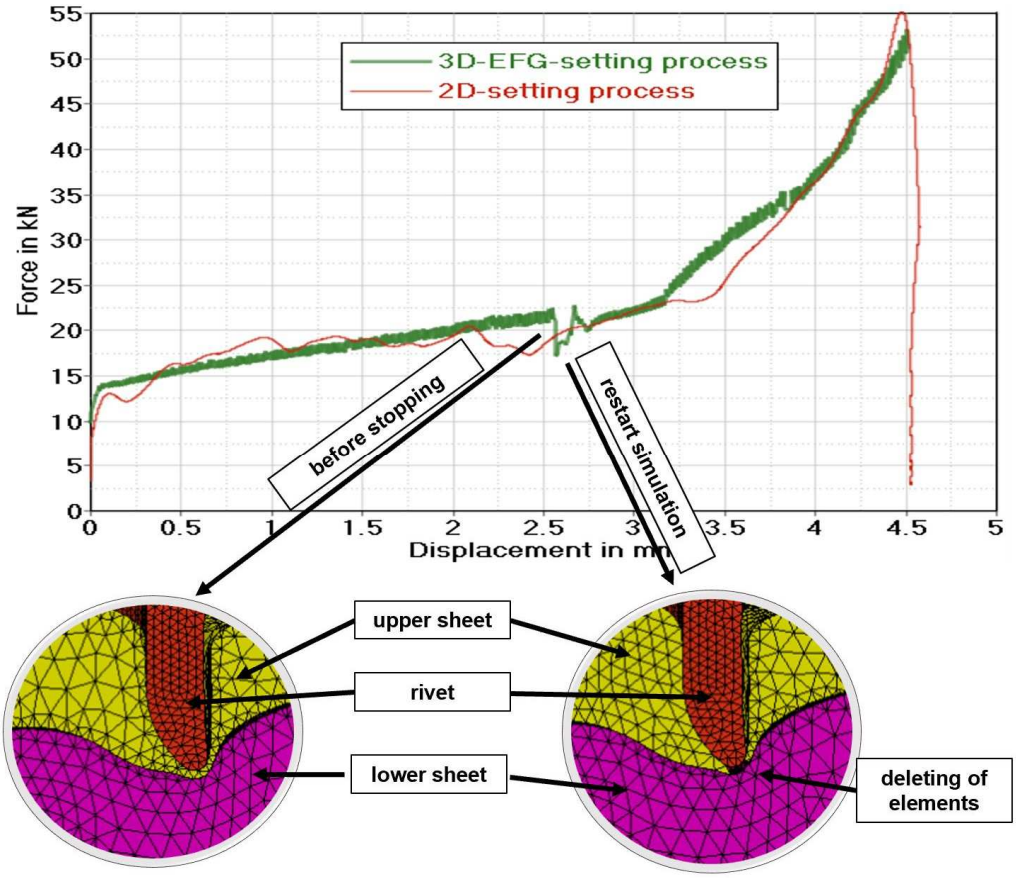

Figure 74 Force-displacement curve of 3D EFG simulation

Comparison of 3D EFG simulation versus reality

Figure 75 illustrates (a) the microsection of the SPR (experiment) with the main geometrical features and (b) the result of the 3D EFG simulation. The horizontal interlock in the simulation is 0.35mm versus 0.31mm in the experiment, which is quite a good correlation. The residual thickness in the simulation is about 0.61mm, moderately higher than in the experiment with 0.56mm. The rivet head position in the simulation is 0.0mm versus 0.24mm in the experiment.

The overall deformation observed in the simulation also has a good accordance with the experiment. The degree of filling of the die is higher than in the experiment. This can be seen by the encircled red area.

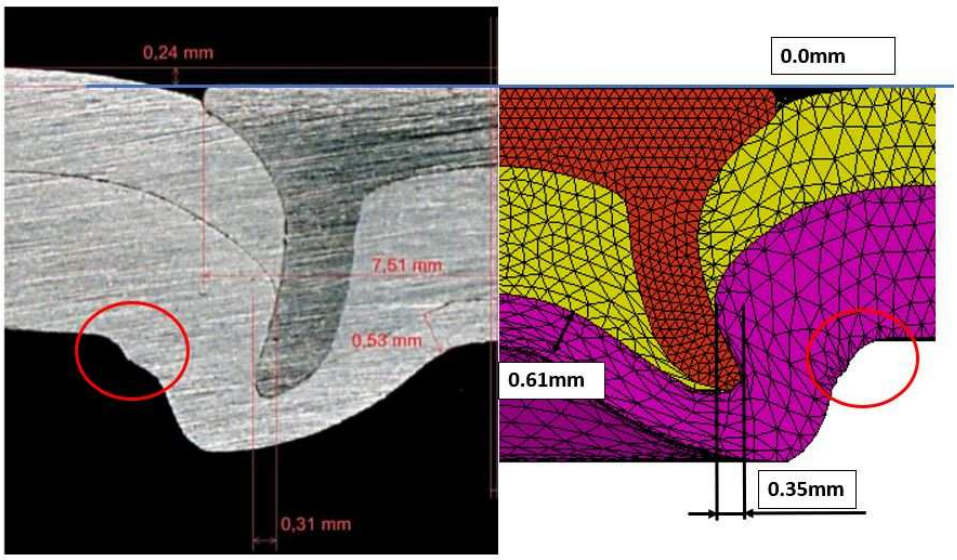

(a) *(b)*

Figure 75 Comparison of the deformation between experiment (a) and 3D EFG simulation (b)

Result of the effective strain field

Figure 76 illustrates the effective plastic strain field at the end of the SPR setting process. The highest plastic strain occurs in the area where the upper sheet touches the rivet. Furthermore, in the area where the lower sheet touches the die, a higher plastic strain occurs because of the deformation due to the rivet spreading.

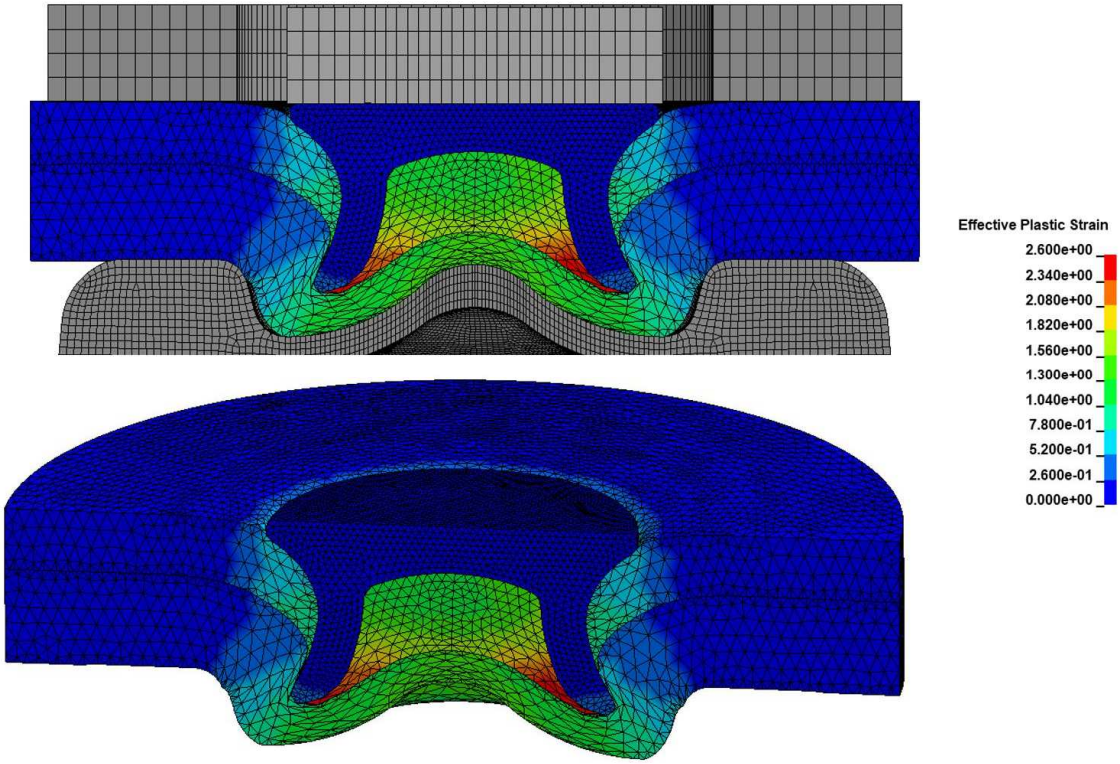

Figure 76 3D EFG effective plastic strain field at the end of the setting process

6.1.6 Discussion of the EFG simulation result

The main disadvantage of the EFG method is the stopping of the simulation to cut through the upper sheet. This manual step brings some inaccuracies into the simulation. Because the cutting area is picked by the user, the real cutting area can occur in a different sector, which leads to a false result. Furthermore, the correct time when the cutting occurs must be detected. To find the correct stopping time, a simulation must be done without stopping. With this first simulation, the time and the area of the deleting can be identified and implemented in the second simulation with the cutting process.

To eliminate this disadvantage, a second 3D setting model was implemented using the smoothed particle Galerkin (SPG) method [31, sections 36–73]. This method is described in the next subchapter.

6.2 3D SPG model

In the last several years, the SPG was developed as a new meshless method, which means there is no connection required between the nodes. Such approaches are primarily used in fluid simulations but are now also used for investigations of structural parts for process simulations. This method can handle large deformations and has a higher numerical stability. However, there are also some disadvantage regarding the meshfree method such as tension instabilities [42]. These drawbacks are suppressed or stabilised by using a special smoothing scheme in the displacement field [41]. There is no remeshing necessary, and therefore a remapping of stress or strain is not necessary. In that way, better accuracy can be achieved. Furthermore, a constant Eulerian kernel was implemented to capture the large deformation and reduce the tension instabilities [42].

One important feature in the numerical simulation is the handling of failure. LsDyna has a large library of materials and failure models. The SPG method supports those failure models, and nodes can, for example, be eroded (*MAT_ADD_EROSION). LsDyna developed a bond-based failure criterion for the SPG method. For this criterion, the effective plastic strain between the nodes in the support area is calculated and compared to the user definition. If the value of the calculated effective plastic strain reaches predefined value, the surrounding nodes or particles are disconnected. The principle of this failure model is shown in Figure 77. Particle one (red) and particle two (blue) are connected via the black dashed line. If the strain reaches the input value, this connection is deleted, and particle one has no influence on particle two anymore and vice versa. The red and blue circles are the supported areas of the particles [42].

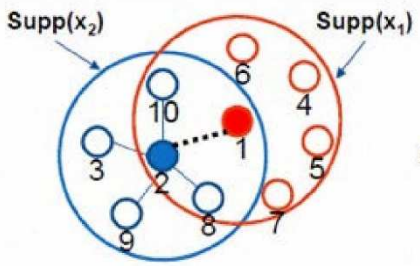

$$\varepsilon_{12}^{p} = \frac{\varepsilon_{eff}^{p}(X_1) + \varepsilon_{eff}^{p}(X_2)}{2}$$

Figure 77 SPG bond failure [42]

With this method, process simulations are much more stable and more accurate than the conventional approaches with the FEM.

6.2.1 Basic SPG model

To reduce the numerical simulation time, a hybrid SPG-FEM model was created. The 3D basic SPG model consists of the following components, illustrated in Figure 78:

- punch (rigid)
- SPR (deformable)
- upper and lower aluminium sheets (deformable)
- die (rigid)
- blank holder (rigid)
- SPG area of the upper aluminium sheet (deformable)
- SPG area of the lower aluminium sheet (deformable)

To reduce the computational effort, a half hybrid SPG-FEM model with symmetrical boundary conditions was used. This model is sufficient for the investigation of misalignment and tilting.

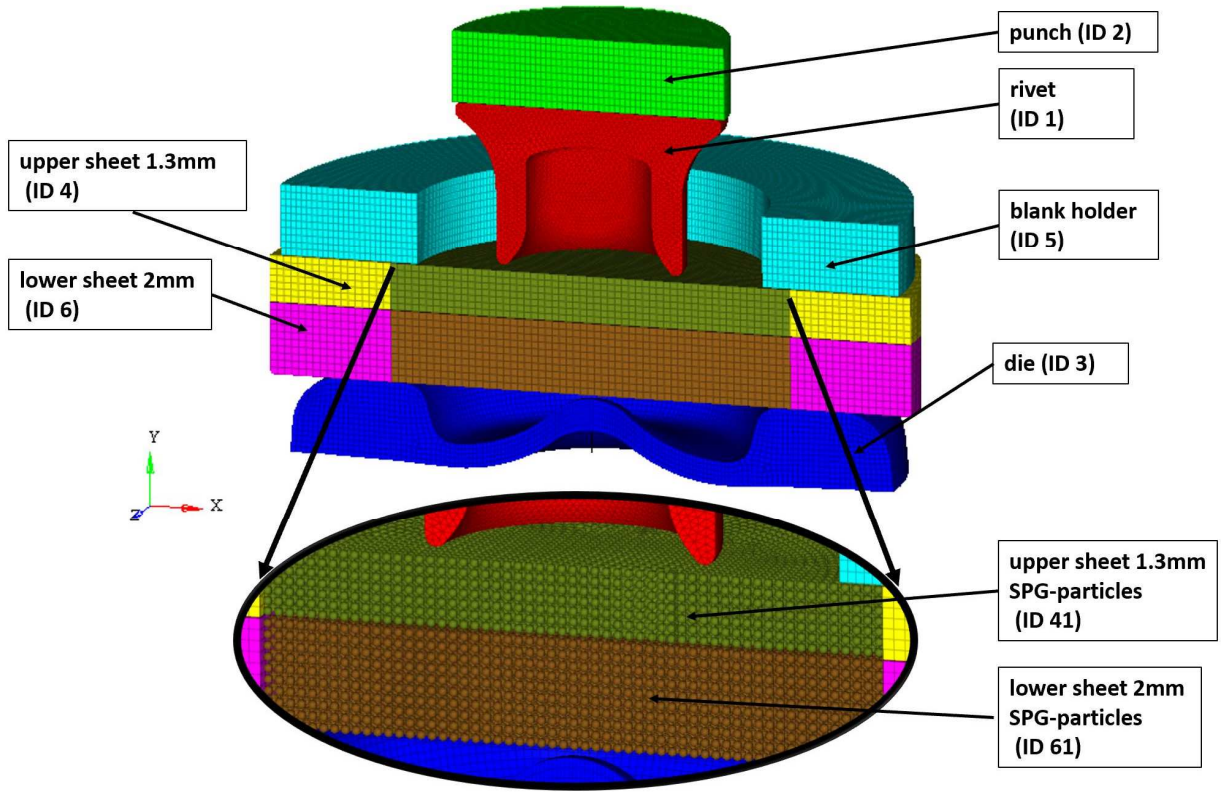

Figure 78 The 3D hybrid basic SPG model

The upper and lower aluminium sheets were divided into two parts. The zones where the large deformations and failure occur are modelled with SPG particles. The normalised nodal support size for the SPG particles was set to 1.5, and the Eulerian kernel with T-bond failure algorithm was used. The exact definition is illustrated in Figure 79.

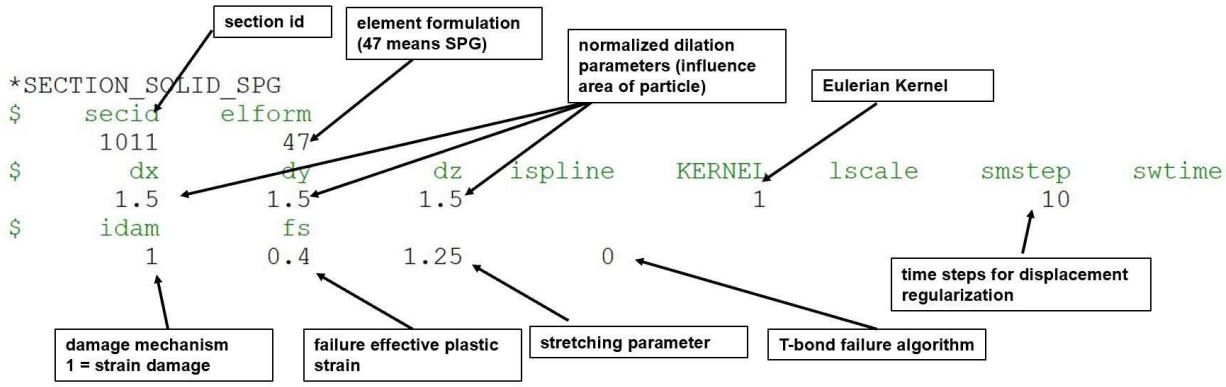

Figure 79 Section card of the SPG part

The rivet was modelled with tetrahedral elements and all other parts with hexahedral elements. The size of the elements is summarised in Table 7.

Table 7 Element size of the SPG model

ID	Part	Element formulation	Element size
1	*rivet*	*tetrahedral*	*~0.1*
2	*punch*	*hexahedral*	*~0.15*
3	*die*	*hexahedral*	*~0.15*
4	*upper sheet*	*tetrahedral*	*~0.2*
5	*blank holder*	*hexahedral*	*~0.15*
6	*lower sheet*	*tetrahedral*	*~0.2*
41	*upper sheet*	*SPG*	*~0.2*
61	*upper sheet*	*SPG*	*~0.2*

6.2.2 Contact definition

For the hybrid SPG-FEM simulation, the following contact definitions were used:

- ***CONTACT_AUTOMATIC_SURFACE_TO_SURFACE**

The two-way symmetrical contact definition was used for the contact of the upper and lower aluminium sheets (FEM elements). Static and dynamic friction was implemented in the contact card.

- ***CONTACT_NODES_TO_SURFACE**

This single-surface contact definition was used for parts in contact with the SPG particles. The particles are implemented in a node set and defined as slave contact side. The opponent contact part is defined as master contact side. Also, the deformable parts in contact with rigid parts are defined in that way. Again, static and dynamic friction is implemented in the contact card.

- ***CONTACT_TIED_NODES_TO_SURFACE**

In this contact definition, the slave nodes were constrained (fixed) to the master surface, so they were moving with the master contact. The punch is implemented as master contact and the rivet as slave contact.

The contact definition used is described in section 4.3.1 (‘Contact definition in LsDyna’).

Table 8 Contact definition of the hybrid SPG-FEM model

Parts in Contact			Static Friction (FS)	Dynamic Friction (FD)	Contact definition
Rivet (ID 1)	<-->	SPG Upper Sheet (ID 41)	0.12	0.12	NODES_TO_SURFACE
Rivet (ID 1)	<-->	SPG Lower Sheet (ID 61)	0.12	0.12	NODES_TO_SURFACE
Blank Holder (ID 5)	<-->	Upper Sheet (ID 4)	0.2	0.2	NODES_TO_SURFACE
Die (ID 3)	<-->	Lower Sheet (ID 6)	0.2	0.2	NODES_TO_SURFACE
Blank Holder (ID 5)	<-->	SPG Upper Sheet (ID 41)	0.2	0.2	NODES_TO_SURFACE
Die (ID 3)	<-->	SPG Lower Sheet (ID 61)	0.2	0.2	NODES_TO_SURFACE
Upper Sheet (ID 4)	<-->	Lower Sheet (ID 6)	0.12	0.12	SURFACE_TO_SURFACE
Plunger (ID 2)	<-->	Rivet (ID 1)	0.2	0.2	TIED_NODES_TO_SURFACE

6.2.3 Material data

The material data used for the hybrid SPG-FEM model are the same as for the EFG model (described in section 6.1.3). The material behaviour of the deformable parts is modelled with the *MAT_PIECEWISE_LINEAR_PLASTICITY and the behaviour of the tools with *MAT_RIGID material definition. The material definitions for the different parts are summarised in Table 3 (section 5.3).

6.2.4 Boundary condition and load

The boundary conditions are the same as in the 3D EFG model. For the moving of the punch, the **BOUNDARY_PRESCRIBED_MOTION_RIGID* keyword was used, and for the blank holder force (10kN), the **LOAD_RIGID_BODY* keyword was implemented. The characteristics of the different boundary and load conditions are described in section 5.4. The punch speed was defined as 92mm/s.

6.2.5 Results of the basic SPG model

The following section addresses the results of the basic SPG model. First, the deformation of the SPR (rivet) is evaluated and compared to the experiment. After that, the effective plastic strain and the stress (von Mises) are analysed. At the end of this section, the force-displacement curve of the 3D SPG setting process is compared to the curve from the experiment.

6.2.5.1 Optical investigation of the connection (basic SPG model)

Figure 80 shows the deformed rivet (red part) and the two aluminium sheets, which were jointed during the process. The aluminium sheets are separated into the FEM elements at the outer area and the SPG-particles in the centre of the model where the large deformations occur. The different views in Figure 80 show the main geometrical features of the joint. For the filling ratio, one characteristic feature is the geometry of the closing head (black encircled). This characteristic feature depends on the spreading of the rivet. The picture in the middle of Figure 80 shows the front view, and the lower picture shows an isometric view of the simulation result. Overall, the SPR joint looks quite satisfactory.

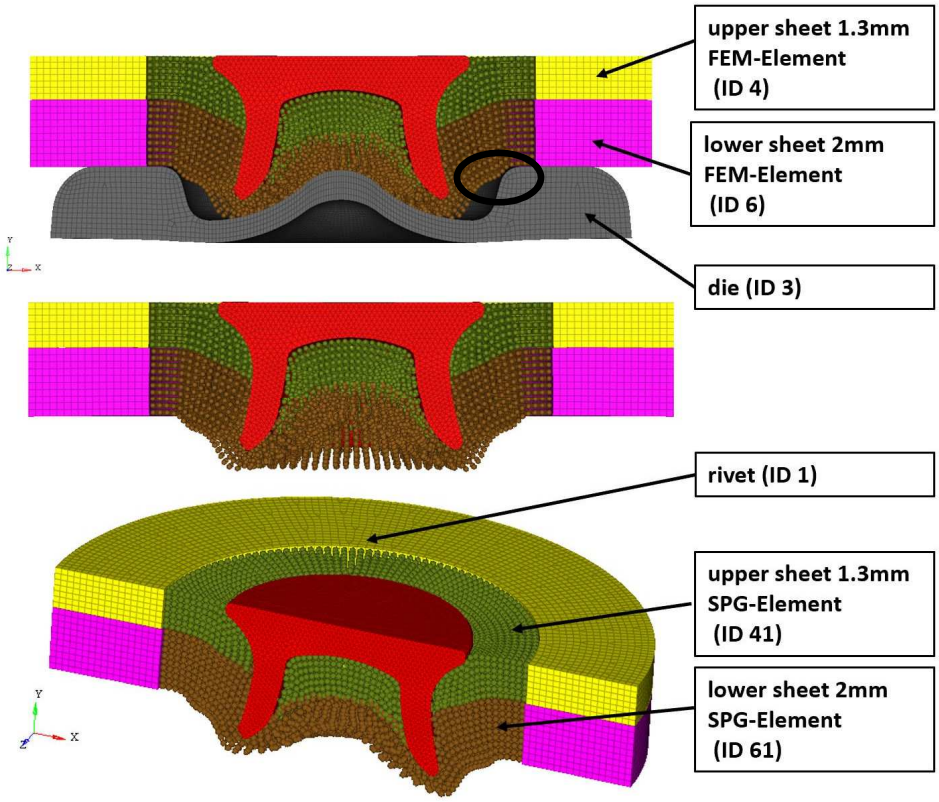

Figure 80 Result of deformation of the basic SPG model

Figure 81 illustrates the result of the numerical basic SPG simulation compared to the microsection of this SPR joint. In this figure, the horizontal interlock, closing head, and residual wall thickness of the joint are compared. In the numerical simulation, the horizontal interlock is 0.34mm, which is 0.03mm more than in the experiment. That means a difference of about 10 per cent, which is quite good. The numerical simulation also shows an increase of about 25 per cent in residual wall thickness compared with the experiment. This could lead back to the SPG model because of the small transition zone of the particles (black encircled) between the upper and lower sheets. The difference in the residual wall thickness can be reduced by optimising the final position of the rivet in the simulation. In the experiment, the rivet head is 0.24mm below the upper

edge of the upper aluminium. In the simulation, the head is nearly parallel with the upper edge of the sheet. By increasing the displacement of the rivet, the residual wall thickness can be reduced, but the spreading of the rivet leg would also increase, therefore diverging from the experiment. The feature of the closing head (red encircled) shows a quite strong accordance between the numerical simulation and the experiment. The 3D basic SPG model shows a high correlation of the deformation between the numerical simulation and the experiment.

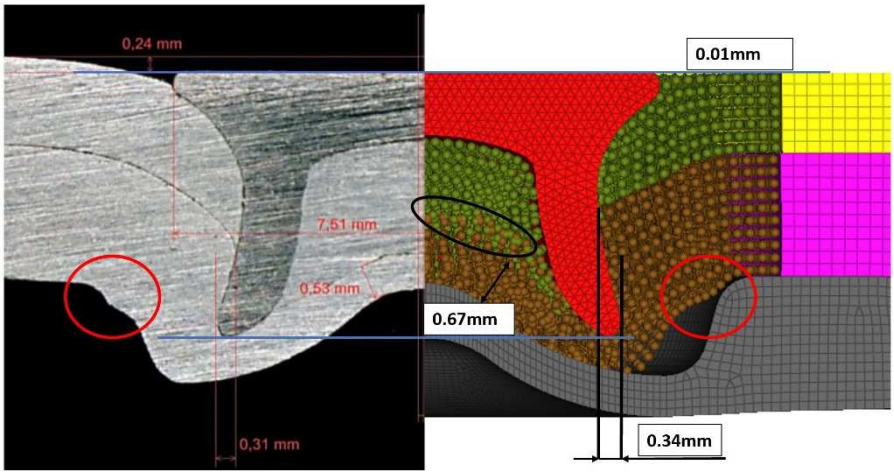

Figure 81 Comparison of the microsection (left) and SPG simulation (right)

6.2.5.2 Effective plastic strain and stress interpretation (baseline SPG model)

Figure 82 illustrates the effective plastic strain field (left column) and stress field (right column) at the final position of the SPR setting process. The highest strain value (roughly 2.6) occurs in the inner area of the rivet, and the upper sheet near the contact point of the upper sheet, lower sheet, and the rivet. This is because the rivet stretches or pulls the upper sheet into the final position. Also, a higher plastic strain occurs in the bulge of the die because of the deformation due to the spreading of the rivet. The plastic strain field has a good correlation with the 2D setting simulation described in section 5.5.1.

In the right column of Figure 82, the stress field (von Mises) is visualised. The magnitude of the stress field reaches values up to 370 MPa. In the upper sheet, in the area where the sheet is compressed, high stress values occur. Furthermore, the stress field looks quite similar to the 2D model (section 5.5.1).

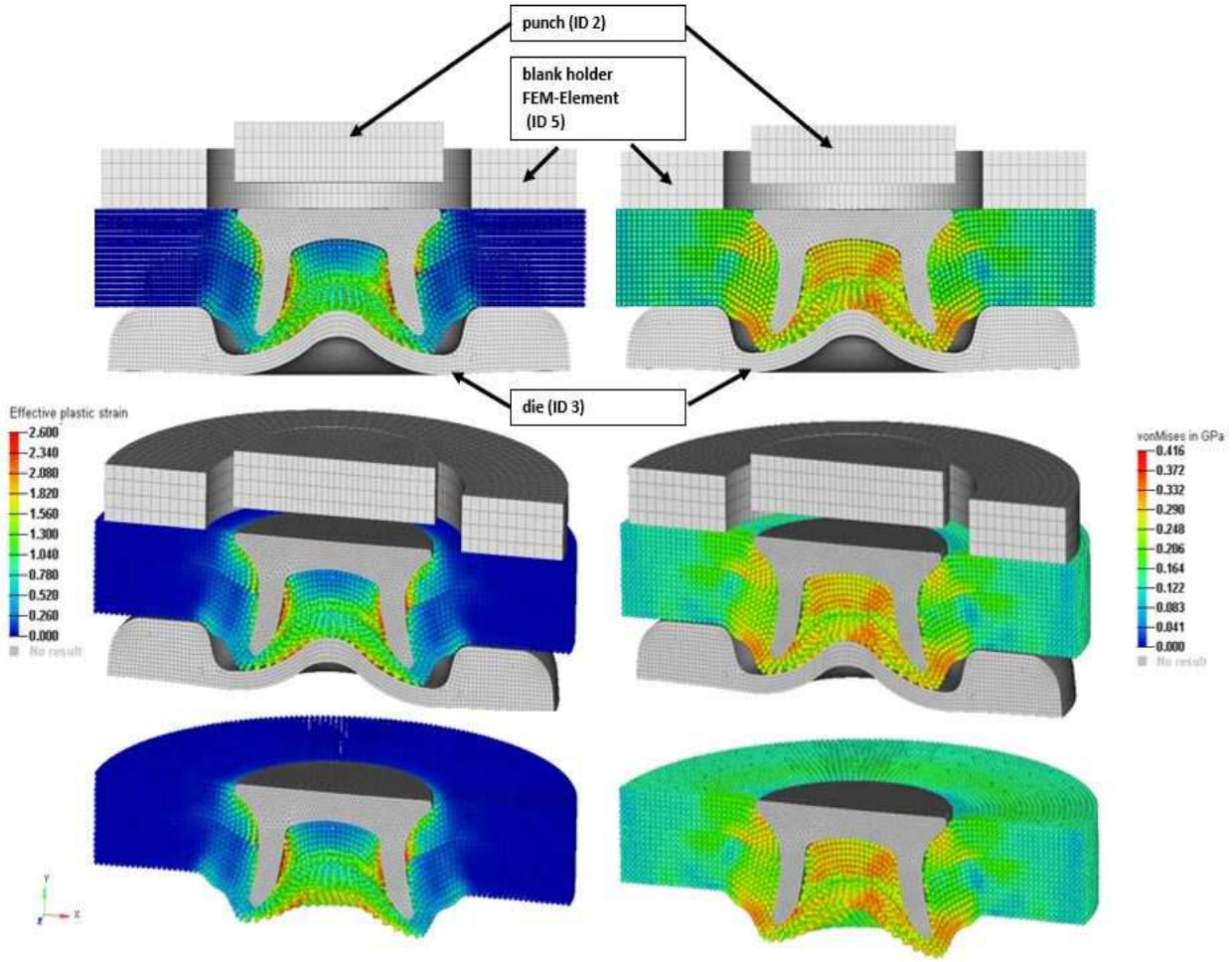

Figure 82 Effective plastic strain field (left column) and stress field (right column) of the basic SPG model

6.2.5.3 Force-displacement curve of the basic SPG model

In Figure 83, the force-displacement curve of the setting process is illustrated. In that figure, the 2D force-displacement curve (orange curve) is compared to the 3D one of the basic SPG simulation (green curve). The correlation of the 2D curve is described in section 5.5.2. The overall comparison shows quite good accordance. The maximum force achieved in the simulation is comparable to the 2D simulation and is roughly at the same peak at 55kN. There are some small deviations between the shape of the two curves. Both start at 10kN because the clamping force of the blank holder is included. The reason for that is the arrangement of the force sensor in the SPR gun. In the first 2.5mm, the 3D curve is slightly higher than the 2D result. The average force difference is about 10 per cent in the first section. Between 2.5mm and 3.5mm, the shape of the curves correlate very well. From 3.5mm, the 3D curve increases faster than the 2D curve.

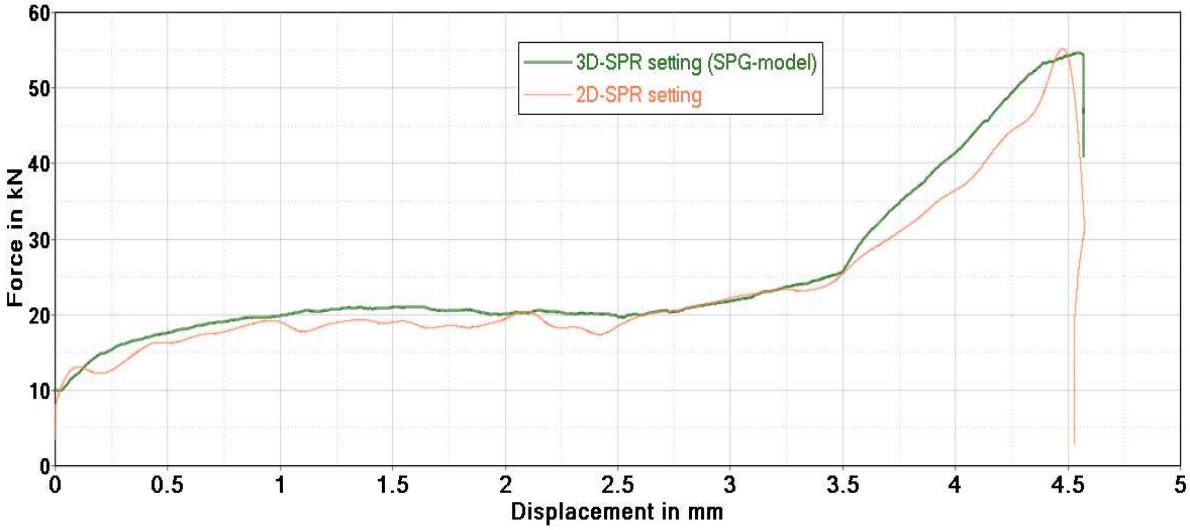

Figure 83 Force-displacement curve of the basic SPG model

Concluding the results, the 3D basic SPG model shows a good correlation between the simulation and the experiment in terms of deformation and force-displacement curve. This basic SPG model is used in the following investigations of the misalignment of the rivet and tilting of the die, which can occur during the setting process of the rivet.

6.2.6 Eccentricity influence analysis (basic SPG model)

For the investigation of the misalignment of the rivet, two simulations were performed with an eccentricity of 0.2mm and 0.4mm. The boundary conditions of the numerical simulation are the same as in the basic SPG model. Only the rivet was moved in horizontal direction as shown in Figure 84.

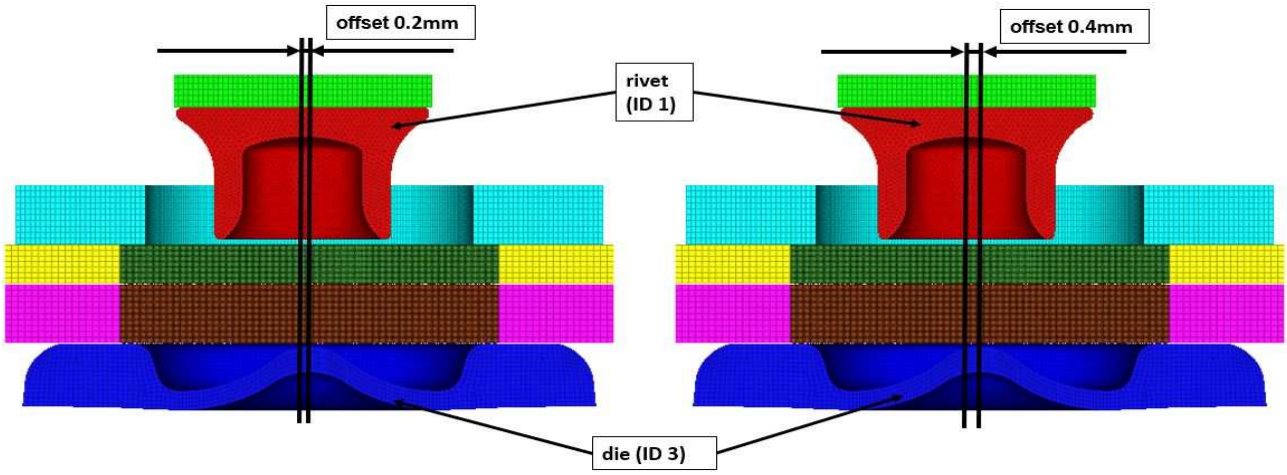

Figure 84 Basic SPG model with 0.2mm (left picture) and 0.4mm (right picture) offset

6.2.6.1 Validation of the deformation behaviour

In Figure 85 and 86, the microsections with 0.2mm and 0.4mm eccentricity are compared to the result of the numerical simulations where Figure 85 represents the 0.2mm and Figure 86 represents 0.4mm eccentricity. The pictures show the main geometrical features of the joint.

For the simulation of 0.2mm eccentricity, the horizontal interlock on the right side shows a difference between the numerical simulation and the experiment of about 0.05mm (simulation 0.34mm versus experiment 0.29mm) and on the left side a difference of 0.06mm (simulation 0.32mm versus experiment 0.26mm). Both the simulation and the microsection show a lower horizontal interlock on the left side and a higher horizontal interlock on the right side, which is clearly because of the eccentricity. In the experiment, the difference between the left and right sides is about 0.03mm, and in the simulation, it is about 0.02mm; that means roughly a 5 per cent difference and quite high accordance.

The optical analysis of the simulation and the microsection also shows a very good accordance. The main feature, the filling of the die and, therefore, the development of the closing head, is marked in the yellow and red encircled area. The yellow areas show a slight difference from the experiment, whereas the red encircled areas correlate very well.

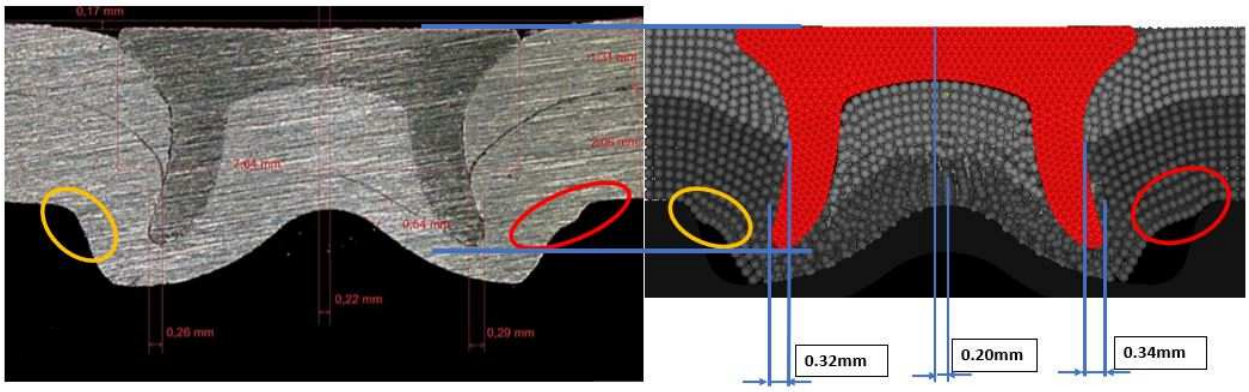

Figure 85 Comparison of experiment (left columns) and simulation (right columns) for 0.2mm eccentricity

In general, the results for the 0.4mm eccentricity of the rivet show a similar accordance of the horizontal interlock, residual wall thickness, and deformation. One main occurrence is the increasing horizontal interlock on the left side since more material of the lower aluminium sheet is flowing into the left side of the die and presses with a higher force against the left leg of the rivet, which leads to a higher deformation. This material flow is marked with a green circle in Figure 86 and can also be observed in the numerical simulation.

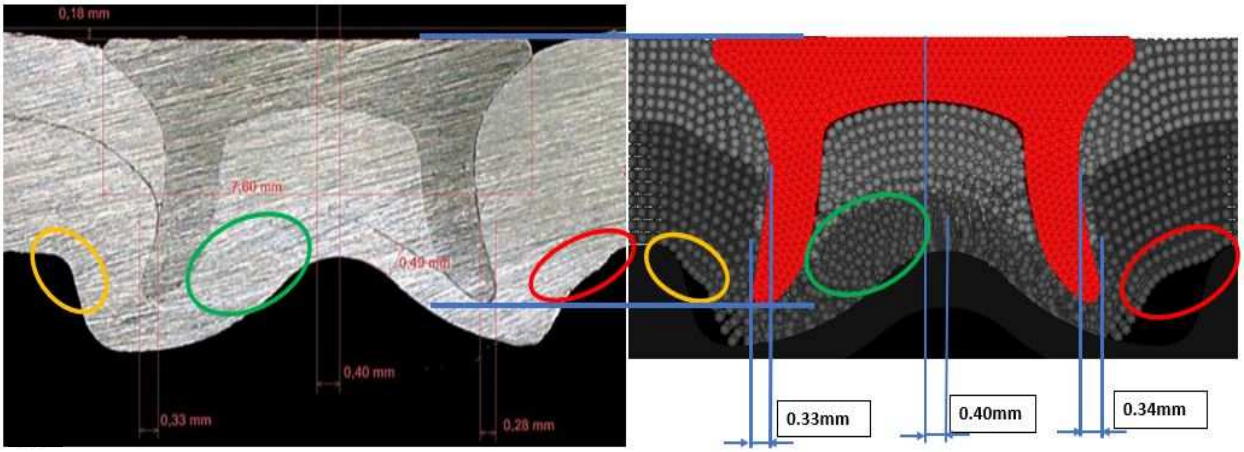

Figure 86 Comparison of experiment (left columns) and simulation (right columns) for 0.4mm eccentricity

6.2.6.2 Effective plastic strain and stress (von Mises) for 0.2mm eccentricity

In Figure 87, the effective plastic strain (left column) and the von Mises stress (right column) are shown. The areas with the highest plastic strain and stress are the same as in the basic SPG model, and therefore no special differences occur.

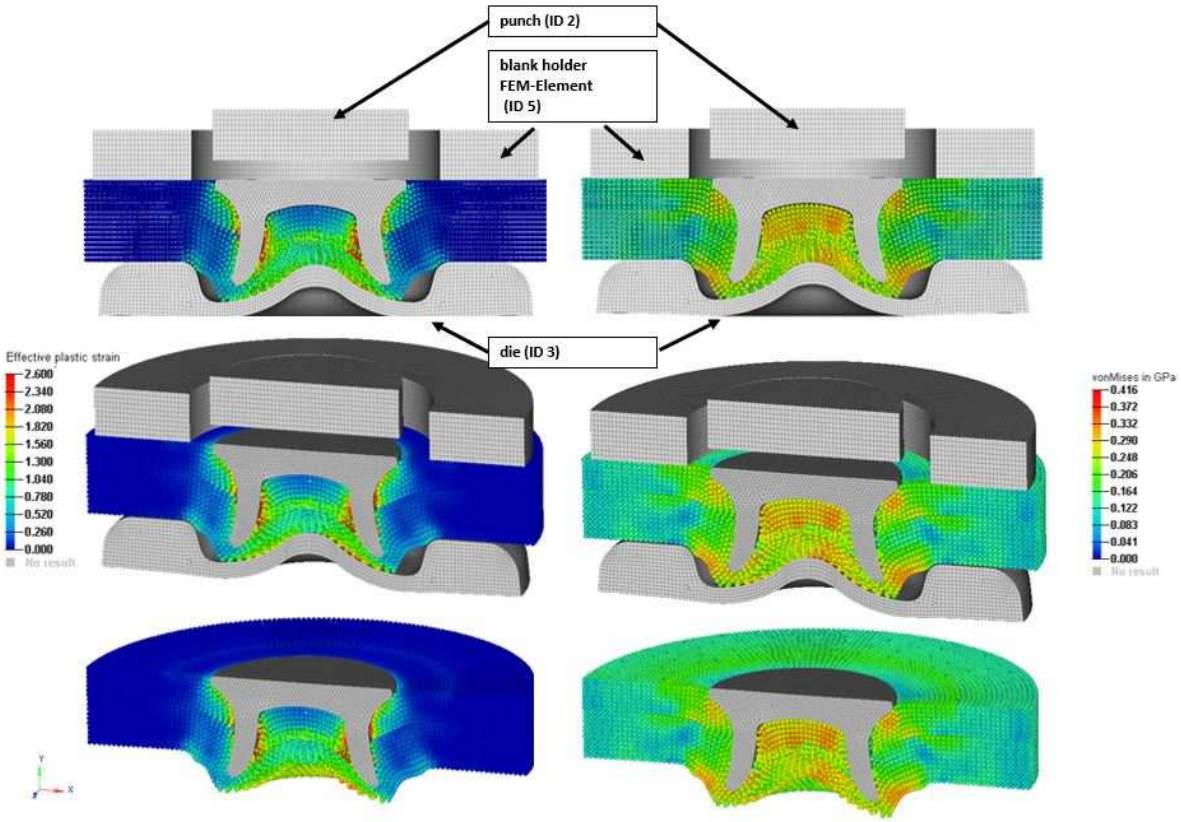

Figure 87 Effective plastic strain field (left column) and von Mises stress field (right column) of the basic SPG model with 0.2mm eccentricity

6.2.6.3 Effective plastic strain and stress (von Mises) for 0.4mm eccentricity

In Figure 88, the effective plastic strain (left column) and the von Mises stress (right column) for 0.4mm eccentricity are shown. Furthermore, this offset simulation only shows small deviations compared to the basic SPG model.

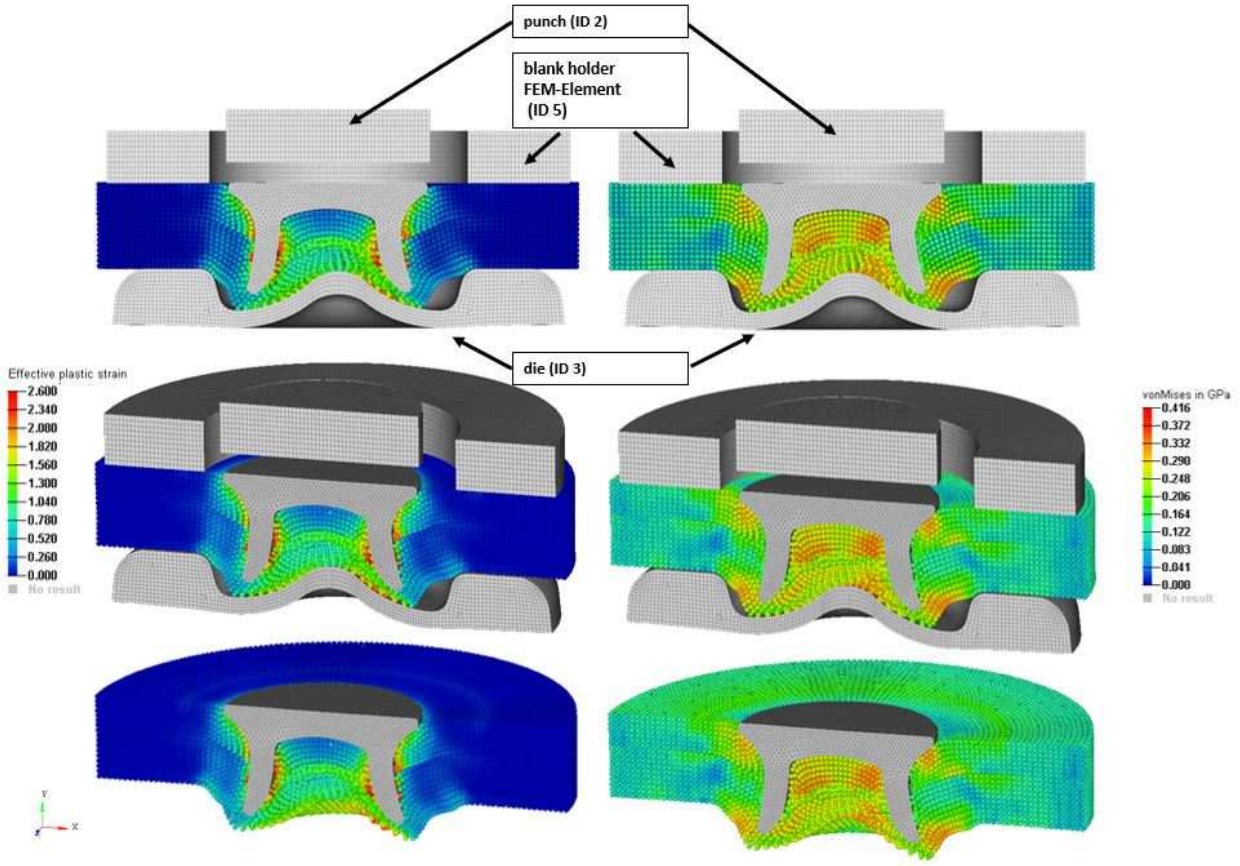

Figure 88 Effective plastic strain field (left column) and von Mises stress field (right column) of the basic SPG model with 0.4mm eccentricity

6.2.6.4 Comparison of Force-displacement curves

The different force-displacement curves of the simulations are illustrated in Figure 89. In this diagram, the main difference of the various simulations is a small deviation at the end of the curve. The comparison shows that the eccentricity of the rivet has nearly no, or only negligible, influence on the force-displacement curve. That means for the real process, the eccentricity is not observable in the force-displacement curve.

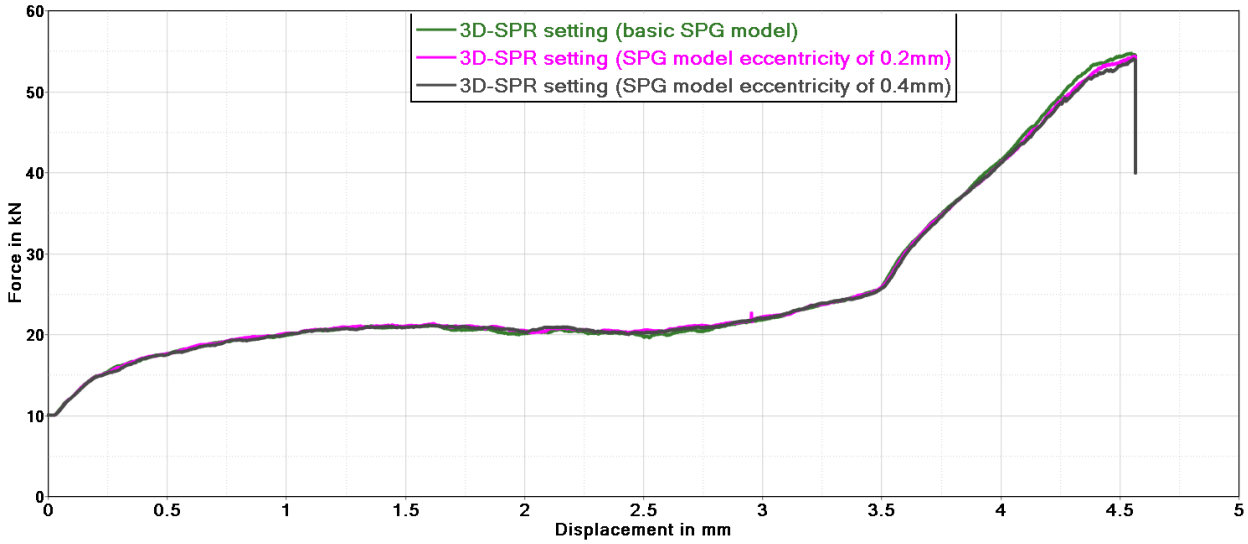

Figure 89 Comparison of force-displacement curve of the basic SPG and eccentricity simulation

6.2.7 Influence of die tilting (basic SPG model)

Another problem which can occur during the setting process of the rivet is the tilting of the die because of the elastic deformation of the C-frame. To investigate tilting, the die is rotated around the z-axis. A one- and two-degree tilt angle was investigated. The remaining boundaries are the same as in the basic SPG model (described in section 6.1.4). Those setups are illustrated in Figure 90.

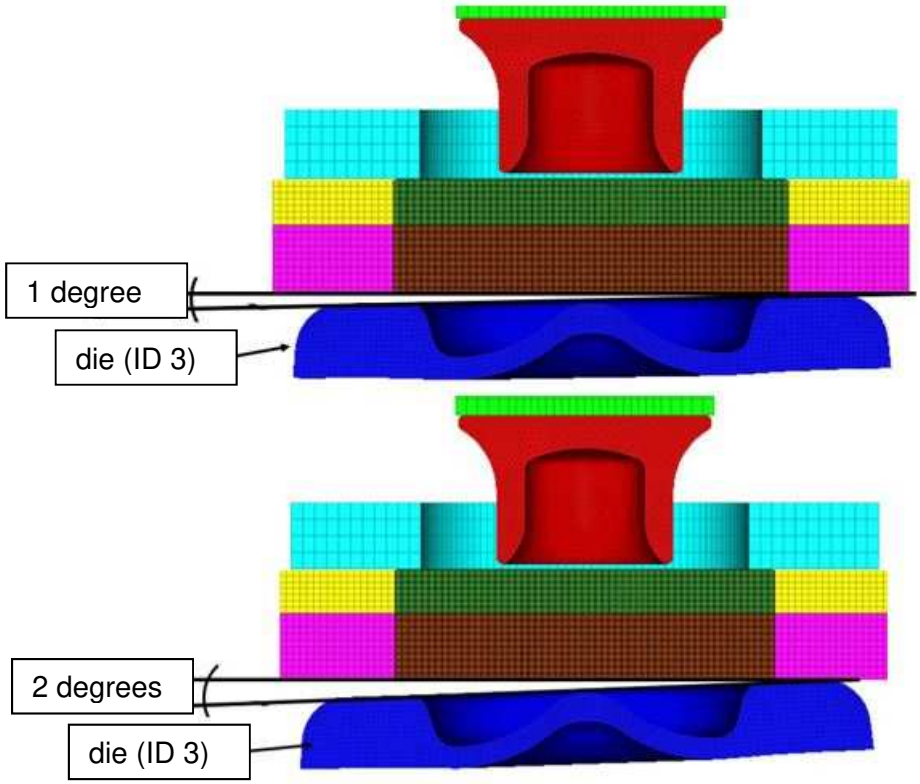

Figure 90 SPG model for tilting: upper picture 1°, lower picture 2°

6.2.7.1 Result of one-degree die tilting (basic SPG model)

The result of the one-degree tilting is shown in Figure 92 a) to e). However, there are no microsections available for the comparison of the one- and two-degree tilting.

Analysis of the one-degree simulation result

Figure 91 shows the final position of the one-degree die tilting simulation. In this picture, the areas of interest are encircled in different colours. Because of the tilting in the black encircled area, a deformation of the lower aluminium sheet occurs. If this deformation also occurs in the experiment, it would be an optical feature for the validation of the simulation result. The blue and green circles show the development of the closing head, which is not as well developed as in the basic SPG model. Another area of interest is the yellow encircled one, which shows the residual wall thickness of the left side. A higher wall thickness occurs there because there is more space for the material which flows into that area due to the die tilting. The left side has a minimal residual wall thickness of about 0.66mm and the right side of about 0.51mm. The orange encircled area shows the lower deformation near the rivet head and that the deformation in this area is more strongly developed than on the opposite side. Figure 91 illustrates the horizontal interlock, and it is observable that the left side has a lower horizontal interlock with 0.29mm compared to the right side with 0.32mm, which is quite similar to the basic SPG model.

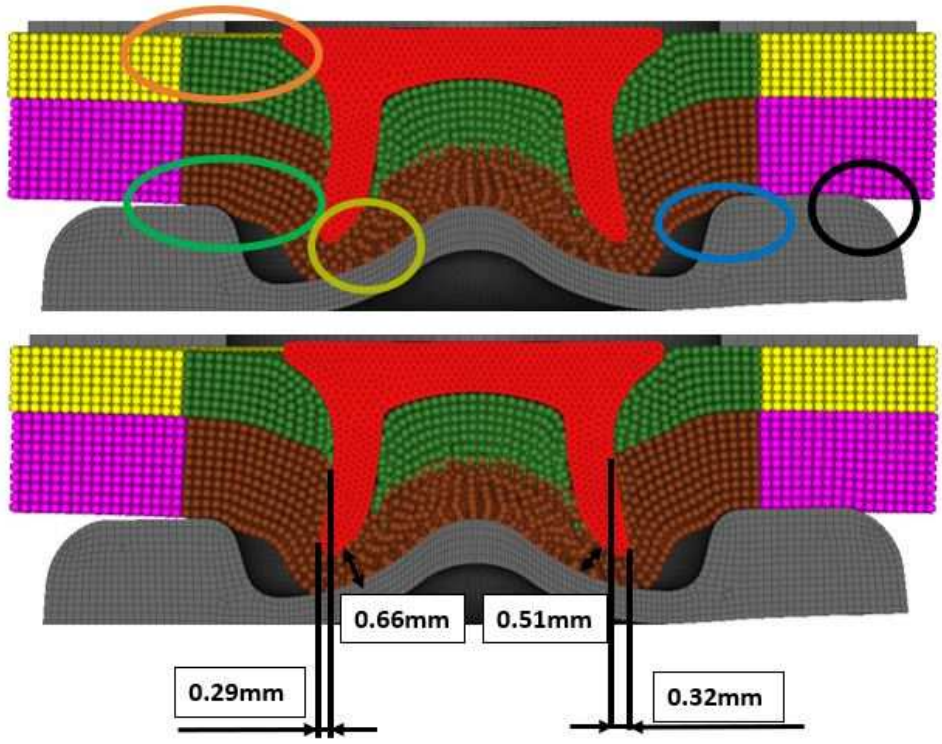

Figure 91 Simulation result of the deformation of the 1° tilting

Effective plastic strain and stress analysis of the one degree die tilting simulation

Figure 92 shows the stress (von Mises) and effective plastic strain analysis of the simulation. The left side of the picture, (a) and (d), shows the strain and the right side, (b) and (e), shows the stress analysis. The main difference with the basic SPG model is encircled in white (strain field) and black (stress field). This difference is due to the deformation of the lower sheet on the right side by the clamping area. The picture illustrates a higher level of stress on the upper (~250MPa) and lower sheets (~300MPa). Furthermore, the effective plastic strain is higher than in the basic SPG model.

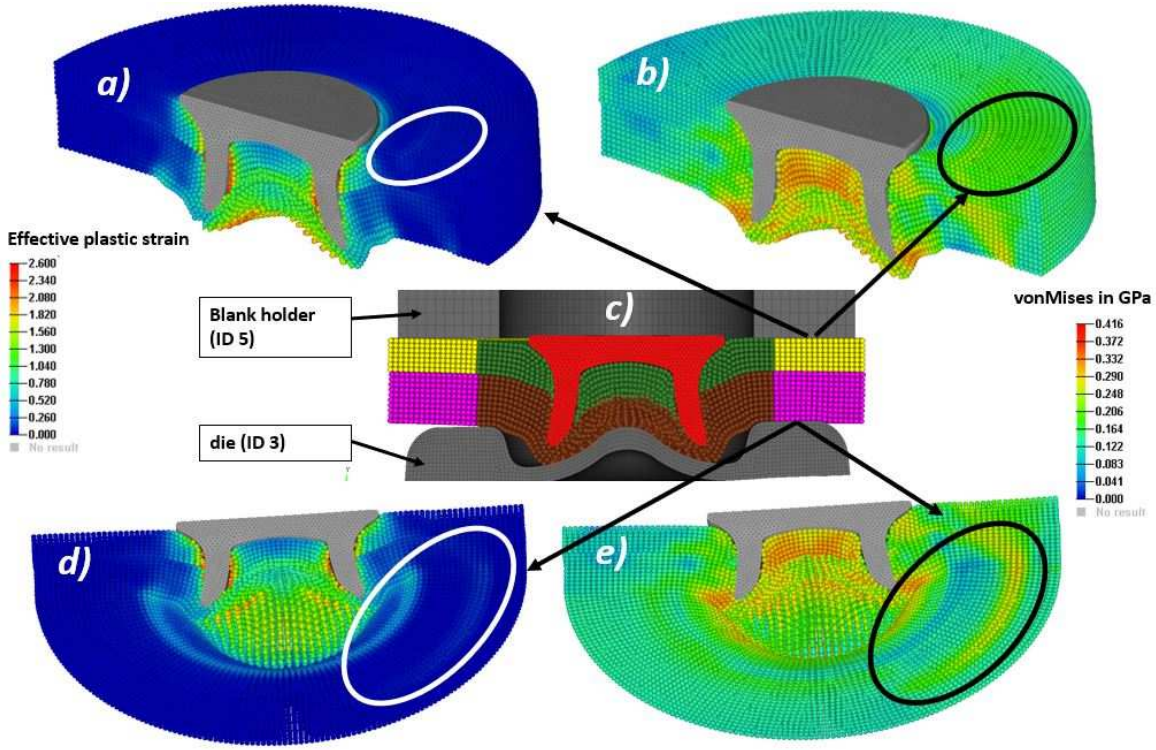

Figure 92 Effective plastic strain field (a) and (d) and von Mises stress field (b) and (e) of the basic SPG model with 1° tilting of the die

6.2.7.2 Result of two-degree die tilting (basic SPG model)

Analysis of the two-degree simulation result

The result of the two-degree simulation is illustrated in Figure 93. The main points described in the one-degree simulation are similar to those in the two-degree simulation. Again, in the black encircled area, there is a deformation which would be an optical feature for the validation of the simulation result. In the green encircled area (closing head on the left side), less deformation occurs, and the residual wall thickness increases on the left side up to 0.76mm compared to the right side with 0.58mm. The orange encircled area shows a much smoother deformation than on the right side. The horizontal interlock decreases at both sides. On the left side, the interlock is about 0.21mm, and on the right side, it is about 0.28mm.

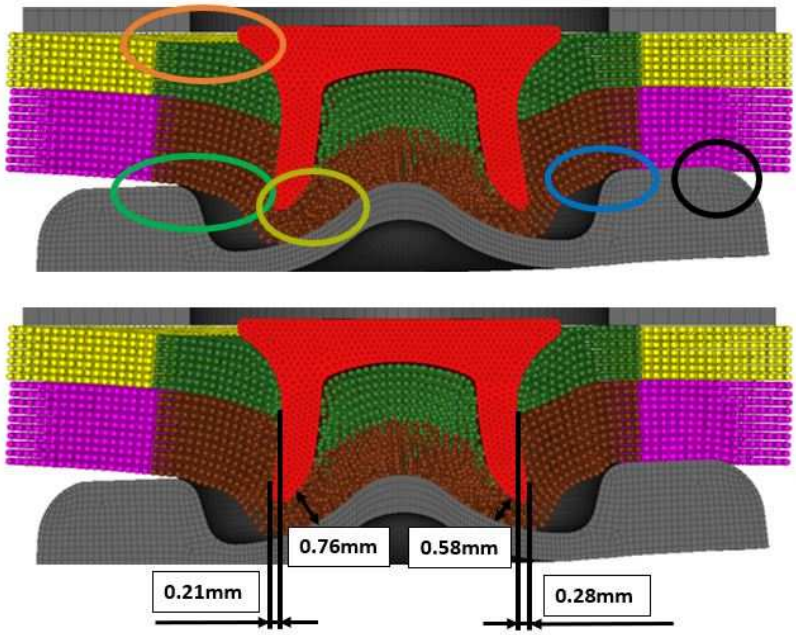

Figure 93 Simulation result of the deformation of the 2° tilting

Effective plastic strain and stress analysis of the two-degree die tilting simulation

Figure 94 shows the stress and effective plastic strain analysis of the two-degree numerical simulation. In general, similar effects occur as in the one-degree tilting simulation. Moreover, the values occurring in the two-degree simulation results are comparable to those of the one-degree simulation.

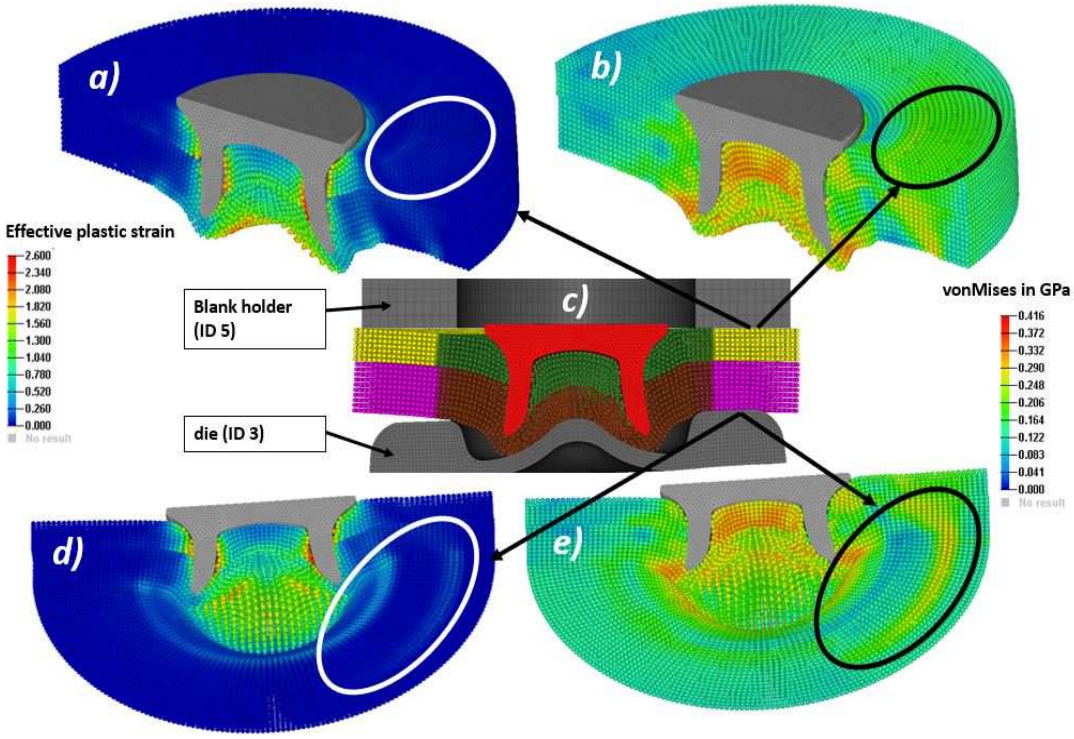

Figure 94 Effective plastic strain field (a) and (d) and von Mises stress field (b) and (e) of the basic SPG model with 2° tilting of the die

Summarising the obtained results, more tilting of the die leads to lower joint quality and increases the chance of producing defective joints.

6.2.7.3 Comparison of the force-displacement curve (basic SPG model)

The first third of the force-displacement curves of the different joints are similar until 3mm displacement. From 3mm, the curves start to differ from each other. One main difference is the maximum force, which decreases. In the basic SPG simulation, the maximum force reaches about 55kN. In the one-degree simulation, the maximum force decreases to 52kN, and in the two-degree simulation, it goes down to 48kN. The comparison of the force-displacement curves is shown in Figure 95.

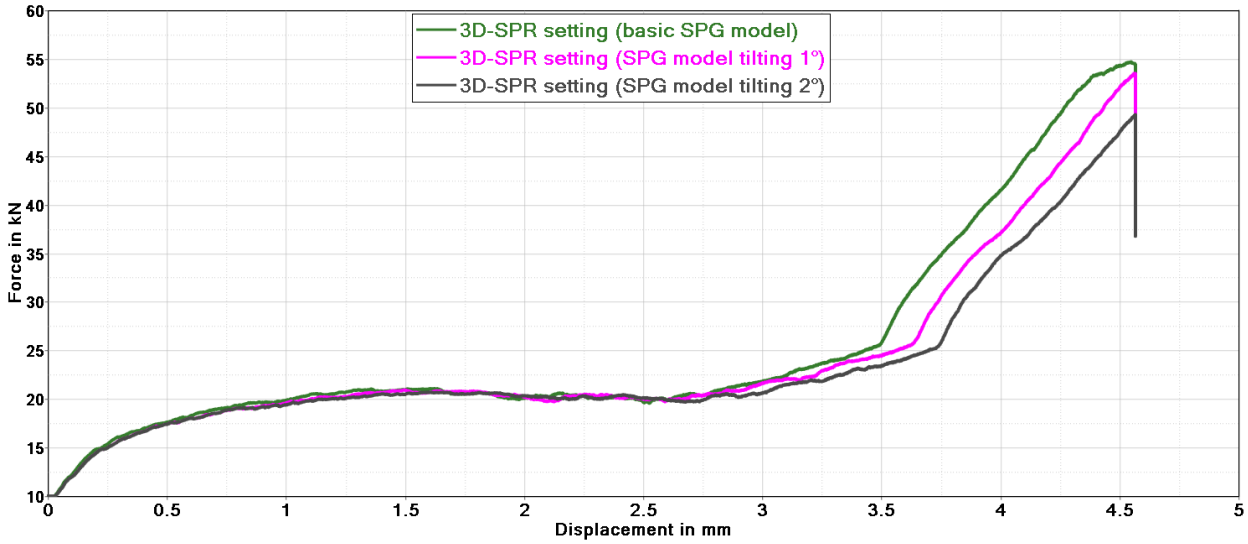

Figure 95 Comparison of force-displacement curve of the basic SPG and tilting simulation

For the simulation model in section 6.2, the die is fixed in all degrees of freedom. In the experiment, the tool has a certain stiffness because of its design (C-frame), and therefore the whole tool deforms elastically. For the SPR joint investigated in this thesis, the tool moves about 1.6mm. The stiffness of the tool is implemented in the next section. That means that the die, punch, blank holder, sheets, and rivet must move downwards. The 3D basic SPG model used must be modified to fulfil this requirement, which is described in the next section.

6.3 Modified 3D SPG model

The elastic deformation of the tool was implemented for the following simulations. This stiffness of the C-frame was integrated into the simulation by assigning numerical springs to the die. In the previous chapter, the die was fixed in all six degrees of freedom, and so no movement could occur. By implementing a spring below the die, it can move downwards. For the modified basic SPG model, five degrees of freedom were locked, namely, x- and z-translation and rotation around x-, y-, and z axis. This setup was also used for the investigation of the misalignment of the rivet. To investigate the tilting of the die, two springs were implemented, one with a lower stiffness to realise a rotation of the die during the processing. For this analysis, the rotational degree of freedom around the z-axis was not locked.

One major problem occurred during the simulation which required a change from the SPG element definition from the Eulerian kernel to the updated Lagrangian kernel. This was done in the section card of the SPG parts. During the simulation, the SPG particles behaved in a very instable manner, and at some point, the particles started to leave the parts boundary. This is shown in Figure 96. Although some parameters were changed, the problem still remained, especially after the piercing of the top sheet. With the updated Lagrangian kernel, those problems could be solved. For this reason, the simulations in this section were performed with the updated Lagrangian kernel. With this method, the force-displacement curve shows some artefact which is analysed later.

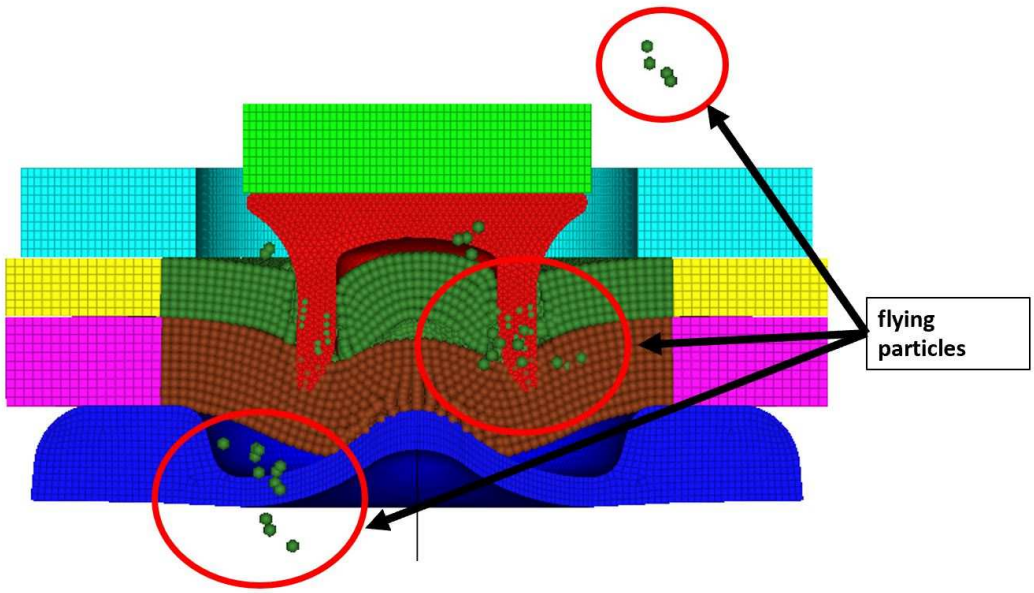

Figure 96 Problems with SPG model and Eulerian kernel

6.3.1 Modified SPG model

The modified SPG model consists of the same parts as the basic SPG model described in section 6.2.1. However, the modified model includes a numerical spring which allows the movement of the die. The main purpose of the spring was to create a counterforce, and its stiffness was defined as 25kN/mm. A discrete element was used to model the spring, *SECTION_DISCRETE, with the material definition *MAT_SPRING_ELASTIC. With the option *BOUNDARY_PRESCRIBED_MOTION, the movement of the die was prescribed. The model of the modified baseline SPG model is illustrated in Figure 97. The velocity of the rivet was changed to 100mm/s to speed up the simulation. The friction definitions are the same as defined in Table 8 (section 6.2.2).

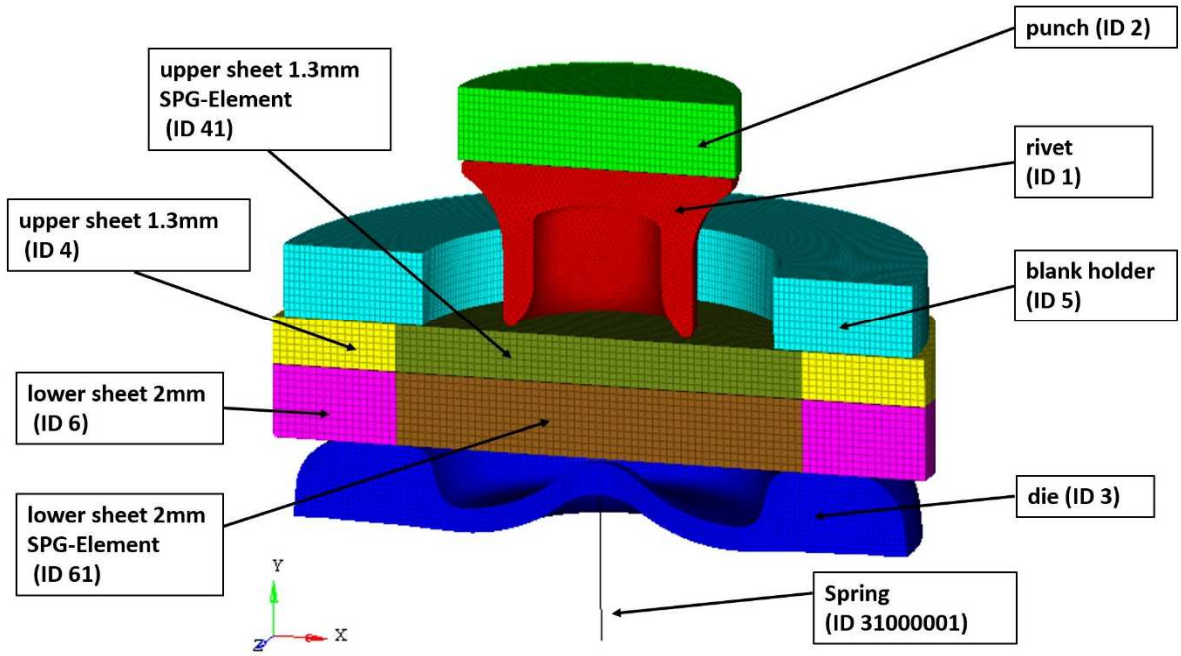

Figure 97 Modified SPG model

6.3.2 Results of the modified SPG model

The following section explains the results of the modified SPG simulation. First, the deformation behaviour of the joint is evaluated, followed by the effective plastic strain, stress (von Mises), and force-displacement curve of the 3D SPG setting process.

6.3.2.1 Geometrical investigation of the simulation result (modified SPG model)

Figure 98 illustrates the results of the setting process. The deformation and the main geometrical features, like the closing head and the spreading of the rivet, are comparable to the experiment.

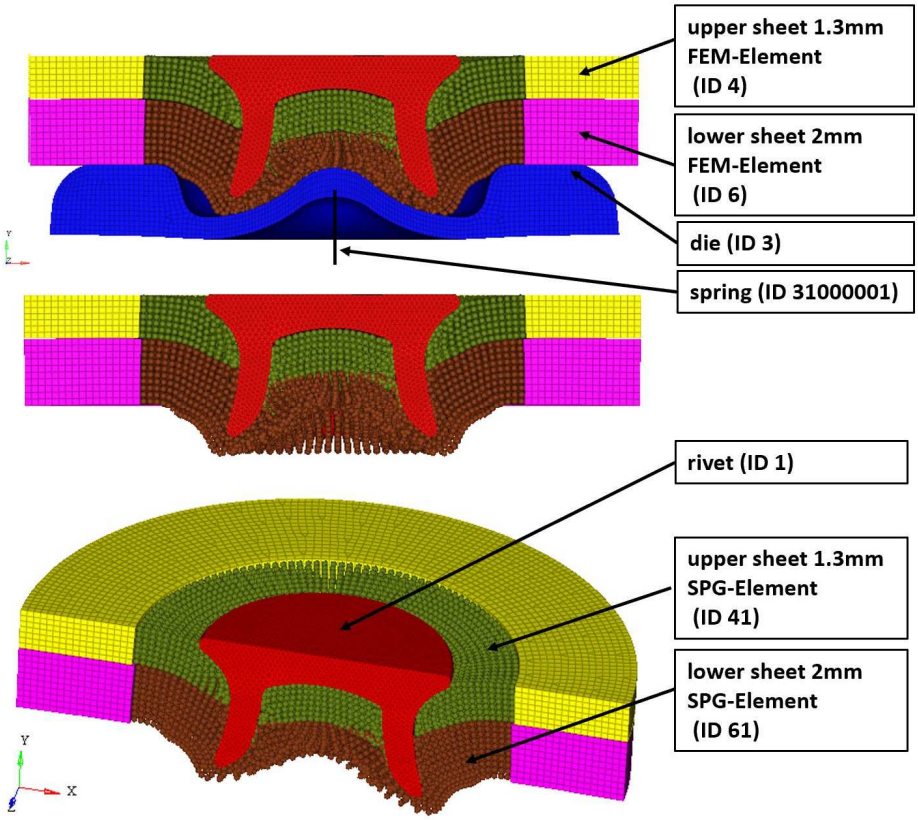

Figure 98 Simulation result of the modified SPG model

A comparison of the experiment (a), the basic SPG (b), and the modified SPG (c) simulation result is illustrated in Figure 99. The horizontal interlock increases slightly in the modified SPG model compared to the basic SPG model. This is negligible, and so the results of the simulation represent the experiment quite well. Moreover, the development of the closing head looks very similar to the experiment.

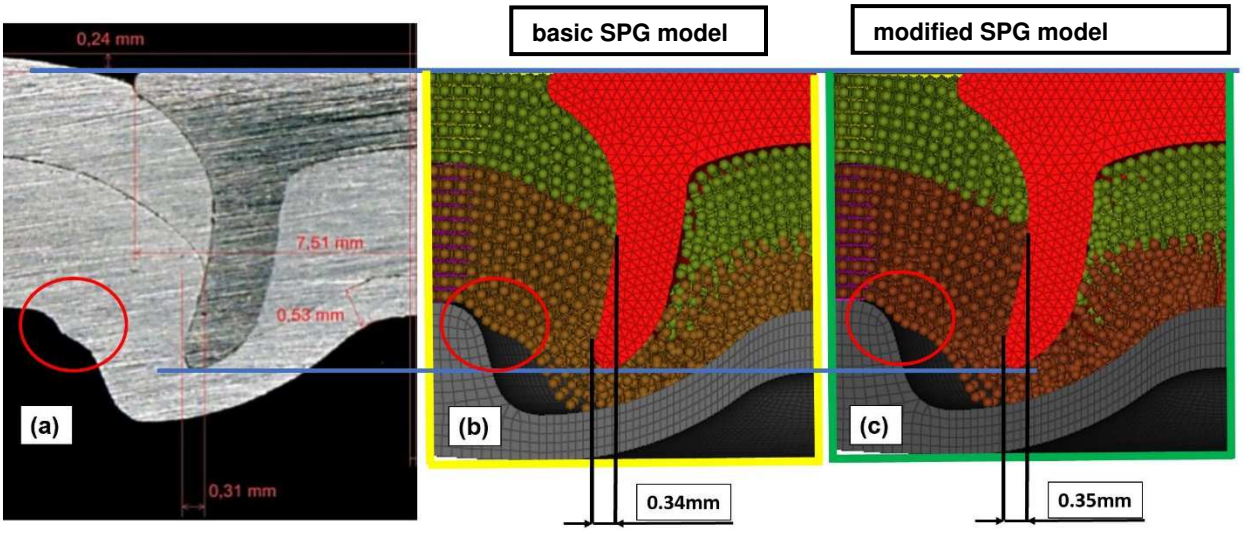

Figure 99 (a) Comparison of microsection, (b) basic SPG result, (c) modified SPG result

6.3.2.2 Effective plastic strain and stress (von Mises) analysis (modified SPG model)

Figure 100 depicts the effective plastic strain of the basic SPG model, (a) left column, and the modified SPG model, (b) right column. Comparing those simulations, the main difference is the maximum value of the plastic strain. In the basic SPG model, it is higher (~2.5) than in the modified simulation (~1.9). This could be traced back to the SPG element formulation with the updated Lagrangian kernel. The biggest strains occure in the same area of the joint, but the values of the modified simulation are lower.

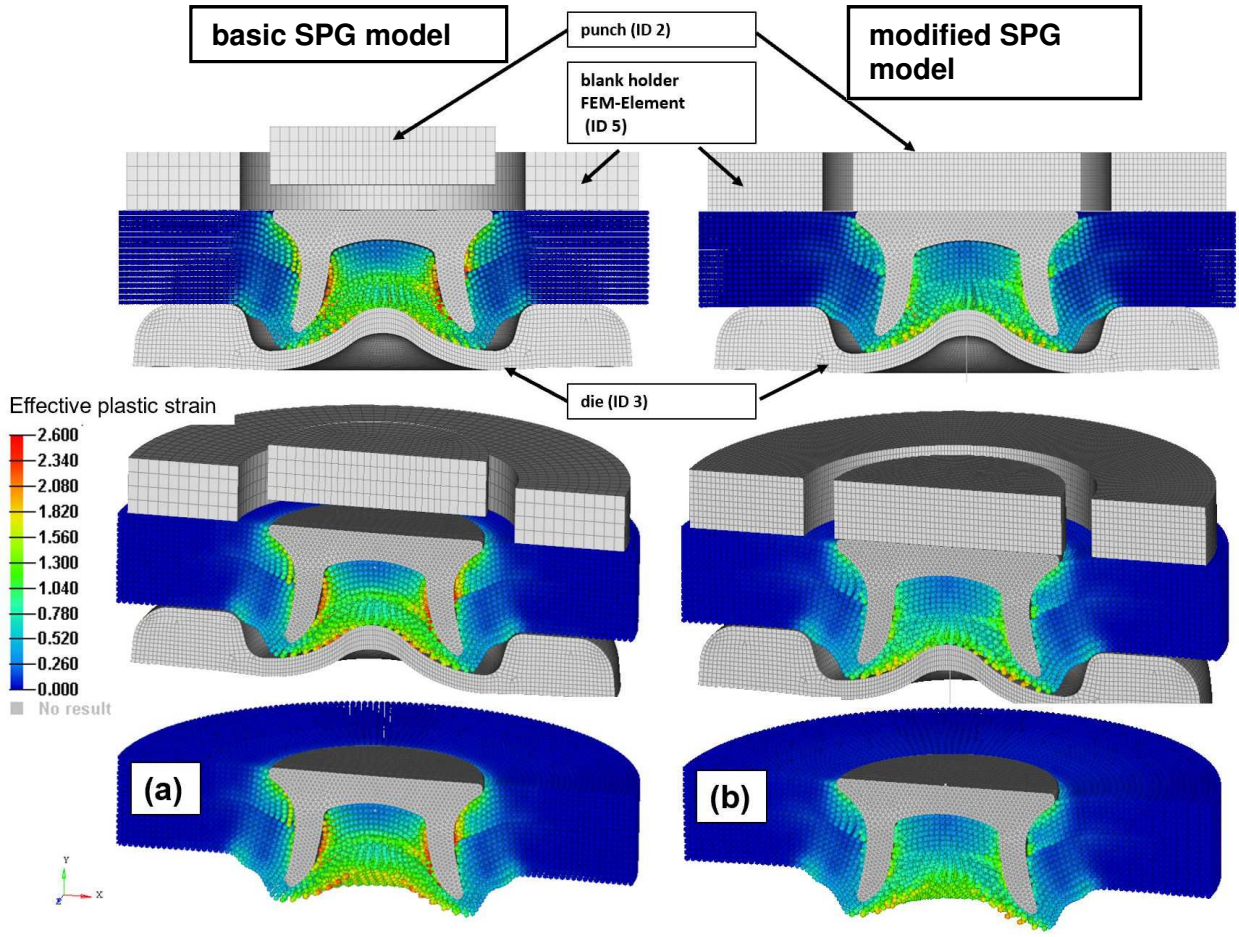

Figure 100 Comparison of effective plastic strain field: (a) basic SPG model and (b) modified SPG model

The stress comparison of the two SPG models is shown in Figure 101, where in (a) the basic SPG model and in (b) the modified SPG model is illustrated. The stress field analysis shows some minor differences. The maximum values are of the same order of magnitude, but the areas where they occur are slightly different. Overall, these differences are negligible.

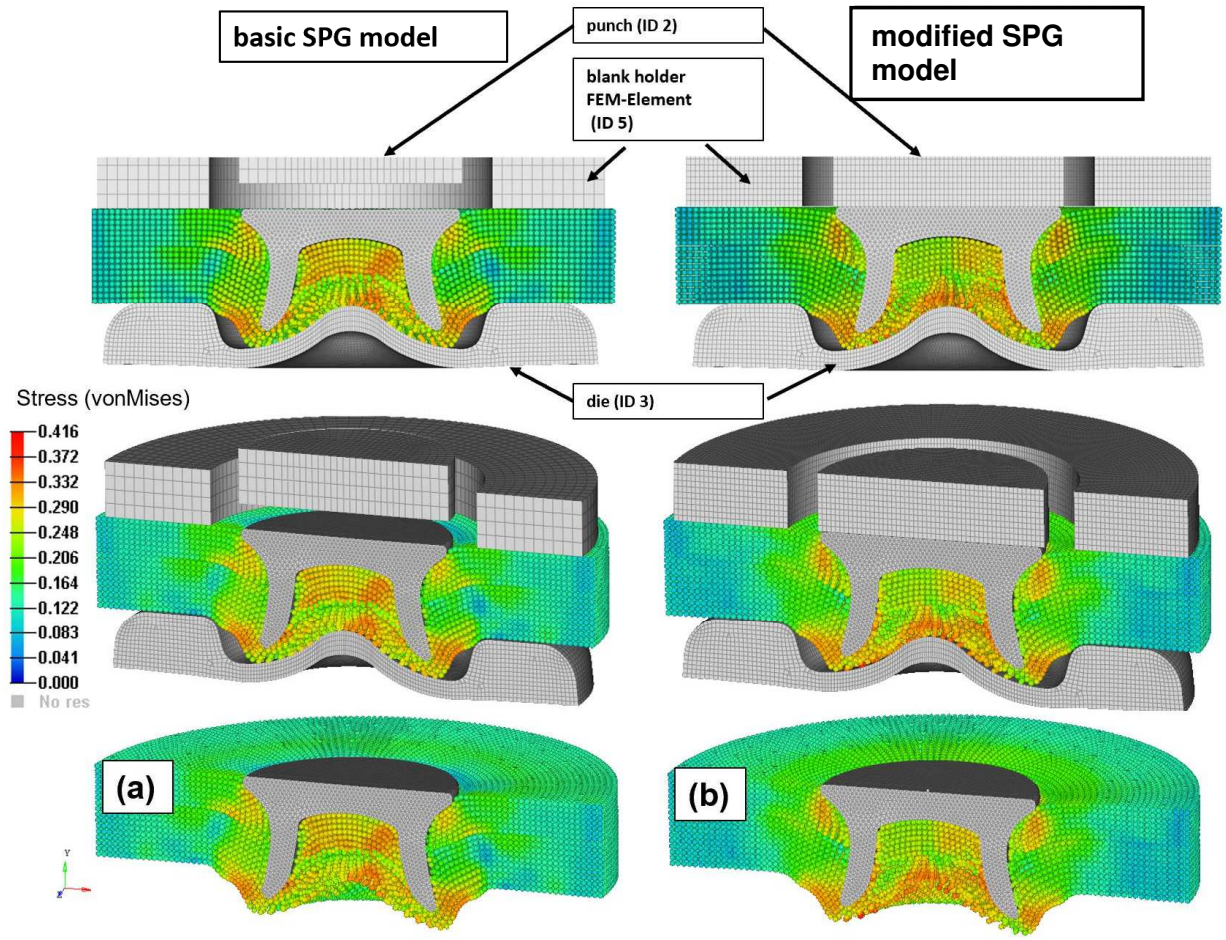

Figure 101 Comparison of stress field: (a) basic SPG model and (b) modified SPG model

6.3.2.3 Force-displacement curve of the modified SPG model

Figure 102 illustrates the force-displacement curve of the modified SPG model (green) compared to the experimental data (blue). The shapes of the curves are very similar, but there are some differences between the two curves, which is a problem with the updated Lagrangian kernel. For the first 2.2mm, the curve is identical to the experiment. At the point where the upper sheet is pierced, an increase of force is observed in the simulation. This is because the updated Lagrangian kernel supports no failure; only the connection between the particles was stretched, which leads back to a higher force in the simulation. Therefore, between 2.2mm and 3.5mm, a deviation of about 3kN occurs. The simulation also reaches the maximum value of about 50kN. Overall, there is a small deviation between the 3D modified SPG model and the experiment, but, in summary, the accordance is satisfying.

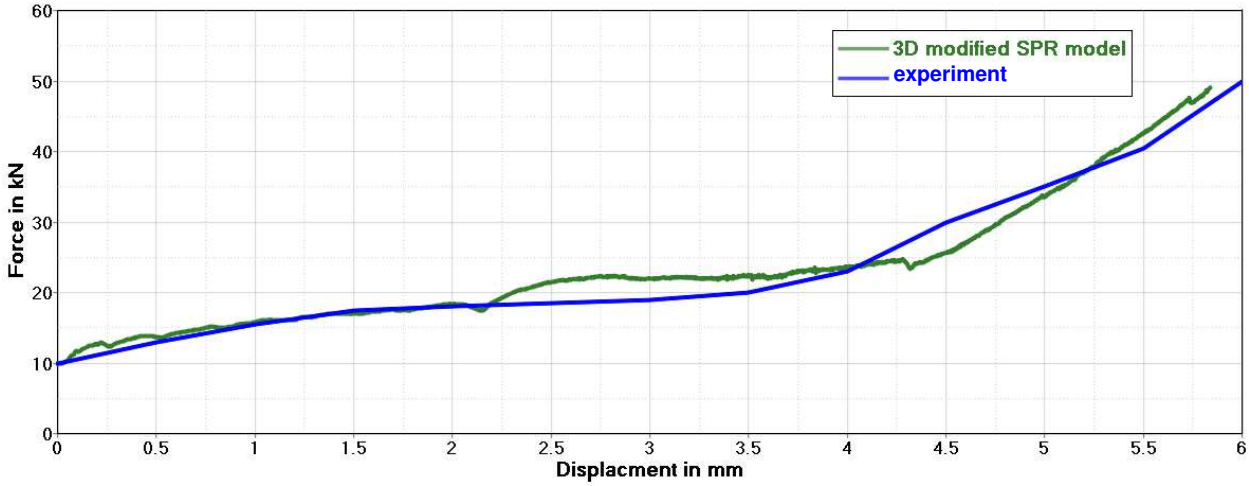

Figure 102 Force-displacement of modified SPG model (green) compared to the experiment (blue)

6.3.3 Eccentricity influence analysis (modified SPG model)

The following section shows the results of the modified basic SPG model in terms of the eccentricity. The deformation of the rivet is evaluated first, followed by the effective plastic strain field, the stress field (von Mises), and the force-displacement curve.

6.3.3.1 Validation of the deformation behaviour (eccentricity, modified SPG model)

The eccentricity of the basic SPG model (b)(e), modified SPG model (c)(f), and microsection (a)(d) of such a joint are compared in Figure 103. In the left column, the results with 0.2mm eccentricity and, in right column, the results with 0.4mm eccentricity are illustrated.

The comparison of the models with different offsets shows a very similar horizontal interlock with an increased correlation for the modified SPG model (c)(f). The illustration shows an average deviation of the interkock for the 0.2mm offset of about 10 per cent and for the 0.4mm offset of about 7 per cent referring to both sides (average).

The geometrical features of the different eccentricity simulations, like the closing head, are again very similar between the basic SPG result and the modified SPG result, which reflects the experiment quite well. This can be seen in the yellow and red encircled areas in Figure 103.

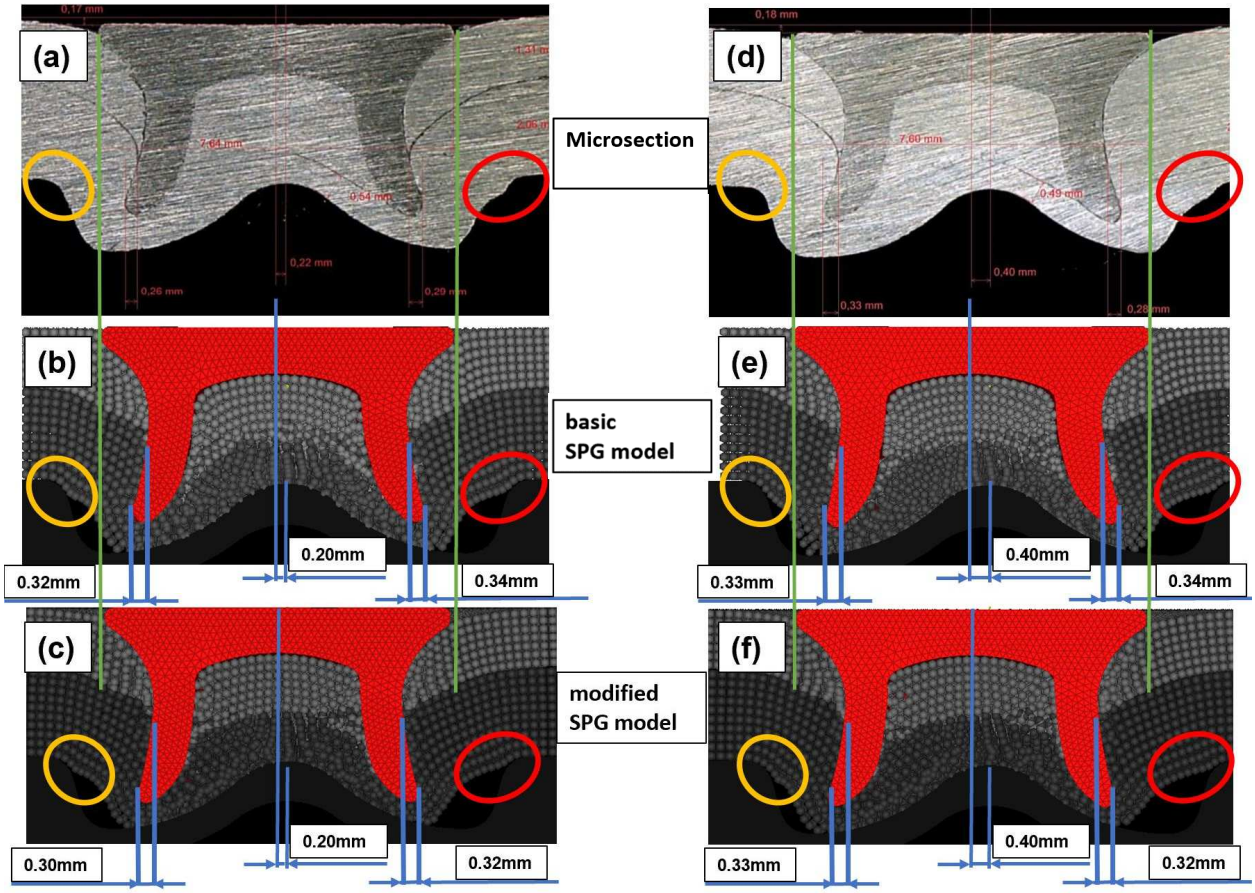

Figure 103 Comparison of eccentricity (0.2mm, 0.4mm) amongst microsection (a)(d), basic SPG model (b)(e), and modified SPG model (c)(f)

6.3.3.2 Effective plastic strain and stress analysis (eccentricity, modified SPG model)

In Figure 104 and 105, the stress field (von Mises) and effective plastic strain field of the different levels of eccentricity are illustrated. For the 0.2mm offset (Figure 104 c, d), the results are quite similar to the modified SPG simulation. The stress fields are of the same order of magnitude, but there are some small deviations in the area where the stress occurs. The stress field of the 0.4mm offset reflects the same similarity (Figure 105 c, d).

In the effective plastic strain field, the difference between the basic SPG model and the modified SPG model is in the maximum value (Figure 104 a, b and 105 a, b). In the basic SPG model, the values are higher than in the modified model. Comparing the numbers, the basic model shows a plastic strain of about 2.6 and the modified model roughly 1.9, which means that there is a difference of about 0.7 or a deviation of 27 per cent. The main difference appears in the area of the pierced upper aluminium sheet. That could be caused by the change from the Eulerian to the updated Lagrangian kernel.

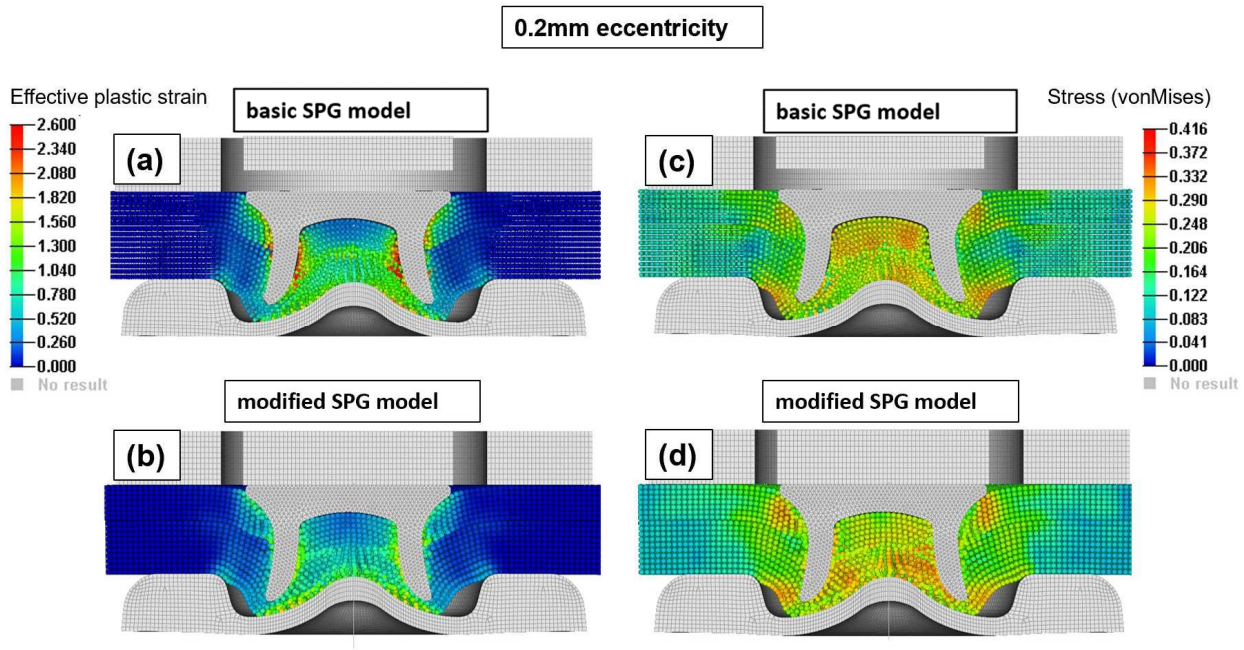

Figure 104 Comparison eccentricity of 0.2mm basic SPG model (a)(c) and modified SPG model (b)(d)

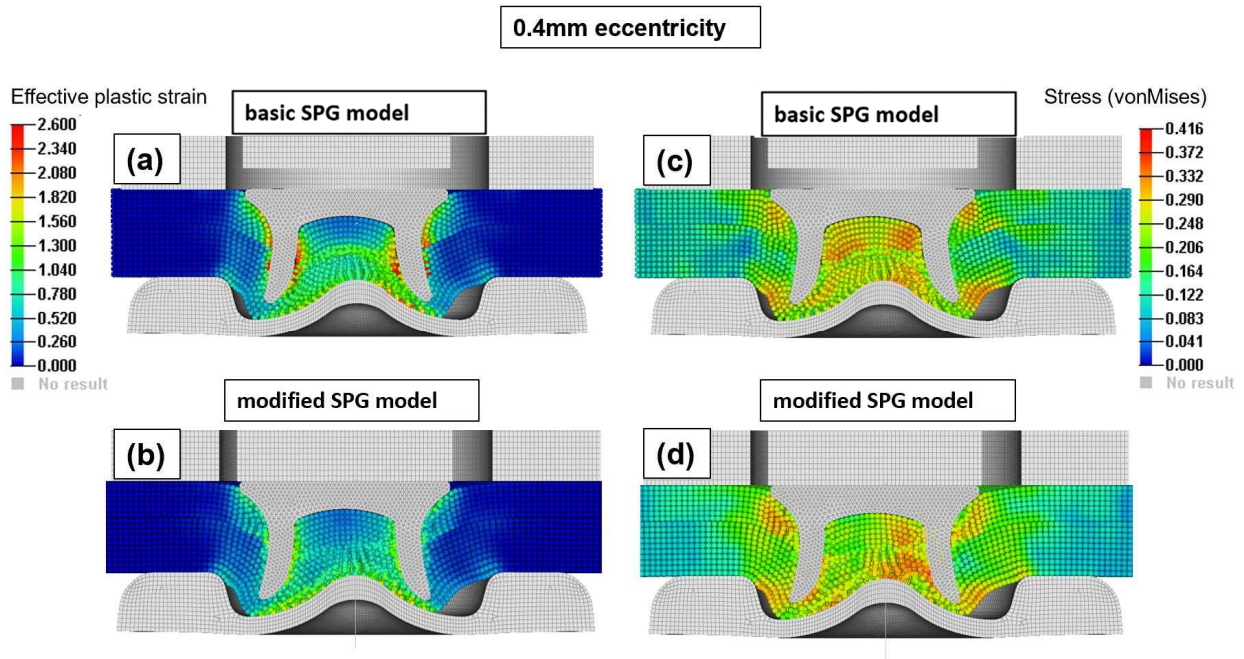

Figure 105 Comparison eccentricity of 0.4mm basic SPG model (a)(c) and modified SPG model (b)(d)

6.3.3.3 Force-displacement curve (eccentricity, modified SPG model)

The modified SPG eccentricity simulations shows a high correlation in respect to the shape of the curve. Illustrated in Figure 106, the influence of the eccentricity is very small. Only the maximum value at the end of the curve is scattered between 50kN and 43kN. The curves from the simulation (green, black, and red) are compared to the experiment (blue curve) with no offset.

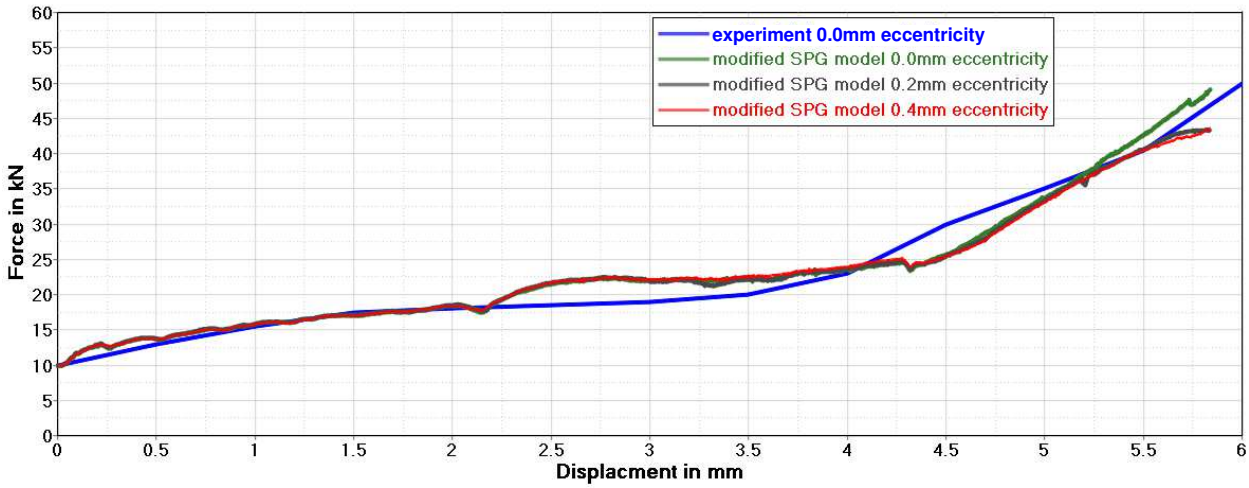

Figure 106 Force-displacement of modified SPG model with different eccentricity (0.0mm green, 0.2mm black, 0.4mm red)) compared to the experiment (blue)

6.3.4 Influence of die tilting (modified SPG model)

For the tilting simulation, the one-degree load case was analysed and compared to the basic SPG model from section 6.2.7. The applied hybrid SPG-FEM model was adapted with a second spring. The degree of freedom of the die was changed to allow it to rotate around the z-axis. The stiffness from the second spring (ID 31000001) was reduced to 20kN/mm. The translational and rotational movements were implemented with the option **BOUNDARY_PRESCRIBED_MOTION.* The model is illustrated in Figure 107.

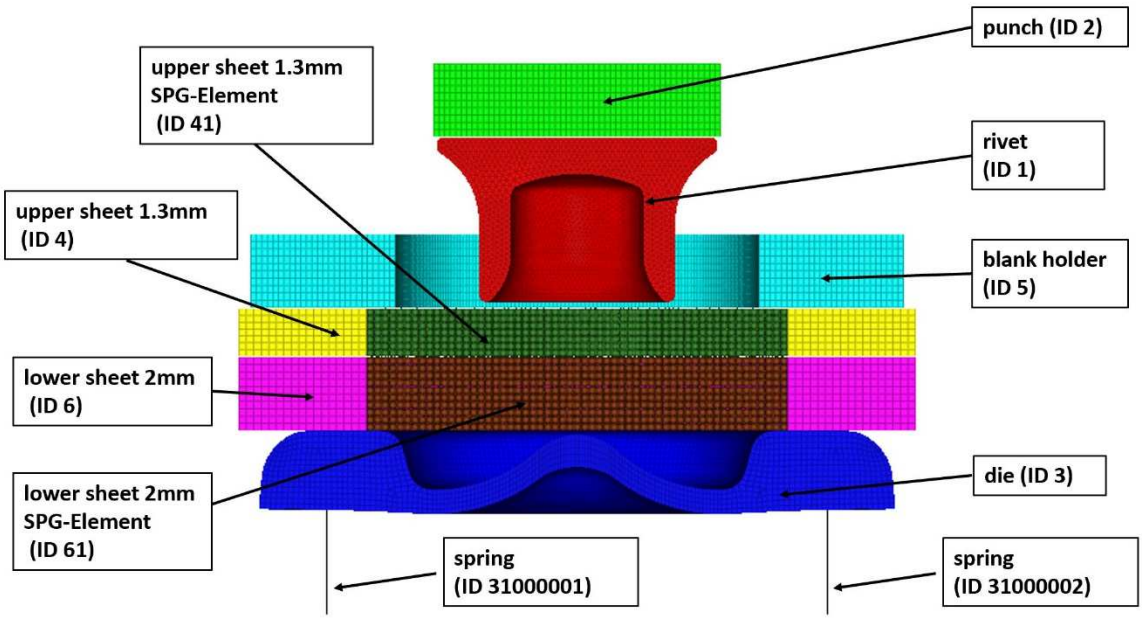

Figure 107 Tilting model for modified SPG simulation

6.3.4.1 Geometrical investigation (tilting, modified SPG model)

Figure 108 depicts the basic SPG model (a) and the modified SPG model (b). In the figure, the main geometrical features are marked with blue, green, and yellow circles. Overall, the deformations are very similar. Comparing the horizontal interlock, a minor, negligible difference (0.01mm) appears. The deformation in the yellow encircled area could be an optical mark for the tilting of the die during the setting process.

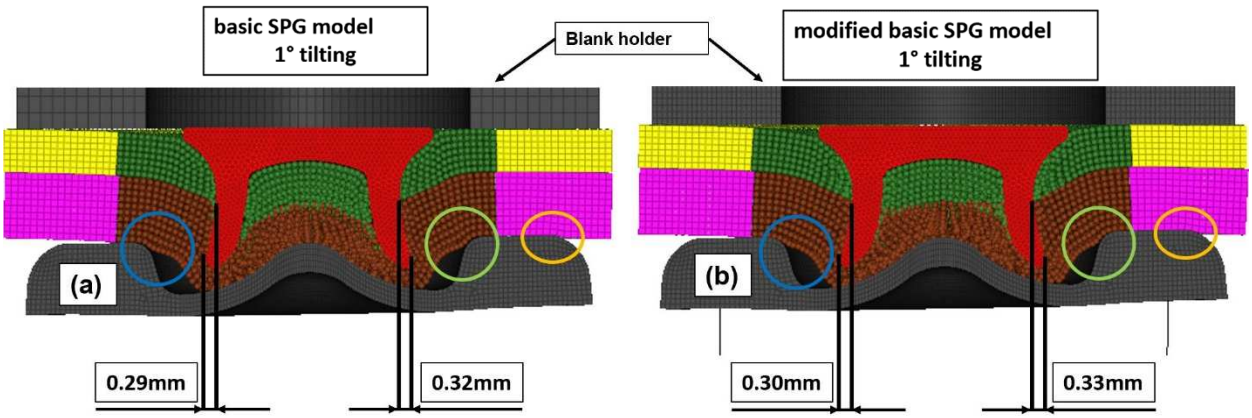

Figure 108 Deformation 1° tilting: (a) basic SPG model, (b) modified SPG model

6.3.4.2 Effective plastic strain and stress analysis (tilting, modified SPG model)

The effective plastic strain analysis in Figure 109 shows recognisable plastic deformation, encircled in red in the lower aluminium sheet. Compared to the basic model, the modified model shows the same value (~0.5) in the exact same area. Overall, the plastic strain of the modified SPG model tends to be lower than in the basic SPG model.

The von Mises stress analysis, illustrated in Figure 110, again shows a similar stress field of about 400MPa. One more significant difference is the high stress field in the lower aluminium sheet in the area of the bulge from the die. In the basic SPG model, a higher stress occurs compared to the modified SPG model (encircled in blue).

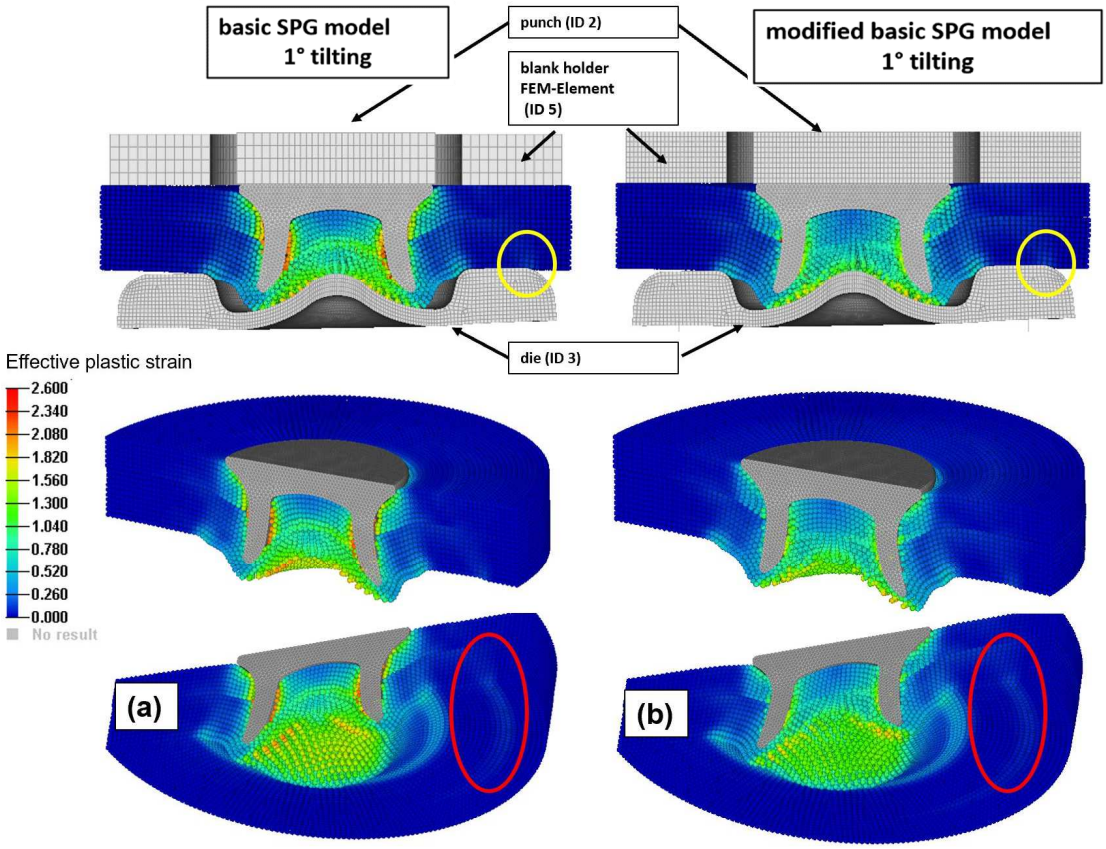

Figure 109 Comparison of effective plastic strain field of 1° die tilting: basic SPG model (a) and modified SPG model (b)

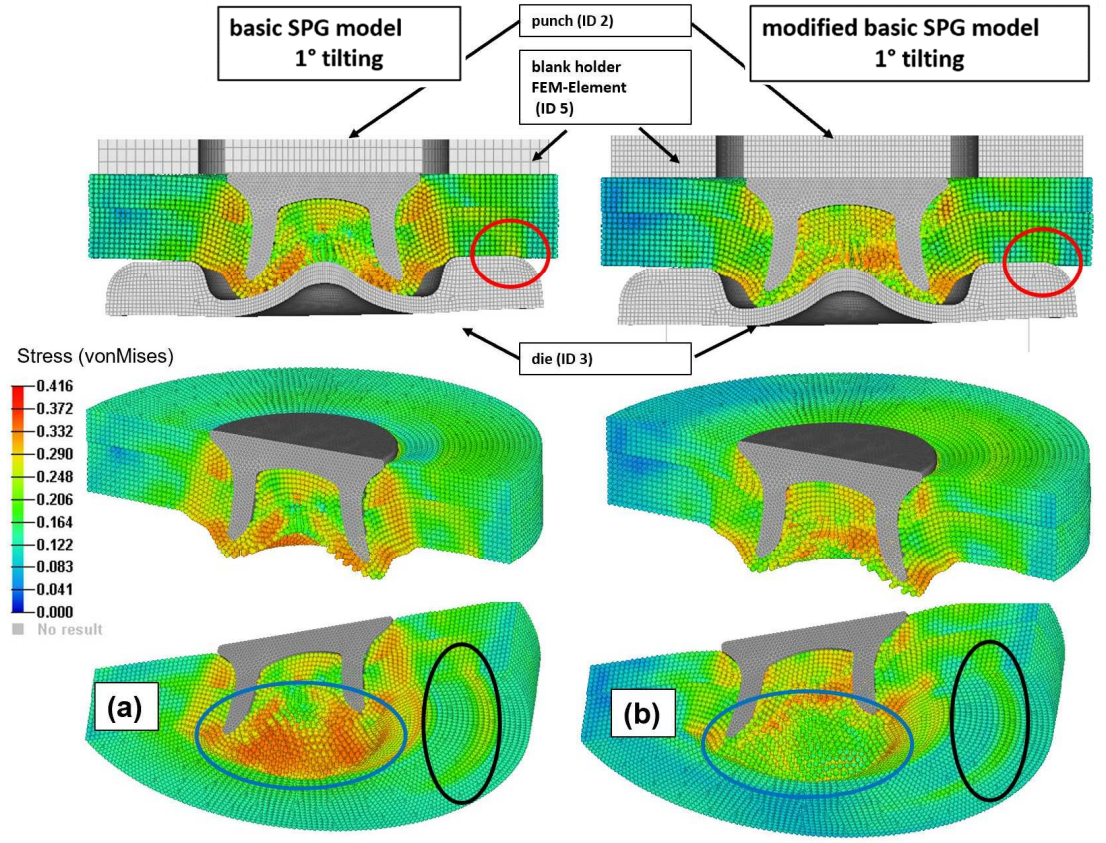

Figure 110 Comparison of stress of 1° die tilting: basic SPG model (a) and modified SPG model (b)

6.3.4.3 Force-displacement curve (tilting, modified SPG model)

The force-displacement curve in Figure 111 shows a very similar shape of the curves between the zero-degree tilting (modified SPG model) and the one-degree tilting. Only at the end do the curves spread. That means at one-degree die tilting, the maximum force decreases about 5kN.

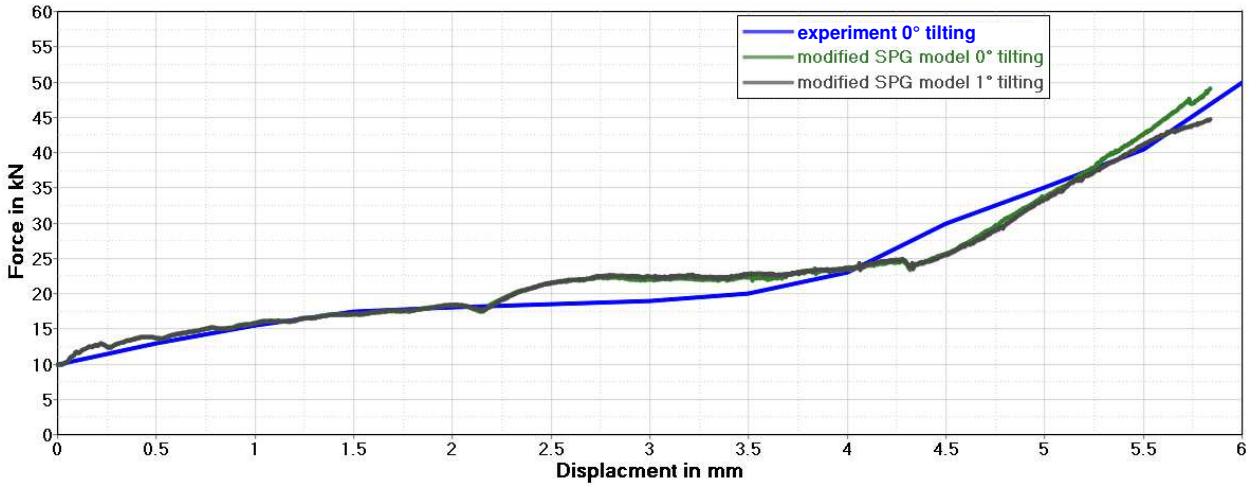

Figure 111 Force-displacement curve of the modified SPG 1° tilting simulation

6.4 Conclusion of 3D setting simulation

With the help of 3D setting simulation, the misalignment and die tilting could be analysed well. The EFG method is not recommended for such an investigation because of the stopping of the simulation and deleting of elements are time consuming and can bring some inaccuracies into the result. By using the SPG method, these problems can be avoided

Overall, the results of the basic SPG simulation look good and are comparable with the experiment. The material data are important in such a simulation because, if they are not accurate, the result has a high level of scattering compared to the experiment.

For exact results, the Eulerian kernel should be preferred to the updated Lagrangian kernel because of the better failure mechanism. However, a drawback of using the Eulerian kernel is the instability of the particles.

7 SUMMARY AND OUTLOOK

In this master's thesis, several numerical models of the setting process of an SPR were developed. Furthermore, the influence of the misalignment of the rivet and the tilting of the die were evaluated.

One approach taken for a self-piercing riveting process simulation is a 2D simulation, where the horizontal interlock, which is characteristic of the mechanical strength of an SPR joint, and the force-displacement curve, can be evaluated. As a starting point in this work, a 2D-setting simulation was developed and compared with the experimental data. The result showed high accordance with the experiment.

To evaluate the mechanical strength of the connection, an axial tension and a shear tension simulation were performed and again compared with experimental data. To create the FEM simulation, the result from the 2D setting simulation was rotated (180°) about the vertical axis, and the stress and effective plastic strain were mapped onto the 3D model.

During the rivet setting process, some issues like an offset between the rivet and the centre line of the tool or a tilting of the die can occur. The tool itself includes a C-frame, which has a certain stiffness because of its geometry. During the process, a force of 60kN or more can occur. This leads to elastic deformation of the frame and tool. The influence of a misalignment cannot be investigated with a 2D simulation model. Therefore, the main focus of the thesis was to create a 3D setting simulation model and evaluate the influences on the joint. The 3D setting process contained the rivet, upper aluminium sheet (thickness of 1.3mm), lower aluminium sheet (thickness of 2.0mm), die, blank holder, and punch.

Two different methods were used for the 3D simulation. First, a simulation with the EFG method was performed, and the advantages and disadvantages of the method were discussed. One major problem with this method was the stopping of the simulation shortly before piercing the upper aluminium sheet and the manual deletion of elements. After that step, the simulation continued with the calculation. This stopping and deleting process leads to high inaccuracy and is time consuming because more than one calculation is needed for a single joint.

The second approach was using the SPG method, which is a particle-based method, assumed to be more effective than the EFG method. A hybrid FEM-SPG 3D numerical model was developed for the simulation of the different misalignments such as rivet offset and tilting.

As the results illustrate, the model has a very high accordance with the experiment. The 3D model was validated by comparing the different simulation results with the experiment, e.g., microsection of the connections and the force-displacement curves of the setting process. Also, the effective strain field and the stress field (von Mises) were evaluated. Overall, with the present 3D model, different settings can be simulated, and the joining behaviour can be predicted accurately.

For future simulations with the 3D model, different settings like various sheet thicknesses, alternative materials such as aluminium and steel, or the connection of more than two sheets should be analysed. With the adaption of the 3D model to those settings, the prediction of the joint could improve, which would be helpful in checking the strength of the joint without any experiments. Moreover, the influence of a hybrid joint with adhesive between the sheets should be investigated because such joints are important in the automotive industry.

Finally, to check the mechanical strength of the joint and compare it with the experiment, the axial tension and shear tension simulation should be conducted with the 3D numerical model.

LIST OF FIGURES

LIST OF TABLES

ABBREVIATIONS

CAD	Computer-aided design
CAE	Computer-aided engineering
CFD	Computational fluid dynamics
CFRP	Carbon-fibre-reinforced plastic
SPG	Smooth Particle Galerkin
EFG	Element Free Galerkin
FEM	Finite Element Method
FEA	Finite Element Analysis
HAZ	Heat Affected Zone
NVH	Noise, Vibration, Harshness
MPP	Message Passing Parallel
tn	neck thickness
ts	undercut
etc.	etcetera

REFERENCES

[1] Chrysanthou, A., Sun, X. (eds.): Self-piercing riveting. Properties, processing and applications. Woodhead Publishing Series in Welding and Other Joining Technologies, vol. 82. WP Woodhead Publ, Oxford (2014), ISBN: 9781845695354

[2] Rowe, J.: Advanced materials in automotive engineering. Woodhead Publishing, Philadelphia (2012), ISBN: 9781845695613

[3] https://www.audi-mediacenter.com/de/fotos/detail/der-neue-audi-a8-l-43938, access: 16.02.2019

[4] Miklos T., Imre C.: Comparative study of the application of steels and aluminium in lightweight production of automotive parts. International Journal of Lightweight Materials and Manufacture **1**(4), 229–238 (2018). doi: 10.1016/j.ijlmm.2018.09.001

[5] https://www.audi-mediacenter.com/de/fotos/detail/der-neue-audi-a8-43909, access: 16.02.2019

[6] Hönsch F.: Experimentelle Untersuchung und statistische Analyse wesentlicher Prozessparameter beim Stanznieten von Aluminiumblechen, Masterarbeit; TU-Graz; (2017)

[7] Feldmann, K., Schöppner, V., Spur, G. (eds.): Handbuch Fügen, Handhaben, Montieren, 2nd edn. Edition Handbuch der Fertigungstechnik, / hrsg. von Günter Spur; 5. Hanser, München (2014); ISBN: 978-3-446-42827-0

[8] Enzinger, N.: Fügetechnik; Skriptum. TU Graz, Graz (2013)

[9] https://nptel.ac.in/courses/112107144/welding/lecture2.htm, access: 17.02.2019

[10] Wittel, H., Jannasch, D., Voßiek, J., Spura, C.: Roloff/Matek Maschinenelemente. Normung, Berechnung, Gestaltung, 23rd edn. Springer Vieweg, Wiesbaden (2017); ISBN: 978-3-658-17896-3

[11] https://www.fachwissen-technik.de/verfahren/schweissen.html, access: 18.02.2019;

[12] Messler, R.W.: Joining of materials and structures. From pragmatic process to enabling technology. Elsevier Butterworth-Heinemann, Amsterdam (2004); ISBN: 978-0-750-67757-8

[13] Dietrich, J.: Praxis der Umformtechnik. Umform- und Zerteilverfahren, Werkzeuge, Maschinen, 12th edn. Springer Vieweg, Wiesbaden (2018) ISBN: 978-3-658-19530-4

[14] Ostermann, F.: Anwendungstechnologie Aluminium, 2nd edn. VDI-Buch. Springer-Verlag Berlin Heidelberg, Berlin, Heidelberg (2007); ISBN 978-3-540-69451-9

[15] Eshtayeh, M.M., Hrairi, M., Mohiuddin, A.K.M.: Clinching process for joining dissimilar materials: state of the art. International Journal of Advanced Manufacturing Technology **82**(1-4), 179–195 (2016). doi: 10.1007/s00170-015-7363-0

[16] Neugebauer, R., Jesche, F., Israel, M.: Enlargement of the application range of solid punch riveting by two-piece dies. International Journal of Material Forming, **3**(S1), 999–1002 (2010). doi: 10.1007/s12289-010-0938-2

[17] Masoud S.: Processing and tooling considerations in joining by forming technologies; part A—mechanical joining; The International Journal of Advanced Manufacturing Technology, pp 1–55; (2018)

[18] Zhang, Y., Shan, H., Li, Y., Zhao, C.F., Luo, Z., Guo, J., Ma, C.Y.: Effects of the oxide film on the spot joining of aluminum alloy sheets: a comparative study between resistance spot welding and resistance spot clinching. International Journal of Advanced Manufacturing Technology, **92**(9-12), 4231–4240 (2017). doi: 10.1007/s00170-017-0387-x

[19] He, X., Pearson, I., Young, K.: Self-pierce riveting for sheet materials: State of the art. Journal of Materials Processing Technology 199(1-3), 27–36 (2008). doi: 10.1016/j.jmatprotec.2007.10.071

[20] https://media.boellhoff.com/files/pdf12/-rivset-at-de-6701.pdf
access: 22.02.2019

[21] Neugebauer, R., Mauermann, R., Grützner, R.: Hydrojoining. International Journal of Material Forming **1**(S1), 1303–1306 (2008). doi: 10.1007/s12289-008-0142-9

[22] Stahl-Informations-Zentrum, Leitfaden für erfolgreiche Verbindungen,

[23] Academic Program Altair University: Practical Aspects of Finite Element Simulation A Study Guide; (2015):

[24] Steinbuch, R.: Finite Elemente - Ein Einstieg. Springer-Lehrbuch. Springer, Berlin, Heidelberg (1998); ISBN: 978-3-642-58750-4

[25] Nielsen, C.V., Zhang, W., Alves, L.M., Bay, N., Martins, P.A.F.: Modeling of thermo-electro-mechanical manufacturing processes. Applications in metal forming and resistance welding. SpringerBriefs in applied sciences and technology manufacturing and surface engineering. Springer, London, Heidelberg, New York (2013); ISBN 978-1-4471-4643-8

[26] https://gns-mbh.com/products/indeed/
access: 24.02.2019

[27] https://www.computerhistory.org/makesoftware/exhibit/car-crash-simulation/
access: 24.02.2019

[28] King, R.P.: Setting load requirements and fastening strength in the self-pierce riveting process, In Proceedings of the 11th National Conference on Manufacturing Research: Leicester, UK. p. 57–61; (1995)

[29] Altair Eng., Inc., https://altairhyperworks.com/
access: 20.03.2019

[30] Geometrical Data from F. Hönsch; TU Graz; Working group Tools & Forming

[31] LS-DYNA® Keyword User's Manual Volume I, Version 10.0, Livermore Software Technology Corporation (LSTC), (2017)

[32] Spinella D.J.: Common Joining Methods Used in Aluminum Structures; Alcoa Technical Center; Presentation; (2013)

[33] LsDyna; https://www.dynasupport.com/tutorial/ls-dyna-users-guide/contact-modeling-in-ls-dyna; access: 27.02.2019

[34] Stelzmann, u.: Robuste und effiziente Kontaktmodellierung in Ls-Dyna: Wie gut sind die neuen Optionen?, 30. CADFEM Users Meeting 2012

[35] LsDyna: http://www.lstc.com/products/ls-dyna; access: 28.02.2019

[36] LS-DYNA® Keyword User's Manual Volume II Material Models, Version 10.0, Livermore Software Technology Corporation (LSTC), (2017)

[37] Domitner, J.: Numerical study on destructive testing of self-piercing rivet joints; X-Mech 2018, Tehran

[38] Hönsch, F. (2018): Numerical simulation and experimental validation of self-piercing riveting (SPR) of 6xxx aluminium alloys for automotive applications; IOP Conf. Series: Journal of Physics: Conf. Series 1063 (2018) 012081

[39] Hockett J E and Sherby O D, 1975, J. Mech. Phys. Solids 23, 87-98

[40] Hu W.: LS-DYNA ® Advanced FEM and Meshfree Methods for Solid and Structural Analyses – Manufacturing Applications; LS-DYNA Training Class, Notes¸(2016)

[41] Wu, C.T.: LS-DYNA Smooth Particle Galerkin (SPG) Method; LSTC SPG-Introduction

[42] Huang, L.: Simulation of Self-Piercing Rivet Insertion Using Smoothed Particle Galerkin Method; 15th International Ls-Dyna Users Conference; (2018)

[43] http://ftp.lstc.com/anonymous/outgoing/support/PRESENTATIONS/mpp_201305.pdf
access: 04.05.2019